Integrated experimental and computational analysis of mixed convection heat transfer from the human head, full body, and clothing microclimate

by

Zubeida Alali

B.S., Jordan University of Science and Technology, 2004
M.S., Kansas State University, 2019

AN ABSTRACT OF A DISSERTATION

Submitted in partial fulfillment of the requirements for the degree

DOCTOR OF PHILOSOPHY

Department of Mechanical and Nuclear Engineering
Carl R. Ice College of Engineering

KANSAS STATE UNIVERSITY
Manhattan, Kansas

2026

Abstract

Thermal comfort and heat exchange between the human body and its environment are critical factors in building design, apparel engineering, occupational safety, and the assessment of human performance in diverse climates. Accurately predicting the convective, radiative, and total heat transfer rates for the human body, and specific body segments such as the head, requires an integrated approach that combines controlled experimental measurements with high-accuracy computational fluid dynamics (CFD) modeling. The present study develops and validates a comprehensive computational fluid dynamics (CFD) framework designed to investigate mixed convection heat transfer from two critical human geometries: the human head and the full standing human body. These models represent both localized and whole-body thermal behavior, capturing the distinct effects of buoyancy-driven flows interacting with forced convection. The objective is to derive semi-empirical correlation for the average Nusselt number, providing predictive capability across a wide range of Reynolds, Grashof, and Richardson numbers. This correlation is developed with careful attention to it applicability for complex geometries, such as the head, where curvature, orientation, and local flow separation introduce additional complexities absent in simpler canonical cases like spheres or flat plates.

Building on this, the study further extends its scope to investigate heat transfer through the skin–clothing microclimate, using a fabric-covered cylinder model to represent clothed body segments. In this context, the fabric is treated as a porous medium, with permeability and porosity controlling the degree of airflow penetration and transport through the clothing layer. This addition captures a critical component of real-world heat exchange: the interaction between the skin surface, entrapped air gaps, and textile layers. By modeling the porous zone in detail, including parameters such as viscous and inertial resistance coefficients, porosity, absorption,

scattering, and radiation exchange, the study ensures that both transport through the fabric and radiative transfer within the pores are accounted for. This approach enables evaluation of clothing's thermal insulation in a physically realistic manner.

A high-resolution 3D CFD model of a nude thermal manikin head was created from 3D body scans, meshed with unstructured tetrahedral grids refined near the surface, and simulated in ANSYS Fluent (2020 R2) using the RNG k-ε turbulence model with enhanced wall treatment and discrete ordinates radiation modeling. Air properties were evaluated at the film temperature, and mesh independence testing ensured accuracy. Predicted convective heat transfer coefficients (h_c) were validated against five experimental cases (0.05–0.5 m/s air velocity; 5–30°C temperature difference), with deviations typically within ±2%. Total and radiative heat fluxes varied spatially, peaking at the nose and forehead due to flow acceleration and plume interaction.

The methodology was extended to a full standing body to compare whole-body and segmental heat transfer. Natural convection coefficients matched published mid-range values (≈3.76 W/m^2K), while forced convection coefficients scaled with air velocity in agreement with ASHRAE and Fanger correlations. Radiative coefficients (≈4.93 W/m^2K) matched established data. Velocity field analyses revealed buoyancy-driven plume tilting and recirculation patterns that shifted with Richardson number, supporting the mixed-convection modeling approach.

A 2D arm–clothing microclimate model quantified the effects of air gap, fabric conductivity, and emissivity. Results showed smaller gaps reduced natural convection but increased conduction, while higher conductivity and emissivity improved heat loss, demonstrating applicability to clothing design.

This integrated experimental–numerical approach links localized, whole-body, and clothing-related heat transfer, enabling accurate prediction across diverse conditions. Findings support applications in comfort assessment, thermal safety, and protective clothing design, with recommendations for future work including transient modeling, evaporative cooling, and complex garment simulations.

Integrated experimental and computational analysis of mixed convection heat transfer from the human head, full body, and clothing microclimate

by

Zubeida Alali

B.S., Jordan University of Science and Technology, 2004
M.S., Kansas State University, 2019

A DISSERTATION

Submitted in partial fulfillment of the requirements for the degree

DOCTOR OF PHILOSOPHY

Department of Mechanical and Nuclear Engineering
Carl R. Ice College of Engineering

KANSAS STATE UNIVERSITY
Manhattan, Kansas

2026

Approved by:

Major Professor
Steven Eckels

Copyright

Abstract

Thermal comfort and heat exchange between the human body and its environment are critical factors in building design, apparel engineering, occupational safety, and the assessment of human performance in diverse climates. Accurately predicting the convective, radiative, and total heat transfer rates for the human body, and specific body segments such as the head, requires an integrated approach that combines controlled experimental measurements with high-accuracy computational fluid dynamics (CFD) modeling. The present study develops and validates a comprehensive computational fluid dynamics (CFD) framework designed to investigate mixed convection heat transfer from two critical human geometries: the human head and the full standing human body. These models represent both localized and whole-body thermal behavior, capturing the distinct effects of buoyancy-driven flows interacting with forced convection. The objective is to derive semi-empirical correlation for the average Nusselt number, providing predictive capability across a wide range of Reynolds, Grashof, and Richardson numbers. This correlation is developed with careful attention to it applicability for complex geometries, such as the head, where curvature, orientation, and local flow separation introduce additional complexities absent in simpler canonical cases like spheres or flat plates.

Building on this, the study further extends its scope to investigate heat transfer through the skin–clothing microclimate, using a fabric-covered cylinder model to represent clothed body segments. In this context, the fabric is treated as a porous medium, with permeability and porosity controlling the degree of airflow penetration and transport through the clothing layer. This addition captures a critical component of real-world heat exchange: the interaction between the skin surface, entrapped air gaps, and textile layers. By modeling the porous zone in detail, including parameters such as viscous and inertial resistance coefficients, porosity, absorption,

scattering, and radiation exchange, the study ensures that both transport through the fabric and radiative transfer within the pores are accounted for. This approach enables evaluation of clothing's thermal insulation in a physically realistic manner.

A high-resolution 3D CFD model of a nude thermal manikin head was created from 3D body scans, meshed with unstructured tetrahedral grids refined near the surface, and simulated in ANSYS Fluent (2020 R2) using the RNG k-ε turbulence model with enhanced wall treatment and discrete ordinates radiation modeling. Air properties were evaluated at the film temperature, and mesh independence testing ensured accuracy. Predicted convective heat transfer coefficients (h_c) were validated against five experimental cases (0.05–0.5 m/s air velocity; 5–30°C temperature difference), with deviations typically within ±2%. Total and radiative heat fluxes varied spatially, peaking at the nose and forehead due to flow acceleration and plume interaction.

The methodology was extended to a full standing body to compare whole-body and segmental heat transfer. Natural convection coefficients matched published mid-range values (≈3.76 W/m^{2}K), while forced convection coefficients scaled with air velocity in agreement with ASHRAE and Fanger correlations. Radiative coefficients (≈4.93 W/m^{2}K) matched established data. Velocity field analyses revealed buoyancy-driven plume tilting and recirculation patterns that shifted with Richardson number, supporting the mixed-convection modeling approach.

A 2D arm–clothing microclimate model quantified the effects of air gap, fabric conductivity, and emissivity. Results showed smaller gaps reduced natural convection but increased conduction, while higher conductivity and emissivity improved heat loss, demonstrating applicability to clothing design.

This integrated experimental–numerical approach links localized, whole-body, and clothing-related heat transfer, enabling accurate prediction across diverse conditions. Findings support applications in comfort assessment, thermal safety, and protective clothing design, with recommendations for future work including transient modeling, evaporative cooling, and complex garment simulations.

Table of Contents

Nomenclature

A complete list of symbols, units, and abbreviations used throughout the thesis is provided. Also, the list of non-dimensional numbers utilized in this thesis is provided.

Symbol	Description	Units / Formula
Cp	Specific heat of air	kJ/(kg·K)
D	Characteristic diameter of the head	m
g	Gravitational acceleration	m/s^2
h	Local heat transfer coefficient	$W/(m^2·K)$
k	Thermal conductivity of air	W/(m·K)
q	Surface heat-transfer rate per unit area	W/m^2
Tw	Wall temperature	K
T∞	Free stream temperature	K
v	Local free stream velocity	m/s
k	Turbulent kinetic energy	J/kg
ε	Turbulent kinetic energy dissipation rate	J/(kg·s)
αa	Volume fraction of air	–
Gk	Turbulence kinetic energy from velocity gradients	–
Gb	Turbulence kinetic energy from buoyancy	–
ui	Mean velocity component in i-th direction	m/s
μt	Turbulent viscosity	kg/(m·s)
Sk, Sε	User-defined source terms	–
αk, αε	Inverse effective Prandtl numbers	–
r	Position vector	m
ν	Kinematic viscosity	m^2/s
s	Direction vector	–
s′	Scattering direction vector	–
S	Path length	m
a	Absorption coefficient	–
n	Refractive index	–
σs	Scattering coefficient	–
σ	Stefan–Boltzmann constant	5.669×10^{-8} $W/(m^2·K^4)$
I	Radiation intensity	W/sr
T	Local temperature	K
Φ	Phase function	–
Ω′	Solid angle	sr

Symbol	Name	Definition	Physical Meaning
Pr	Prandtl number	$Pr = \nu / \alpha$	Ratio of momentum diffusivity to thermal diffusivity; indicates relative thickness of velocity and thermal boundary layers.
Re	Reynolds number	$Re = \rho VD / \mu$	Ratio of inertial forces to viscous forces; characterizes flow regime.
Gr	Grashof number	$Gr = g\beta(T_s - T_\infty)D^3 / \nu^2$	Ratio of buoyancy forces to viscous forces; governs natural convection strength.
Nu	Nusselt number	$Nu = hD / k$	Ratio of convective to conductive heat transfer at the surface.
Ri	Richardson number	$Ri = Gr / Re^2$	Quantifies the relative importance of buoyancy-driven flow compared to forced convection.
y^+	Non-dimensional wall distance	$y^+ = u\tau\ y / \nu$	Near-wall mesh resolution parameter

List of Figures

List of Tables

Acknowledgements

I extend my deepest gratitude to my major professor and dissertation committee for their invaluable guidance, mentorship, and encouragement throughout the course of this research. I sincerely acknowledge the Institute for Environmental Research (IER) team members for their technical assistance, experimental support, and efforts that were essential to the completion of this work. I am especially grateful to Dr. Yingying Wu from the Department of Interior Design and Fashion Studies at Kansas State University for her expert guidance in 3D body scanning for apparel design, which significantly contributed to the development and accuracy of the geometric models used in this study. I also appreciate the technical support provided by Kansas State University's Graduate School and Information Technology Services. Finally, I am deeply thankful to my family for their unwavering support, patience, and encouragement throughout this academic journey.

Dedication

To my family, whose unwavering love and support have sustained me through every challenge, and to my late father whose memory continues to inspire my pursuit of knowledge and excellence.

Chapter 1. Introduction

1.1.Research objectives and motivation

This thesis is driven by the broader goal of improving our understanding of human thermal behavior in built and environmental systems. By combining experimental measurements with advanced computational modeling, the research aims to bridge the gap between theoretical heat transfer principles and their practical applications in human comfort, clothing design, and environmental control.

The primary objective of this thesis is to advance the scientific understanding of mixed convection heat transfer from the human head and full body through the integration of experimental measurements and computational fluid dynamics (CFD) simulations. Human thermal comfort and safety in built and outdoor environments depend heavily on accurate estimation of convective and radiative heat transfer from exposed body segments, as well as their interactions with clothing layers. Although many empirical correlations exist for simplified geometries such as flat plates, cylinders, or spheres, these models fail to account for the anatomical complexity of the human body, the variability of environmental conditions, and the mixed convection regime in which buoyancy and forced flow interact simultaneously. This research, therefore, aims to fill a critical gap by developing validated, geometry-specific correlations for human head heat transfer and by linking them directly to thermal comfort modeling.

The human head plays a disproportionately large role in the thermoregulation of the body compared to its surface area. Although the head and neck collectively account for approximately 10% of the body's total surface area, they are responsible for a significant fraction of total heat loss, particularly in cold or windy conditions. This is primarily due to the limited insulation provided by hair and the lack of substantial fat in the cranial region. Historical studies dating back to Newburgh (1950) and Froese (1960) highlighted the head's vulnerability to heat loss even when the remainder of the body was adequately clothed. Subsequent research, such as Rohles (1974), further established that environmental conditions including air velocity, turbulence intensity, and temperature gradients apply a strong influence on the perception of comfort when the head is exposed. Building on these foundational findings, the present thesis sets out a series of objectives focused on accurately estimating and modeling the thermal exchanges occurring at the human head, using both experimental and computational approaches.

The first objective was to generate a comprehensive dataset of heat transfer coefficients and surface flux distributions for the head under controlled environmental conditions. For this purpose, an advanced thermal head manikin, developed by Measurement Technology Northwest (MTNW), was employed. This device includes eight independently controlled thermal zones and a guard zone designed to minimize conduction losses at the base. Each zone can be regulated to maintain a target surface temperature in the range of 33–35 °C, consistent with average skin temperatures of the head, while the resulting heat flux required for this control is recorded. By placing the manikin within the large environmental chamber at the Institute for Environmental Research (IER), air velocity and temperature could be tightly regulated, enabling tests across a range of forced and mixed convection conditions. The resulting experimental data provide an essential foundation for evaluating the influence of environmental parameters such as air velocity (0.05–0.5 m/s), temperature gradients between the skin and air (5–30 °C), and turbulence intensity on head heat loss. These measurements serve a dual purpose: (1) validating numerical models and (2) filling critical gaps in the empirical literature regarding localized convective heat transfer coefficients for the head.

While experimental testing yields valuable insights, it is constrained by cost, duration, and environmental variability. Therefore, a parallel set of numerical objectives was established. The goal was to construct a high-accuracy three-dimensional computational fluid dynamics (CFD) model of the thermal head and surrounding chamber using ANSYS Fluent. A further objective was the implementation and evaluation of turbulence closure models, including the standard $k–\varepsilon$ model with enhanced wall treatment, to determine their suitability for low Reynolds number mixed convection flows. Radiation, which can account for up to 50% of total head heat loss, was modeled using the Discrete Ordinates (DO) method, ensuring that both convective and radiative components were adequately represented.

The numerical objectives extend beyond replication of experimental results. A key aim was to explore a much broader parameter space than is feasible experimentally, including Reynolds numbers ranging from 500 to 7,000, Grashof numbers up to 2.99 × 10^7, and Richardson numbers spanning both buoyancy-dominated and inertia-dominated regimes ($0.19 \leq Ri \leq 40$). This allowed for the systematic study of laminar-to-turbulent transition under mixed convection conditions, a phenomenon that remains poorly understood for head-shaped geometries. By linking surface heat flux distributions with localized flow structures such as plume tilting, recirculation zones, and separation points the simulations provide detailed insight into the mechanisms driving head heat loss.

The ultimate objective of the thermal head study is the derivation of semi-empirical correlations for predicting the average Nusselt number under mixed convection conditions.

Using Buckingham π-theorem, the convective heat transfer coefficient was expressed in terms of Reynolds, Grashof, and Prandtl numbers. Data obtained from CFD simulations and experiments were integrated through regression analysis using the Generalized Reduced Gradient (GRG) method to minimize squared residuals between predicted and observed values. The resulting correlation provides a practical yet accurate tool for predicting head heat transfer across a wide range of thermal and flow conditions. Notably, this is the first study to explicitly examine the effect of head diameter on heat transfer, enabling the extension of correlations to represent adult males, females, and children.

While the human head represents a critical site of heat exchange, the majority of thermal interaction between the human body and the surrounding environment occurs across the full body surface. The convective and radiative heat transfer coefficients of a standing human figure in still air is fundamental parameter for determining thermal comfort, designing energy-efficient built environments, and evaluating clothing systems. Yet, despite decades of study, reported values for whole-body convective heat transfer coefficients vary widely, reflecting differences in posture, air velocity, turbulence intensity, body geometry, and methodological approach. The experimental objectives for the full-body manikin consisted of two main components. First, to obtain accurate measurements of heat flux distributions and the average convective coefficients across the body in stagnant air. The second objective was to generate whole-body averages for convective and radiative heat transfer coefficients that could be directly compared with established standards such as those published in the ASHRAE Handbook of Fundamentals (2017). This serves both as a validation of the manikin-based methodology and as a benchmark for CFD results, ensuring that numerical predictions align with widely accepted reference values. The full-body manikin objectives contribute directly to advancing human thermal comfort modeling by addressing two major gaps in the literature: (1) the lack of consistent whole-body convective coefficients validated across experimental and numerical methods, and (2) the limited understanding of spatial variations in heat transfer across body regions. By combining experimental manikin data with validated CFD predictions, this research generates reliable, transferable correlations that can be applied in building energy simulations, HVAC system design, and personal protective clothing evaluation. Moreover, the findings highlight the importance of considering both convective and radiative components in human thermal modeling, as radiative exchange can account for nearly half of total body heat loss in certain environments.

The interaction between human skin, clothing layers, and the surrounding environment is central to understanding thermal comfort and protection in both every day and extreme conditions. Unlike the head and full-body models, which directly represent human geometry, the two-dimensional (2D) fabric-covered cylinder model provides a simplified yet powerful framework to investigate fundamental physics of heat and mass transfer in the clothing microclimate. The model approximates a clothed limb, where a heated inner cylinder (representing skin) is surrounded by a fabric layer modeled as a porous zone. This allows for the isolation and systematic study of permeability, porosity, and fabric thermophysical properties on overall insulation.

The primary motivation for this study is to address the limitations of existing models of clothing heat transfer. Many past studies have oversimplified fabric as an impermeable wall or as a thin barrier with fixed properties, thereby neglecting the transport of air through fabric pores.

The cylinder configuration serves as a benchmark system that creates a balance between being easy to compute and being relevant to thermal environments for clothed individuals.

The first objective is to construct a computational representation of fabric layers as porous materials using the porous zone approach in ANSYS Fluent. In this thesis, fabric resistance to airflow is captured using both viscous and inertial resistance coefficients, while heat transfer is represented through effective thermal conductivity, porosity, specific heat, and radiative properties (surface emissivity, absorption, scattering, and refractive index).

Key aspects include:

1. Porosity variation: Simulations will span a wide porosity range (5%, 27%, 50%, and 99%), representing fabrics from nearly solid-like materials (very dense weaves) to highly permeable mesh structures. High porosity is expected to correspond with better insulation performance due to increased air entrapment, while low porosity behaves closer to a solid barrier.

2. Permeability control: Fabric permeability will be varied across several orders of magnitude, from 10^{-9} m^2 (low-permeability dense cotton) to 10^{-11} m^2 (nearly impermeable structures). These values reflect realistic textile ranges and allow systematic examination of the balance between airflow penetration and insulation.

3. Thermophysical properties: Material constants for cotton (density, conductivity, specific heat) will be incorporated. Radiative effects will be considered through a two-flux approximation, accounting for absorption, scattering, and self-emission within the porous fabric.

By developing this porous media representation, the fabric is modeled not as a simple wall but as an active medium participating in coupled conduction, and radiation. A crucial research objective is to evaluate how the boundary treatment at the interface between porous fabric and surrounding free flow influences heat transfer predictions. The work of Somerton and Wood (1988) demonstrated that wall-type assumptions in porous media modeling significantly affect flow fields. Impermeable wall treatments can suppress lateral flows, increasing local velocities and pressure drops inside the porous medium. On the other hand, fully open boundaries allow mix sideway exchange, which can reduce velocity gradients and change predicted flow properties. In the context of fabric modeling, this means:

- Using an impermeable wall condition may underestimate transport, yielding results that exaggerate insulation and fail to capture realistic fabric performance.
- A semi-permeable or open boundary allows penetration of airflow through fabric pores, producing more realistic distributions of heat and mass transfer.

The objective here is to systematically compare simulation results under different boundary conditions impermeable, semi-permeable, and fully permeable and see their impact on convective heat transfer coefficients and total heat loss.

1.2 Literature review

A thermal comfort is defined as “that condition of mind that expresses satisfaction with the thermal environment” (ASHRAE Standard 55). This definition does not clarify what is meant by “condition of mind" or "satisfaction," but it accurately highlights that the assessment of comfort is a cognitive process that involves various inputs influenced by physical, physiological, psychological, and other factors.

Modeling the thermal comfort of humans becomes particularly complex in situations involving mixed convection, an interaction between natural convection, driven by buoyancy forces due to temperature differences, and forced convection, caused by external airflow such as wind or mechanical ventilation. In such scenarios, the behavior of heat transfer around the human body is influenced by multiple interacting factors, including body geometry, air velocity, ambient temperature, surface emissivity, clothing insulation, and even the posture and activity level of the individual. Mixed convection creates a highly variable and dynamic heat transfer environment, complicating the prediction and simulation of thermal comfort conditions. Accurately capturing these phenomena is essential for the design of energy-efficient buildings, comfortable indoor environments, and effective thermal protective clothing systems. Therefore, advanced computational tools, such as computational fluid dynamics (CFD), are increasingly used to model and analyze these complex interactions with greater precision.

Airflow, heat transfer, and mass transfer through clothing can be studied on different scales: (1) macroscale of the whole human body in protective clothing; (2) mesoscale of a single limb covered by clothing material; and (3) microscale, focusing on transport phenomena in the clothing material at the scale of individual fibers. Clothing material properties are important at all of these scales. Material models account for the heat transfer that involves conduction by the solid material of the fibers and intervening air, by radiation attributed to the large temperature difference and by convection when air penetrates the porous material.

In this thesis, it is acknowledged that the human head and neck represent a relatively small portion of total body surface area approximately 10%, yet they play a disproportionately large role in overall heat exchange between the body and its surroundings. This concept has been recognized for decades, beginning with early research in the 1950s by military physiologists who observed that significant heat loss occurred from the head, even when the rest of the body was well insulated. Newburgh (1950) emphasized the importance of protecting the head to prevent excessive heat loss and maintain thermal balance in cold environments. Froese (1960) later quantified non-evaporative heat loss using a gradient calorimeter, demonstrating a nearly linear relationship between external temperature and head heat dissipation across a wide range of ambient conditions. Rohles (1974) expanded on this foundational work by examining how air temperature and velocity affect both skin temperature and thermal sensation, showing that environmental conditions have a direct influence on human comfort perception.

Modern researches have transitioned from simple calorimetric studies to the use of thermal manikins that accurately replicate human geometry and heat production. These manikins enable precise measurement of convective and radiative heat transfer under controlled laboratory settings. Early modeling efforts, such as Fanger’s (1970) one-dimensional steady-state model, provided the theoretical basis for quantifying heat exchange from the human body. Tanabe (1994) later introduced transient finite element simulations capable of representing more complex and time-dependent heat transfer behaviors. Subsequent numerical studies, such as Kilic (2008), incorporated virtual thermal manikins into computational frameworks that accounted for multiple modes of heat transfer, convection, radiation, and airflow interaction, demonstrating that radiative heat exchange is a critical component of overall thermal balance.

Together, these developments highlight a continuous evolution in the study of human thermal behavior, from empirical measurements to advanced computational modeling. The application of thermal manikins integrates both experimental and numerical methodologies, providing enhanced understanding of localized heat transfer mechanisms, especially over curved and anatomically complex surfaces such as the head.

Liu et al. (2020) used a thermal manikin in a wind tunnel to evaluate forced convective heat loss from different body segments, demonstrating the significant influence of wind speed and turbulence on convective transfer. Similarly, Niu (2022) combined CFD simulations and wind tunnel experiments involving a thermal manikin situated within a lift-up building. This effort resulted in a regression equation predicting whole-body convective heat transfer coefficients based on wind speed and turbulence intensity. In the same year, Kurazumi et al. (2022) developed an empirical correlation for natural convection heat transfer in infants using a manikin, focusing on skin-to-air temperature differentials under strictly controlled environmental conditions.

A notable limitation in existing literature is the insufficient consideration of head diameter and the complexities of mixed mode heat transfer, where both buoyancy-driven and forced convection are significant. In this thesis, this gap is addressed through experimental investigations and the development of CFD models that simulate heat transfer from a thermal manikin head under mixed convection. The objectives include collecting empirical data on the effects of air velocity and thermal gradients, enhancing the database of convective heat transfer coefficients using CFD, and proposing simplified yet accurate correlations for predicting heat loss.

The thesis examines convective and radiative heat transfer coefficients under varying aerodynamic and thermal conditions, including different head sizes and air velocities. From these investigations, average Nusselt numbers are derived. Past literature has generated correlations for mixed convection over fundamental geometries such as spheres and cylinders. For instance, Yuge (1960) conducted detailed experiments on spherical surfaces under low Reynolds and Grashof number conditions, producing correlations based on combined natural and forced convection. Churchill (1977) developed a unified correlation equation for vertical plates that incorporated both free and forced convection, later extended to cylinders and spheres. Raju (1984) studied mixed convection across various Prandtl numbers, offering a broader framework for flat plate analysis.

In contrast to these simplified representations, this thesis employs a thermal manikin head modeled after an adult male with a 23-inch head circumference. Experiments were conducted within an environmental chamber across a temperature range of 5°C to 35°C. Complementary to these tests, a high-fidelity 3D CFD model was developed to simulate steady-state heat transfer, incorporating variable thermophysical properties. Simulations were performed across Reynolds numbers ranging from 500 to 6500, Grashof numbers between 4.45×10^6 and 2.99×10^7, and Richardson numbers from 0.19 to 40.8. The Prandtl number remained steady at approximately 0.72. A new correlation is proposed to predict Nusselt numbers for mixed convection around the human head, marking the first such correlation to include the effects of head diameter, extending even to female and child head sizes.

Understanding full-body heat transfer is essential for achieving thermal comfort in controlled environments. Convective and radiative heat transfer coefficients for a standing human body in still air are fundamental in developing accurate thermal comfort models and optimizing HVAC systems. These coefficients are pivotal in maintaining thermal equilibrium and energy efficiency.

This thesis also investigates heat transfer through clothing systems using simplified cylindrical representations of limbs, simulating real-world fabric-covered conditions. Porous textiles introduce complex thermal behaviors due to interactions between conduction and radiation, with air trapped in fabric pores acting as an insulative medium. The degree of insulation, however, depends on textile structure and properties.

Many early models emphasized conductive heat transfer and either ignored or oversimplified radiative transfer in porous materials. Pioneers such as Verschoor and Greebler (1965) and Rowley et al. (1970) explored radiative interactions in fibrous media, identifying mechanisms like absorption, emission, scattering, and transmission. Although some attempted to integrate radiation into effective thermal conductivity models, Torvi (1997) found its contribution to overall insulation to be minimal.

Common limitations in these models include the study of fabrics as air-impermeable layers with no or fixed thickness. Such assumptions neglect convective heat transport, a key mode of heat transfer under realistic conditions. Additionally, radiation is frequently excluded under the assumption of its insignificance at moderate temperatures. These simplifications limit the applicability and accuracy of the models.

The use of fabric-covered cylinders in controlled settings allows for precise evaluation of thermal behavior, particularly with varying air gaps and fabric layers. While full-body simulations provide greater realism, they are computationally demanding. Simplified models remain valuable for understanding key mechanisms of thermal exchange and for validating broader models.

Despite their long-standing importance, textiles have historically received limited attention within modern materials science. Gibson (1997, 2002) was among the earliest to introduce rigorous models for coupled heat and moisture transfer through porous fabrics, validating these models with experimental data and capturing the dynamic thermophysical interactions of textiles under varying environmental conditions. Gao and McCullough (2000) expanded this understanding by modeling a two-dimensional arm covered with a fabric layer, demonstrating that increasing fabric permeability resistance reduces convective heat loss. Sobera et al. (2002) subsequently conducted a study on porous-sheathed cylinders, which are comparable to clothed limbs in outdoor settings, and highlighted the significant impact of permeability and the thickness of the air gap on the overall heat exchange process. Havenith et al. (2006) advanced this research into three dimensions, simulating a clothed human torso to study heat and moisture transport between skin, fabric, and environment while addressing challenges related to complex geometry and mesh refinement. Building upon these findings, Pan (2007) highlighted the persistent gap in systematic scientific inquiry into the thermophysical behavior of clothing systems, underscoring the need for multidisciplinary approaches that integrate temperature, humidity, airflow, and fabric composition to accurately model human thermal comfort and protection.

Very recent studies have advanced our understanding of coupled heat and moisture transfer through clothing systems, thermal protective fabrics, and fabric-covered geometries under various environmental conditions. These works provide critical context for the present thesis's 2D fabric-covered cylinder model, which aims to quantify the combined conductive, convective, and radiative processes relevant to the human skin–clothing–air microclimate.

Su et al. (2022) conducted a numerical study of heat and moisture transfer in thermal protective clothing exposed to combined radiant and convective hazards. Their finite-volume CFD approach incorporated coupled heat and mass transfer equations, accounting for moisture evaporation, vapor diffusion, and conduction through multiple fabric layers. While their focus was on protective ensembles under high-intensity hazards, the underlying coupled transport methodology parallels the current study's treatment of thermal and diffusive resistances in fabric-covered geometries. However, in contrast to the complex multi-layer system in Su et al., our 2D model isolates a single fabric layer covering a heated cylinder to derive a clear correlation between airflow velocity, temperature gradients, and overall thermal resistance.

Similarly, Choudhary et al. (2020) developed and experimentally validated a 3D CFD model of the human torso wearing air ventilation clothing, simulating forced convection effects on cooling performance. Their work demonstrated the sensitivity of convective heat transfer coefficients to garment ventilation design, which aligns with the present research's observation that small changes in air gap geometry and flow regime can substantially alter local and average Nusselt numbers. While their human torso geometry is anatomically realistic, the simplified cylinder geometry used here enables systematic parameter variation and controlled isolation of fabric thermal resistance effects.

Experimental studies, such as Asawo et al. (2023), have taken a more direct measurement approach by using a heated cylinder in a wind tunnel to determine convection coefficients and thermal resistance for protective fabrics. Their results confirm trends in heat transfer coefficient increase with air velocity, matching the CFD-predicted behavior in our study. The experimental wind tunnel setup of Asawo et al. provides valuable empirical validation for our cylinder-based CFD approach, particularly regarding the velocity exponent in empirical correlations for forced convection.

In a broader thermal comfort context, Cernei et al. (2025) explored the impact of clothing insulation on thermal comfort evaluation using thermal manikins, emphasizing the role of clothing microclimate parameters in subjective comfort indices. Their findings support our inclusion of fabric thermal resistance in predictive correlations, as variations in insulation directly influence the surface heat flux patterns observed in our 2D cylinder simulations. Acharya et al. (2024) proposed a modified thermal protective performance model for fire-retardant clothing exposed to combined flame and radiant sources, focusing on transient heating and thermal damage thresholds. While their work emphasizes high-intensity, short-duration exposures, the physical principles of combined radiative and convective heat transfer are shared with the present study's steady-state framework. The distinction lies in the controlled, lower-intensity conditions of our experiments and simulations, which are more applicable to building comfort, occupational safety in mild climates, and sports apparel design.

Finally, Rogale et al. (2023) reviewed measurement methods for thermal resistance of clothing materials, highlighting the influence of test apparatus geometry and airflow conditions on measured results. Their conclusion, that fabric thermal resistance is not a fixed property but depends strongly on air velocity, air layer thickness, and posture—directly supports the relevance of our parametric CFD analysis. By quantifying how these parameters affect overall heat transfer from a fabric-covered cylinder, our work offers a simplified but physically grounded bridge between material-level thermal resistance data and full-body comfort modeling.

In summary, the literature reveals a progression from detailed full-body models to simplified geometric surrogates, with each approach offering specific advantages for isolating and understanding thermal transport mechanisms. The present 2D fabric-covered cylinder model builds on both experimental and CFD-based prior studies by combining controlled geometry with fabric covering effects, enabling derivation of semi-empirical correlations for Nusselt number as a function of Reynolds number, Prandtl number, and fabric properties. This targeted approach complements more complex models and provides a scalable foundation for integrating clothing microclimate effects into human thermal comfort prediction.

This thesis builds on these foundational studies, integrating CFD modeling with experimental validation to produce accurate and predictive models of heat transfer from clothed human bodies. Emphasis is placed on head heat loss and the interaction of clothing with environmental variables, providing new insights into mixed convection and material behavior in thermal comfort science.

1.3 The use of thermal manikins in evaluating human thermal environments

Thermal manikins have become crucial tools in thermal comfort and human thermoregulation research, with a history of continuous development spanning over six decades. Initially started as simple, passive models to assess heat loss, today's thermal manikins are advanced, human-shaped devices equipped with internal heating systems, segmented control zones, and highly sensitive sensors. These modern manikins are capable of reproducing human metabolic heat production and, in some cases, simulate sweating and active thermoregulatory responses. As highlighted by Fukazawa and Tochihara (2015), thermal manikins replicate realistic human geometry and posture, allowing researchers to accurately study the spatial distribution of heat transfer across different body regions under various environmental conditions. These features make them especially useful for assessing convective, conductive, and radiative heat transfer, as well as evaporative cooling from the skin or clothing surfaces.

The application of thermal manikins extends broadly across climate chamber testing, clothing system evaluation, HVAC performance studies. According to Psikuta et al. (2017) and McGuffin et al. (2002), manikins are routinely used in combination with environmental chambers to evaluate the thermal insulation of clothing ensembles under controlled wind, humidity, and temperature conditions. These resistance values are crucial inputs for biophysical and thermo-physiological models that simulate thermal comfort in various physical activities or exposed to extreme climates. These manikin-derived data are essential for international standards such as ISO 15831 and ASTM F1291, which govern the evaluation of clothing thermal insulation using heated manikins.

A significant evolution in manikin design has been the development of specialized segmental manikins or regional modules designed to study specific body parts (Wyon, 1989). These include heated manikin heads, hands, and lower limb segments to assess the thermal performance of headgear, gloves, footwear, or combinations. Full-body manikins are often divided into multiple independently controlled thermal zones commonly 20 to 30 segments or more each equipped with dedicated sensors and control feedback loops. Many manikins operate at a uniform surface temperature of approximately 34–35 °C to replicate human skin under thermo-neutral conditions. This approach provides a more physiologically accurate representation of heat transfer and clothing insulation effectiveness.

Despite their high accuracy, segmented manikins are not without limitations. One concern is internal conductive heat flow between neighboring segments, particularly in areas where thin insulation or tight-fitting garments cause thermal bridging. Additionally, lateral heat transfer through multi-layer clothing systems between body zones can skew localized heat loss measurements. To address these issues, two widely accepted methods have been developed for calculating overall clothing thermal insulation. The first is the parallel or global method, in which total heat losses and mean surface temperatures (weighted by area) are used to compute a single overall insulation value. The second is the serial or local method, which computes insulation individually for each segment based on its specific heat flux and temperature difference, and then sums the results. Each method has distinct advantages and limitations: the parallel method is less sensitive to localized measurement errors but may cover regional differences in insulation, while the serial method provides more small and distinct detail but can be affected by inter-segment heat flow and measurement noise.

Overall, the use of thermal manikins in this dissertation serves as a critical experimental tool for validating CFD-based simulations of human thermal environments. By comparing numerical predictions of heat transfer rates and clothing insulation to physical measurements obtained from manikin tests, this thesis ensures that the developed models accurately reflect real-world performance. The integration of both experimental and computational approaches strengthens the credibility of the findings and provides a solid foundation for future work in optimizing personal protective clothing, improving thermal comfort prediction models, and enhancing the design of human-centered environmental systems.

1.4 Future directions in clothing thermal research using CFD

Advancements in clothing research increasingly require predictive tools capable of quantifying thermal insulation and heat transfer under realistic environmental and physiological conditions. Traditional clothing evaluation methods such as guarded hot plates, static thermal manikins, and wind tunnel testing provide valuable benchmark data but remain limited in their ability to resolve localized heat transfer mechanisms, airflow patterns within the clothing microclimate, and the combined effects of convection, radiation, and fabric permeability. As demonstrated throughout this thesis, computational fluid dynamics (CFD), when validated against controlled environmental chamber experiments, offers a powerful framework for overcoming these limitations and advancing clothing thermal research beyond empirical testing alone.

Building on the experimental methodologies employed in this study, future clothing research can leverage CFD to predict thermal insulation and heat transfer performance for a wide range of fabric systems, garment fits, and environmental conditions prior to physical prototyping. By integrating porous media models to represent textile layers, coupled with radiation and mixed convection formulations, CFD enables explicit resolution of heat transfer pathways across the skin–air gap–fabric–environment system. This capability is particularly important for modern functional clothing, where insulation performance is strongly influenced by air gap thickness, fabric permeability, weave structure, and radiative transmissivity parameters that are difficult to isolate experimentally. The validated CFD framework developed in this thesis provides a direct pathway to extend such analyses from simplified geometries, such as fabric-covered cylinders, to anatomically realistic full-body configurations tested inside environmental chambers.

A critical strength of CFD-based clothing research lies in its compatibility with environmental chamber testing protocols. Chamber experiments provide well-controlled boundary conditions; air temperature, velocity, humidity, and radiation that can be directly replicated in numerical simulations. This consistency allows CFD models to be calibrated using measured heat fluxes and thermal resistances from manikin tests, ensuring physical realism while enabling parametric studies beyond the constraints of laboratory time and cost. Future research can take advantage of this model by systematically changing clothing characteristics and environmental factors in computational fluid dynamics (CFD)., while using targeted chamber experiments for validation. Such an approach supports the development of generalized correlations for clothing thermal insulation and convective heat transfer coefficients under mixed convection conditions, analogous to the Nusselt number correlations developed in this thesis for the human head and body.

Ultimately, the integration of CFD with environmental chamber-based clothing testing offers a transformative research pathway for predicting clothing thermal performance with higher spatial resolution, reduced experimental burden, and improved design insight. This approach is well suited for applications in occupational safety, military protective systems, sportswear, and thermal comfort-driven apparel design. By extending the validated modeling framework presented in this thesis to clothed human models, future studies can bridge the gap between textile material science and human thermal physiology, enabling predictive, physics-based evaluation of clothing systems under realistic thermal environments.

Chapter 2. Heat Transfer and Mixed Convection

2.1 Fundamentals of heat transfer and mixed convection

The interaction between the human body and its environment involves complex thermoregulatory processes that govern the exchange of heat and moisture. These exchanges are crucial for maintaining the body's thermal balance and ensuring physiological stability. The human body produces heat through metabolic activity, which includes both the metabolic rate required to support voluntary actions (M_{act}) and, in colder environments, the metabolic contribution of involuntary shivering (M_{shiv}) the total metabolic rate (M) is partially utilized to perform external mechanical work (W), while the remaining energy is released as heat. This residual heat is transferred to the surrounding environment via two primary pathways: the skin surface (q_{sk}) and the respiratory system (q_{res}). If the heat exchange with the environment does not fully balance the metabolic heat production, the excess or deficit results in heat storage (S) within the body, leading to fluctuations in core and skin temperatures (ASHRAE, 2017).

The overall heat balance of the human body can be expressed by the following energy balance equation:

$$M - W = q_{sk} + q_{res} + S = (C + R + E_{sk}) + (C_{res} + E_{res}) + (S_{sk} + S_{cr}) \tag{2.1}$$

Where,

M = rate of metabolic heat production, W/m^2

W = rate of mechanical work accomplished, W/m^2

q_{sk} = total rate of heat loss from skin, W/m^2

q_{res} = total rate of heat loss through respiration, W/m^2

C + R = sensible heat loss from skin, W/m^2

E_{sk} = total rate of evaporative heat loss from skin, W/m^2

C_{res} = rate of convective heat loss from respiration, W/m^2

E_{res} = rate of evaporative heat loss from respiration, W/m^2

S_{sk} = rate of heat storage in skin compartment, W/m^2

S_{cr} = rate of heat storage in core compartment, W/m^2.

Heat dissipation mechanisms include both sensible and latent heat exchanges. Sensible heat loss from the skin surface, quantified as the sum of convection and radiation, is affected by temperature gradients and air movement. Latent heat loss results from the evaporation of sweat or moisture diffused through the skin. In respiration, heat is lost both as sensible heat through the warming of inhaled air and as latent heat through the evaporation of water vapor during exhalation. These thermoregulatory losses are influenced by both personal and environmental parameters.

Key environmental variables include air temperature (T_{air}), mean radiant temperature (T_{rad}), air velocity (V_{air}), and water vapor pressure (P_a), all of which affect the rate and direction of heat exchange. On the other hand, personal variables such as activity level and clothing characteristics (e.g., thermal insulation and moisture permeability) significantly impact the body's thermal balance. Clothing modifies the heat exchange between the skin and the environment by introducing an additional barrier to heat and moisture transfer, influencing both convective and radiative losses.

In real-world scenarios, the body is often exposed to complex environments where both natural and forced convection occur simultaneously. This condition, known as mixed convection, arises when buoyancy forces due to temperature gradients interact with external airflow, such as wind or ventilation systems. Mixed convection represents a significant challenge for thermal modeling, as it introduces nonlinearities in flow and heat transfer behavior. The dominance of either natural or forced convection depends on the relative magnitudes of the Grashof and Reynolds numbers, often captured by the Richardson number (R_i) (see the non-dimensional numbers table in the nomenclature section).

Over the past several decades, extensive research has been devoted to understanding the interaction between human thermoregulation and environmental conditions. These studies have examined both steady-state and transient responses of the human body under various thermal exposures, leading to the development of biophysical models and heat balance equations that form the foundation of thermal comfort prediction and HVAC design (Fanger, 1970; Stolwijk, 1970; Churchill & Bernstein, 1977; Incropera et al., 1996; ASHRAE, 2005). Integrating these fundamental principles with computational tools such as computational fluid dynamics (CFD) has allowed researchers to simulate the heat transfer processes around the human body with increasing accuracy, thereby enhancing our understanding of mixed convection phenomena in realistic settings.

2.2 Human thermal comfort, clothing, and the microclimate

Textile materials have played a critical role in regulating human thermal comfort for thousands of years, yet they have rarely been examined with high precision and accuracy considering its physical and thermal properties without approximation of materials science. Human thermal comfort is a multidimensional physiological and psychological state achieved when the heat generated by metabolism is balanced by the heat lost to the surrounding environment (Gibson, 1997; Gibson, 2002; Pan, 2007; Islam et al., 2023). This balance is regulated by the body's thermoregulatory system, which maintains a relatively constant core temperature of approximately 37 °C. Environmental factors such as, air temperature, humidity, mean radiant temperature, and air velocity combined with personal factors such as activity level, posture, and clothing insulation to determine comfort conditions. In mixed convection scenarios, as addressed in this thesis's CFD and experimental models (see Sections 3.1–3.3), heat transfer from the body becomes a dynamic interaction between buoyancy-driven flow and mechanically induced air movement. These combined effects produce spatially non-uniform convective heat transfer coefficients across different body segments, influencing local and overall thermal sensation. Accurate quantification of these coefficients under realistic exposure conditions is therefore essential for predictive comfort modeling in HVAC design, building performance assessment, and thermal protection system development.

Clothing mediates heat exchange by forming a microclimate a thin, thermally active layer of air between the skin or inner clothing surface and the external environment. This microclimate's properties, including temperature, humidity, and air movement, are shaped by clothing insulation, material permeability, and fit. Under still-air conditions, the microclimate can act as an effective thermal buffer, reducing convective heat loss, whereas higher ambient velocities or body motion can disrupt the layer, increasing ventilation and promoting heat dissipation. These effects become particularly complex in mixed convection environments, where airflow patterns around the body (as later visualized in Section 5.4) interact with clothing geometry, influencing both local heat flux and moisture transfer. Such interactions have direct implications for perceived comfort and can alter the efficiency of evaporative cooling, especially in protective or performance-oriented apparel.

The integration of CFD simulations with experimental measurements, as implemented in this study, provides a comprehensive means to investigate the thermal comfort–microclimate relationship in detail. CFD modeling offers the spatial resolution necessary to predict local convective and radiative heat transfer coefficients for both nude and clothed conditions, while experimental data serve to validate and refine these predictions (see Section 4.3 for CFD validation). The results presented later in Sections 5.1–5.6 demonstrate how these methods were applied to quantify microclimate dynamics under varying Reynolds and Grashof number regimes, and how the derived correlations for Nusselt number (Section 5.3) provide generalized tools for predicting heat transfer in practical settings. These findings not only advance theoretical understanding but also inform the development of climate-responsive clothing, energy-efficient environmental controls, and thermal protection solutions designed to maintain human comfort and safety across a range of environmental exposures.

Chapter 3. Methodology

3.1 Experimental setup

The experimental work for this thesis was conducted inside a large walk-in environmental chamber at the Institute for Environmental Research, with internal dimensions of 3 m × 3 m × 4 m. This chamber provides a highly controlled environment where air temperature, relative humidity, and velocity can be regulated precisely using an autonomous air-handling unit. For the present study, the chamber was configured to replicate typical indoor and outdoor conditions relevant to mixed convection studies. The airflow within the chamber was introduced and maintained through inlet ducts located on the inner wall, allowing uniform air distribution and accurate control of boundary conditions. Air velocity was measured using calibrated low-velocity thermal anemometers at head level inside the chamber, averaged spatially under steady-state conditions, and used to define and validate CFD inlet conditions.

Two different experimental configurations were used: one involving a thermal head manikin and another employing a full standing nude thermal manikin (Stan). The thermal head setup consisted of a head form mounted at the center of the chamber at a height of approximately 1 m from the floor, while Stan, representing an average adult male, was suspended from a frame with 20 independently controlled thermal zones. In both cases, surface temperatures were maintained within the physiological skin temperature range of 33–35 °C. The heat flux required to sustain each zone at its setpoint was continuously measured, providing direct estimates of convective and radiative heat losses. A full description of the experimental facility including the chamber configuration, instrumentation, and measurement techniques is provided in the next section. Further details on how experimental data are used for model validation in the validation section in this thesis.

3.2 Experimental facility description

To realistically assess how environmental conditions influence heat exchange between the human body and its surroundings, life-sized heated manikins were used within the controlled environmental chambers of the Institute for Environmental Research (IER) at Kansas State University.

IER is a multidisciplinary research facility dedicated to exploring the thermal interaction between humans and their environments. As one of the few centers equipped with advanced environmental chambers and precision instrumentation, the Institute provides a setting for studying human thermal comfort. Its research spans thermal comfort and stress, clothing system performance, indoor environmental design, and other related areas.

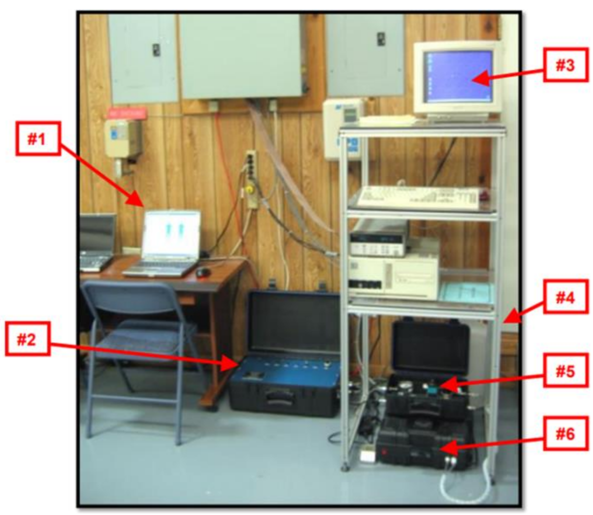

Figure 3.1 The environmental chamber control unit at the Institute for Environmental Research (IER)

This thesis presents an integrated system designed for the comprehensive evaluation of the thermal properties of clothing, utilizing two well-established measurement techniques: the guarded hot plate and the thermal manikin. These methods have been developed, calibrated, and routinely used at the Institute for Environmental Research (IER) to assess the thermal insulation and heat transfer behavior of textile materials under controlled environmental conditions see Figure 3.1.

The environmental chamber control unit at the Institute for Environmental Research (IER) at Kansas State University is a sophisticated setup designed to monitor and control experimental conditions for thermal comfort and heat transfer studies. The system comprises several interconnected components. The manikin laptop (#1) serves as the interface for operating and collecting data from the thermal manikin during experiments. The power supply enclosure (#2) provides regulated electrical power to the manikin and other instrumentation. The environmental chamber control computer (#3), positioned on the top shelf of the rack system, is responsible for regulating environmental parameters such as air temperature, humidity, and airflow within the chamber, ensuring precise and repeatable test conditions. The fluid supply reservoir (#4) stores the working fluid required for specific experiments, while the fluid supply enclosure (#5) houses the pumps, valves, and control electronics for circulating the fluid to the manikin. Finally, the UV light system (#6) is integrated for specialized tests involving radiation effects or sterilization requirements. Together, these components allow for a highly controlled testing environment, essential for accurate calibration, data collection, and validation of computational models.

3.2.1 Hot plate test

The guarded hot plate method is a steady-state technique used to quantify dry thermal resistance (Huang, 2006). The system consists of a measuring unit, temperature control module, and water supply unit, all housed within a specially designed environmental chamber to ensure stable and repeatable testing conditions (as illustrated in Figure 3.2). The measuring unit features a fixed metal block embedded with a square porous metal heating plate (3 mm in thickness), with a central test section measuring 0.254 × 0.254 meters. Surrounding the central section is a guard heater, which serves to eliminate lateral heat loss and ensure a one-dimensional heat flux through the specimen mounted at the center.

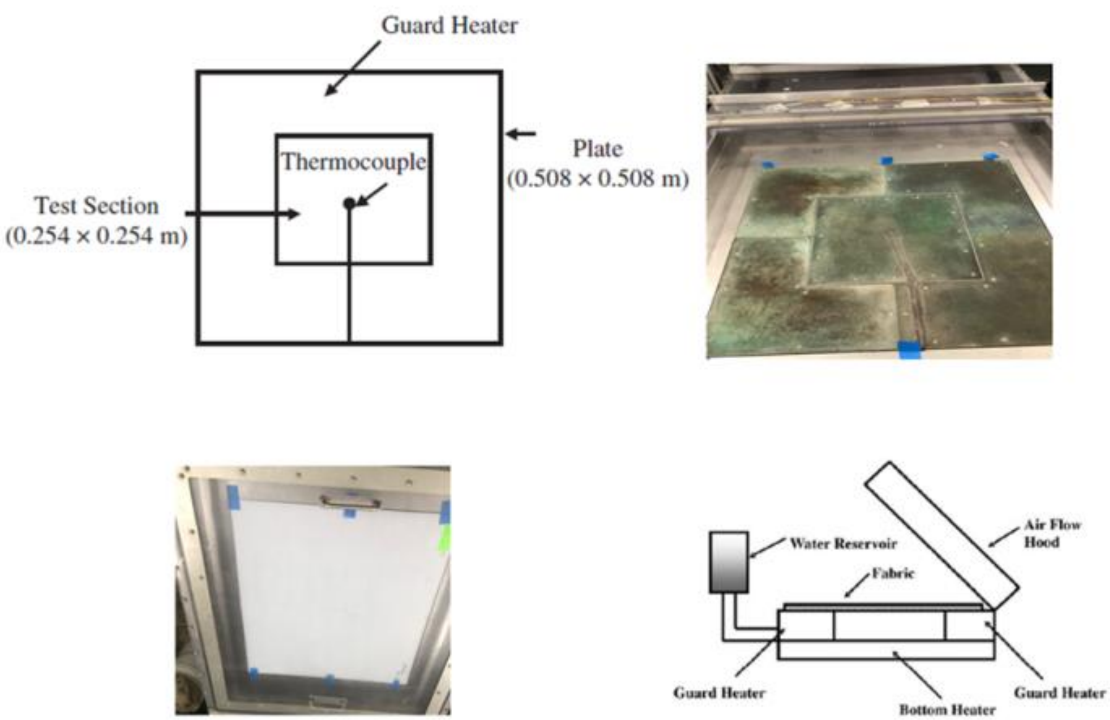

Figure 3.2 Schematic diagram of guarded hot plate.

During testing, a fabric sample is placed directly on the porous metal plate, which is heated to a constant surface temperature, typically around 35 °C to mimic human skin temperature. A temperature sensor embedded just beneath the plate surface records the actual plate temperature, while the power input needed to maintain this temperature is continuously monitored. This setup enables precise measurement of the heat transfer from the plate surface through the fabric and into the surrounding ambient air.

The dry thermal resistance of the fabric system is calculated based on the temperature gradient between the heated plate and the ambient air, and the amount of electrical power required to maintain this gradient. The equation governing this relationship is given as:

$$R_{tot} = \frac{A\,(T_{plate} - T_{air})}{H} \tag{3.1}$$

Where, $\mathrm{R_{tot}}$ is the total thermal resistance of the fabric and boundary air layer (m²·°C/W), A is the surface area of the heated test section (m²), $\mathrm{T_{plate}}$ is the surface temperature of the hot plate (°C), $\mathrm{T_{air}}$ is the ambient air temperature (°C), and H is the electrical power input (W). It is important to note that $\mathrm{R_{tot}}$ includes not only the resistance of the fabric but also that of the overlying boundary air layer. To isolate the intrinsic thermal resistance of the fabric ($\mathrm{R_{fabric}}$), a baseline measurement is conducted with the bare plate (i.e., without any fabric), yielding a reference resistance value $\mathrm{R_{bare}}$.The fabric-only resistance is then determined by subtracting this baseline value from the total:

$$\mathrm{R_{fabric}} = \mathrm{R_{tot}} - \mathrm{R_{bare}} \tag{3.2}$$

This methodology ensures that only the insulative properties of the fabric are captured, excluding the effects of the surrounding air layer. When combined with thermal manikin measurements, which simulate dynamic heat exchange between human skin and environment, this dual-method, system enables powerful characterization of clothing intended for thermal protection and comfort.

3.2.2 Thermal manikin testing

The thermal manikin "Stan" (developed by Measurement Technology Northwest (MTNW)) at the Institute for Environmental Research (IER) is designed to replicate the physical dimensions and thermal characteristics of an average adult male, with a total body surface area of approximately 1.80 m² and a height of 177.2 cm. Stan consists of a rigid shell segmented into 20 representative zones, each independently controlled

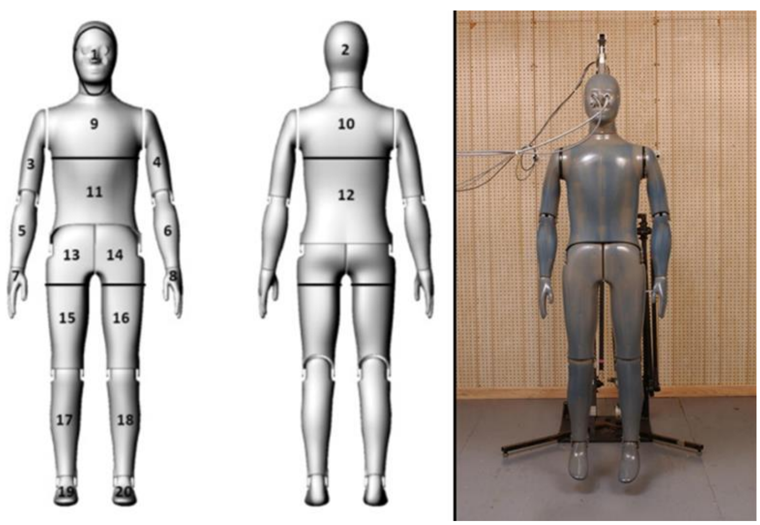

Figure 3.3 Thermal manikin Stan. Stan consists of a shell formed to simulate the physical shape and size of a typical man (i.e., 1.80 m^2 surface area, 177.2 cm height).

and instrumented to measure local heat transfer rates as shown in Figure 3.3. These zones correspond to specific body regions, including the face (Zone 1), head (Zone 2), upper arms (Zones 3 and 4), forearms (Zones 5 and 6), hands (Zones 7 and 8), chest (Zone 9), shoulders (Zone 10), stomach (Zone 11), back (Zone 12), upper thighs (Zones 13 and 14), lower thighs

(Zones 15 and 16), calves (Zones 17 and 18), and feet (Zones 19 and 20). Each zone has a defined surface area, ranging from 0.0442 m^2 for the hands to 0.1509 m^2 for the lower thighs, enabling detailed spatial resolution of thermal exchanges. The manikin's segmentation and precise surface area allocation allow for the assessment of local convective and radiative heat transfer coefficients, making Stan an essential tool for studying human thermal comfort, clothing insulation performance, and environmental heat transfer under controlled experimental conditions. The nude thermal manikin test procedure generally involved placing Stan, the 20-zone heated manikin, in the controlled environmental chamber under carefully regulated temperature, humidity, and airflow conditions. Each zone of the manikin was maintained at skin-like temperatures (35 °C), and the heat flux required to hold these setpoints was recorded, allowing direct measurement of whole-body and local heat transfer. These baseline nude tests provided essential reference data for validating CFD predictions of convective and radiative heat exchange.

Figure 3.4 Thermal manikin in climactic chamber.

To determine thermal resistance, a manikin is outfitted in the clothing system under investigation and placed within a controlled cool or cold chamber (as illustrated in Figure 5). Under steady-state conditions, the electrical power required maintaining a constant skin temperature is measured; this power input is directly proportional to the body's heat loss. Unlike methods such as the guarded hot plate that measure fabric insulation, manikin tests offer a more comprehensive evaluation by considering multiple real-world factors (Wyon, 1989):

- The proportion of the body surface area covered by textiles versus exposed skin,
- The non-uniform distribution of fabric and air layers over the body,
- The fit of the garments (whether loose or tight),
- The increased effective surface area for heat loss due to the clothing configuration.

- The influence of design features and adjustable elements (such as open fasteners or an upturned hood),

- Regional variations in temperature and heat flux, as well as changes resulting from different body positions (standing, sitting, lying down) and movements (such as walking). Consequently, manikin measurements provide a realistic quantification of how a textile system influences whole-body heat exchange with the environment. Although predictive models now exist to estimate the heat transfer properties of clothing based on fabric components and garment geometry, manikin-based assessments remain the more straightforward and practical approach.

3.3 Experimental methodology for the thermal head

The Thermal Head used in this thesis was developed by Measurement Technology Northwest (MTNW) to replicate the geometric and thermal characteristics of the human head with high precision. It consists of eight independently controlled thermal zones and one thermal guard zone See Figures 3.5-3.7. The guard zone functions to thermally isolate the other zones, thereby preventing unwanted conductive heat loss to the base structure a critical feature for ensuring that all measured heat losses are due mainly to convective, radiative, and evaporative mechanisms, rather than conduction through support structures. Each zone is regulated via distributed resistance wires that act both as heating elements and precision temperature sensors, allowing tight control over surface temperature.

The head base enclosure serves dual purposes: providing structural support and housing the electronic zone controllers, power connections, communication interfaces, and three ambient sensors as shown in Figure 3.5. These sensors monitor environmental temperature, velocity, and humidity in real time, ensuring that test conditions remain stable. In all experiments, the base enclosure was positioned on a table in the center of the environmental chamber, approximately 1 m above the floor, to minimize interference from ground boundary layers and to achieve uniform exposure to the chamber's controlled airflow.

The head was operated in temperature control mode, with each zone and the guard maintained at 35 °C, consistent with measured human skin temperatures for the head. The system continuously measured the heat flux (W/m^2) required to sustain the setpoint in each zone, providing high-resolution data on local and average heat losses. Airflow within the chamber was imposed through a controlled inlet wall, allowing tests over air temperatures from 5 °C to 25 °C (278.15 K to 298.15 K) and velocities from 0.05 m/s to 0.5 m/s.

This level of control and resolution is particularly important for the mixed convection heat transfer regimes investigated in this thesis, where both buoyancy-driven and forced airflow effects act simultaneously. By segmenting the head into multiple zones, it is possible to capture non-uniform heat transfer patterns caused by local variations in flow separation, turbulence, and temperature gradients effects that would be masked by a single-zone measurement. These detailed datasets formed the foundation for CFD model validation, ensuring that the simulated results accurately captured both global and local heat transfer characteristics.

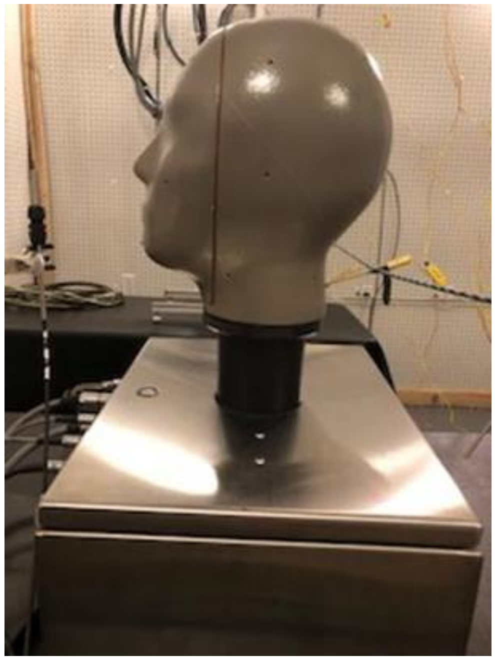

Figure 3.5 Thermal head.

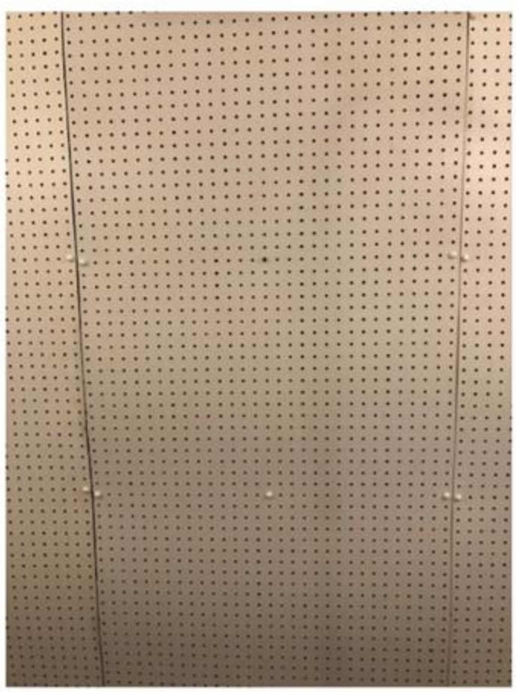

Figure 3.6 Inlet velocity wall.

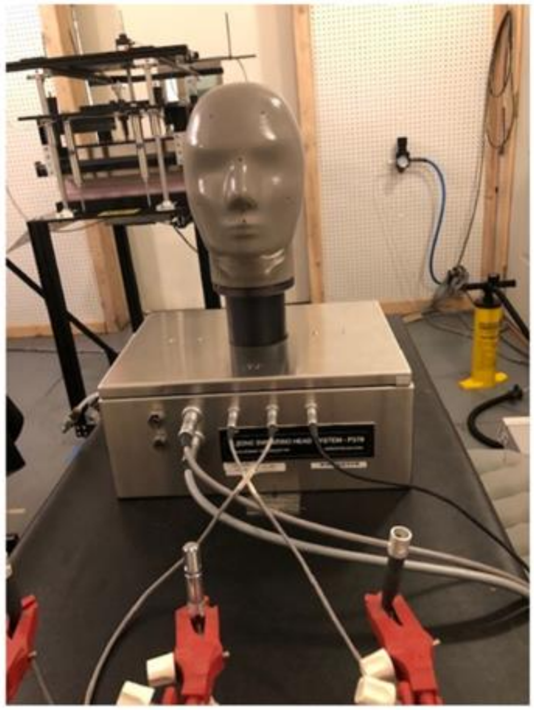

Figure 3.7 Head base enclosure.

3.4 Experimental methodology for the full-body nude thermal manikin

For the full-body nude thermal manikin, the experimental procedure closely followed the same methodology established for the thermal head, ensuring consistency across scales. Stan, the MTNW manikin representing an average adult male, was suspended at the chamber center and divided into twenty independently heated zones, each maintained at 35 °C see Figure 3.3. As with the head model, heat fluxes were measured under controlled conditions of air temperature (5–25 °C) and air velocity (0.2–0.4 m/s), providing zone-level data for convective and radiative heat transfer. While the head experiments offered detailed insight into localized heat transfer, the whole-body manikin allowed for the validation of CFD predictions on a more complex geometry, capturing segmental variations and enabling broader correlation development. This complementary approach ensured that both localized and whole-body effects were addressed within the same experimental framework.

3.5 Linking experimental design to CFD mesh refinement and boundary conditions

The experimental datasets obtained from both the thermal head and Stan were not only used for validation purposes but also played an essential role in defining CFD mesh resolution requirements and boundary condition selection. The detailed spatial distribution of heat flux from the multi-zone measurements directly informed local mesh refinement strategies in the CFD domain. For example, zones exhibiting sharp gradients in heat flux such as the forehead, crown, or shoulder areas were modeled with finer surface meshes and denser prism layer inflation near the wall to ensure accurate capture of boundary layer development and convective transition.

Additionally, the environmental chamber conditions in the experiments air temperature range (5 °C to 25 °C), controlled humidity, and air velocities from 0.05 m/s to 0.5 m/s (see Chapter 4, Table 4.2) were replicated as inlet boundary conditions in the CFD simulations. The measured turbulence intensity from the chamber's inlet air was incorporated into the CFD turbulence model parameters, ensuring that flow characteristics, such as separation points and recirculation zones, matched the physical setup.

The guard zone implementation in the thermal head provided a true adiabatic reference region, which was mirrored in the CFD model by applying zero heat flux boundaries at the base support structure. Similarly, the manikin's suspended position in the chamber was modeled with a symmetry clearance gap below the feet, preventing artificial conductive heat losses in the numerical domain.

By directly mapping the measured surface heat fluxes and ambient environmental conditions from the experiments into CFD boundary definitions, the simulations maintained a high degree of physical realism. This integration ensured that the CFD mesh topology, near-wall treatment, and turbulence model settings were grounded in empirical evidence, leading to more robust and credible correlation development for mixed convection heat transfer around the human head and body.

3.6 CFD methodology

The computational fluid dynamics (CFD) methodology developed in this thesis integrates experimental findings, detailed geometric modeling, and advanced numerical approaches to simulate mixed convection heat transfer from the human head, full-body manikins, and clothing microclimates. The numerical simulations were performed using ANSYS FLUENT adopting a steady-state approach to model coupled heat transfer and airflow interaction within a controlled chamber environment. The computational domain dimensions were selected to balance physical realism with computational efficiency (see Figure 4.1). Although this chamber size is smaller than the physical test environment, it maintains dynamic similarity while reducing mesh size and overall solution time.

In this thesis, the 3D geometry of the test subjects was carefully constructed using two complementary approaches to ensure accurate representation of complex human model while maintaining a surface suitable for meshing in CFD. The first approach involved generating a shrink-wrap surface around the original 3D geometry of the manikin. The raw geometry, particularly around the joints, often contained discontinuities, gaps, and irregularities that would interfere with mesh generation. To resolve these issues, the shrink-wrap function in ANSYS

SpaceClaim was applied, creating a continuous surface that enveloped the entire model. This shrink-wrapped geometry was then subjected to additional cleaning operations, including smoothing, hole filling, and surface merging, to eliminate discontinuities and ensure that the resulting model had a smooth surface. The final product was a clean and continuous surface suitable for computational meshing and subsequent CFD analysis. The second approach relied on 3D body scanning of the thermal manikin, which provided a high-resolution digital model capturing fine surface details using combination of 3D body scanner, Geomagic Studio, and Ansys SpaceClaim. The scans were post-processed to remove noise, patch missing data points, and reduce the total number of data elements to a manageable size for CFD simulations. By integrating surface repair techniques with scan reduction methods, the processed 3D body scans resulted in geometries that retained the essential measurements accuracy of the manikin while ensuring computational efficiency. Together, these two methods provided geometric foundations: the shrink-wrap process ensured continuity and mesh compatibility, while the 3D body scans preserved physical accuracy of human-like features. The combined use of both approaches enhanced the accuracy of the CFD models, especially for capturing localized heat and flow behavior around anatomically complex regions such as the head, joints, and torso.

Due to the highly complex geometry of the human form, unstructured tetrahedral elements were employed throughout the computational domain. Critical attention was given to the near-wall mesh resolution, particularly at the head, torso, and extremities, to resolve thermal boundary layers and accurately capture local heat flux. The enhanced wall treatment (EWT) in the RNG k–ε turbulence model requires a first cell center placement within the viscous sublayer ($y^+ \approx 1$), ensuring accurate prediction of near-wall velocity and temperature gradients.

Boundary conditions replicated the physical test chamber environment (Section 3.3, Experimental Setup). The inlet velocity was varied between 0.05 m/s and 1.0 m/s, with inlet air temperature ranging from 5°C to 25°C. Outlet boundaries were modeled with a gauge pressure of 0 Pa. The human head and manikin skin surface temperatures were held constant at experimentally determined values (e.g., 35°C for the head), with no-slip velocity conditions applied at all solid boundaries. Chamber walls were modeled as adiabatic surfaces to eliminate uncontrolled heat gain/loss.

The RNG k–ε turbulence model with enhanced wall treatment was selected for its proven ability to capture both free and forced convection flows around complex shaped bodies (Yakhot and Orszag (1986)). Radiative heat transfer was modeled using the Discrete Ordinates Model (DOM), which accounts for surface-to-surface radiation exchange. Given the high geometric resolution of the skin surface, view factor calculations required significant computational memory and processing time.

Spatial discretization employed a second-order upwind scheme for convective terms to enhance solution accuracy. The coupled pressure–velocity solver was used to ensure stable convergence in mixed convection regimes. Under-relaxation factors ranged between 0.1 and 0.5, tuned for each case to maintain stability. Convergence criteria were set to 10^{-6} for all residuals, ensuring the final solution satisfied strict mass, momentum, and energy conservation requirements.

Empirical correlations were developed for air thermophysical properties including density (ρ), thermal conductivity (k), kinematic viscosity (ν), specific heat (c_p), and volumetric expansion coefficient (β) using curve fitting to ensure temperature-dependent variation was captured across the studied range.

CFD predictions of convective heat transfer coefficients (h_{conv}), local heat flux, and radiative losses were validated against experimental measurements (see chapter 4, CFD validation section). These comparisons confirmed that the numerical setup could reproduce measured trends with deviations typically within ±2%. Importantly, the CFD results provided the spatially resolved heat flux data necessary to identify critical regions of high and low thermal exchange data that informed the mesh refinement strategy and boundary condition specification.

This validated CFD dataset also served as the foundation for the dimensionless Nusselt number correlations developed in Section 5.1 (Nusselt Number Correlation Development). By linking flow visualization, local heat flux mapping, and integrated heat transfer coefficients, the methodology ensured that each subsequent correlation was grounded in both physical measurement and high-accuracy numerical modeling.

The computational framework and experimental protocols established in this thesis were designed not only to capture the fundamental heat transfer mechanisms from the human body but also to quantify their implications for real-world thermal comfort scenarios. By resolving detailed flow fields, temperature distributions, and local convective coefficients, the approach enables direct assessment of how environmental parameters and body posture influence thermal exchange. However, the human body rarely exists in isolation from clothing, and the air layer trapped between the skin or clothing interior and the external environment the microclimate plays a critical role in regulating heat and mass transfer. Understanding this microclimate, and how it interacts with both buoyancy and forced flow, is essential for linking heat transfer predictions to practical comfort outcomes. Chapter six therefore examines the interplay between human thermal comfort, clothing systems, and the microclimate, providing the physiological and environmental context for the CFD and experimental results presented in later chapters.

3.7 Grid independence study

A grid independence test is a critical step in Computational Fluid Dynamics (CFD) to ensure that the numerical solution of a fluid flow problem is not influenced by the size or density of the computational mesh. In CFD, the physical domain is discretized into a finite number of cells or elements, and the governing equations are solved numerically over this grid. However, the accuracy of the results can be affected by the resolution of the mesh too coarse a mesh may lead to inaccurate predictions, while an overly fine mesh may unnecessarily increase computational cost without significant improvement in results.

To conduct a grid independence test, simulations are performed on multiple meshes of increasing density. Key output parameters such as pressure drop, velocity, temperature, or heat transfer rates are monitored across these simulations. The results are then compared to assess whether further refinement leads to significant changes. If the results converge to a consistent value as the mesh is refined, the solution is said to be grid independent. This allows the researcher to choose the coarsest grid that provides accurate results, optimizing the balance between computational efficiency and solution accuracy. Grid independence enhances the credibility of CFD studies by confirming that the observed results are governed by the physics of the problem rather than numerical artifacts introduced by the mesh.

Key parameters and convergence criteria are discussed for the head model, the manikin in the fully standing posture, and the 2D bare and fabric covered cylinder. A grid independence study was used to check for appropriate spacing throughout the domain. To perform this check, the total heat transfer from the computational head was calculated at higher grid resolutions and the corresponding differences were calculated. Figure 3.8 presents the results of the grid independence test performed for the head model. The number of mesh elements was progressively doubled until the variation in the computed total heat flux became less than 3%, indicating that further mesh refinement would not significantly affect the solution accuracy. The results show that as the mesh becomes finer, the predicted heat flux stabilizes and converges toward a consistent value. Based on this analysis, a mesh containing approximately 1,628,992 nodes and 5,693,173 elements was selected for subsequent simulations, simulation runtimes ranged from approximately 20 minutes to 12 hours to achieve steady-state convergence. This mesh density ensures that the numerical solution is independent of grid resolution while maintaining an optimal balance between computational cost and precision.

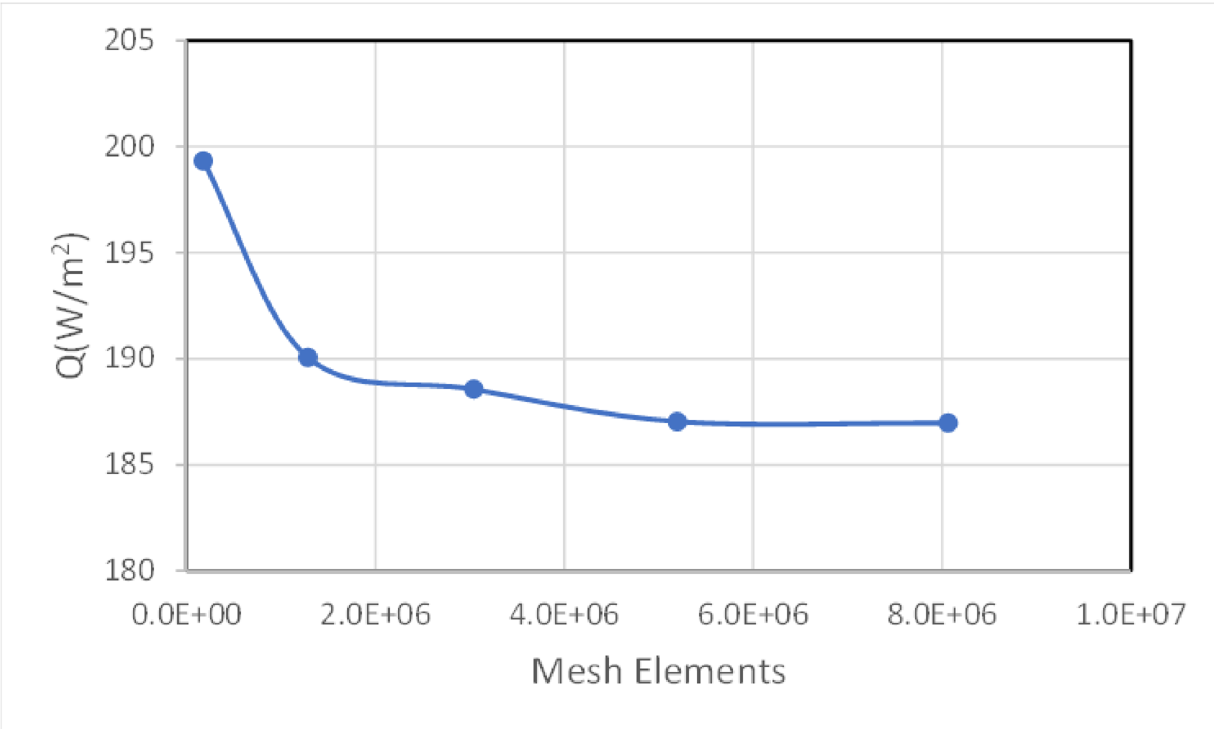

Figure 3.8 Grid independence test/head model

3.8 Effects of thermal radiation

Thermal radiation is a fundamental mode of heat transfer, particularly in applications involving human thermal comfort and thermal manikin testing. In many environmental and clothing-system studies, thermal radiation accounts for a substantial portion of the total heat flux, often up to 50%, especially in low-convection or indoor environments. This makes the accurate modeling of radiative heat transfer critical in computational fluid dynamics (CFD) simulations involving thermal manikins. Such simulations not only enhance our understanding of human-environment thermal interaction but also serve to evaluate and optimize clothing systems, HVAC systems, and indoor environmental design.

Human bodies, like all warm objects, emit infrared radiation. In controlled environments such as environmental chambers, where convective and conductive heat transfer are limited due to stagnant air or low airflow conditions, radiative heat loss becomes one of the dominant mechanisms. Thermal manikins, designed to mimic human thermoregulatory characteristics, are used extensively to evaluate clothing insulation, heat loss, and environmental comfort. Several studies have quantified the radiative component of the total heat flux from thermal manikins, showing that radiation can constitute 30% to 50% of total heat loss depending on surrounding surface temperatures and view factors (Tanabe et al., 1994; Zhang et al., 2010).

The net radiative heat exchange between a surface and its environment can be mathematically described using the Stefan-Boltzmann law:

$$q_{rad} = \varepsilon\sigma(T_s^4 - T_{sur}^4) \tag{3.3}$$

Where:

- q_{rad} is the radiative heat flux (W/m^2)
- ε is the surface emissivity
- σ is the Stefan-Boltzmann constant (5.67 x 10^{-8}W/m^{2}K^4)
- T_s is the absolute temperature of the surface (K)
- T_{sur} is the absolute temperature of the surrounding surfaces (K)

In the context of a thermal manikin in an enclosed space, view factors and enclosure geometry also play a role in determining the distribution and magnitude of radiative heat exchange. Therefore, computational modeling of such phenomena requires more advanced numerical techniques than simple empirical estimation.

To capture the complexity of radiative heat transfer in CFD, two radiation models are employed in this thesis, among the most commonly used are (ANSYS, Inc., 2020):

- The discrete ordinates (DO) radiation model is used in computational fluid dynamics (CFD) to simulate radiative heat transfer, particularly in situations where radiation penetrates a participating medium, like a solid material. It works by discretizing the angular space into a finite number of discrete directions, effectively turning the integral form of the radiative transfer equation (RTE) into a set of solvable equations. This allows for the simulation of radiation within and through porous material, considering factors like absorption, emission, and scattering.
- Surface-to-Surface (S2S) Radiation Model: This model is used when the medium between surfaces is non-participating (i.e., transparent to radiation). It is particularly useful for simulations in sealed chambers where radiation occurs between solid surfaces.

Each of these models can be tailored based on the scenario. For instance, the DOM model is especially useful in full-body manikin and thermal head simulations because it can account for radiation across various surface curvatures and configurations. The discrete ordinates model (DOM) in FLUENT was used to resolve the radiative transfer equation as part of the thermal radiation analysis. It's worth mentioning that the emissivity of the walls remains consistently effective across the relevant wavelengths within the temperature range studied, a wall emissivity of 0.95 was used in all simulations. For such cases, the gray DOM model can be used with little loss of accuracy. The number of bands was set to zero, indicating that only gray radiation will be modeled. The radiative transfer equation that is solved for the discrete ordinate method by discretizing both the xyz-domain and the angular variables that specify the direction of radiation is as follows (Cengel and Ghajar (2007)):

$$\frac{\partial I(\vec{r},\ \vec{s})}{\partial x_i} + \underbrace{(a\ + \sigma_s)\ (\vec{r},\ \vec{s})}_{Absorption} = \underbrace{an^2\ \frac{\sigma T^4}{\pi}}_{Emission}\ + \underbrace{\frac{\sigma_s}{4\pi} \int_0^{4\pi} I(\vec{r},\vec{s}')\Phi(\vec{s}.\vec{s}')d\Omega'}_{Scattering} \tag{3.3}$$

Tanabe et al. (1994) highlighted that thermal radiation plays a crucial role in comfort prediction, especially when convective cooling is minimal. Zhang et al. (2010) conducted comparative studies with and without radiation modeling in CFD simulations involving thermal manikins, and found that excluding radiation leads to a significant underestimation of heat loss and incorrect predictions of skin and clothing surface temperatures. Moreover, Fanger (1970) emphasized the relevance of radiative environments in the context of his PMV/PPD comfort model, establishing the need for realistic radiation modeling.

Modern simulation tools like ANSYS Fluent use these radiation models to analyze how conduction, convection, and radiation affect human bodies or models. These tools allow for both transient and steady analysis, helping to accurately assess clothing insulation, HVAC performance, and building thermal design. Thermal radiation plays an important role in heat exchange involving people or thermal models, making up to half of total heat loss. Accurately modeling this in computational fluid dynamics (CFD) simulations is crucial for reliable heat transfer predictions and understanding thermal interactions. Ongoing improvement and validation of these models against real data from thermal manikins are essential for progress in thermal comfort research and environmental engineering.

Chapter 4. CFD Modeling and Simulation

4.1 CFD modeling of the thermal manikin head

The CFD modeling work in this thesis was not developed in isolation; it was carefully constructed to complement, replicate, and extend the experimental measurements obtained from the multi-zone Measurement Technology Northwest (MTNW) thermal head.

4.1.1 Computational domain and mesh strategies

To accurately simulate the complex interactions of airflow and heat transfer between the thermal head manikin and its surrounding environment, ANSYS FLUENT (Version 19.1, Ansys Inc.) was employed to develop a high-accuracy steady-state computational model. This model replicated the key features of the experimental setup, providing an essential numerical framework for predicting convective and radiative heat transfer under controlled environmental conditions.

A three-dimensional representation of the environmental chamber was created, incorporating all essential boundaries and flow inlets/outlets. The computational domain was modeled with dimensions of 2.0 m × 2.0 m × 3.0 m, which is slightly smaller than the physical chamber used in the experiments see Figure 4.1. This scale reduction was carefully chosen to reduce computational cost and simulation time while still retaining the critical flow physics near the head. The decision was based on sensitivity checks indicating negligible influence of the chamber wall distance beyond these dimensions on the local convective heat transfer coefficients around the head. All simulations were executed on the dedicated CFD computing rack at Kansas State University to efficiently handle the resulting computational demand.

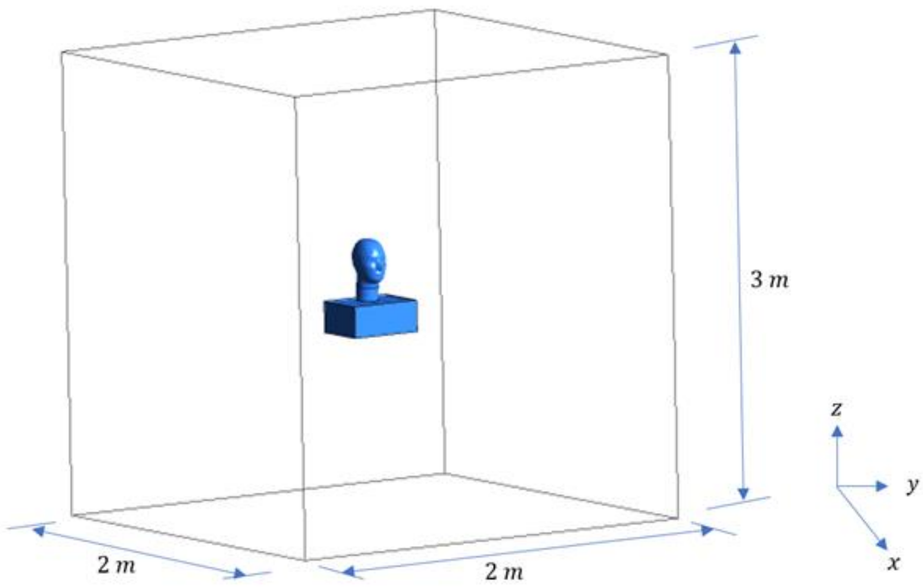

Figure 4.1 3D Model of the chamber and thermal head.

Given the complex curvature and complex geometry of the human head, an unstructured tetrahedral mesh was selected for the bulk of the computational domain as shown in Figure 4.2. This choice provided the flexibility to accurately resolve near surface contours, especially around the facial features, ears, and neck regions, where airflow separation and reattachment can occur. As early discussed in Chapter 3 during the grid independence study, the accuracy of the CFD solution is strongly dependent on the mesh density in regions of steep gradients. To address this, local mesh refinement was applied in the near-wall region surrounding the head surface, where high velocity and temperature gradients are most prominent. The final mesh contained 1,628,992 nodes and 5,693,173 elements, a level of resolution shown in Chapter 3 to provide less than 3% variation in total heat transfer compared with finer grids. This ensured that the chosen mesh represented an optimal balance between computational efficiency and solution accuracy, while maintaining consistency with the validated mesh independence results presented earlier.

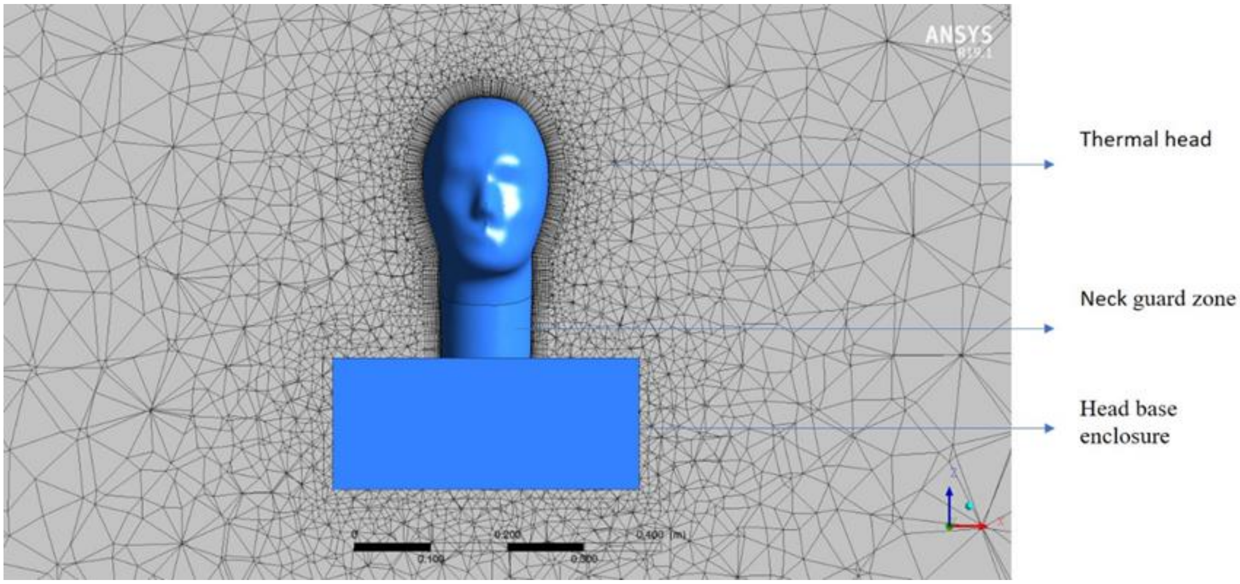

Figure 4.2 Mesh on a created XZ plane at Y = -0.01.

Near-wall resolution was given particular attention, as convective heat transfer prediction is highly sensitive to the mesh treatment within the boundary layer. In this model, the first grid point from the head surface was positioned to achieve a non-dimensional wall distance (y^+) of approximately 1.0, placing it well within the viscous sublayer. This resulted in a first cell height of approximately 0.6 mm. Such a resolution is essential for low Reynolds number turbulence modeling and for resolving the steep velocity and temperature gradients near the wall without over-reliance on empirical wall functions.

To better capture boundary layer development, ten inflation layers were employed around the head geometry. These layers extended through the estimated thermal and velocity boundary layers and were assigned a growth rate of 1.12 corresponding to roughly a 15% increase in cell height from one layer to the next. This gradual growth helped maintain mesh orthogonality and prevented sudden changes in cell aspect ratio, which could otherwise introduce numerical errors and compromise convergence stability.

Away from the head surface, where both temperature and velocity gradients are relatively small, a coarser mesh was applied to reduce computational expense without sacrificing accuracy. This mesh gradation ensured that computational resources were focused where they were most needed—within the near-wall regions and in the wake zone downstream of the head—while keeping the overall simulation runtime manageable.

The choice of near-wall treatment was also a critical aspect of the model setup. ANSYS FLUENT offers several wall modeling approaches, notably the Standard Wall Function (SWF) and the Enhanced Wall Treatment (EWT). Both methods were evaluated in this work to determine their suitability for replicating the experimental results. While SWF is computationally efficient and provides acceptable accuracy for high Reynolds number flows, it becomes less reliable for low Reynolds number or mixed convection scenarios where buoyancy effects are significant. EWT, by contrast, is designed to handle low y^+ meshes ($y^+ \approx 1$) and directly resolves the viscous sublayer, making it more appropriate for the low to moderate Reynolds number regime investigated in this thesis.

In summary, the mesh generation strategy for the 3D CFD model was directly influenced by the geometric complexity of the human head, the near-wall flow physics, and the need to align with the resolution of experimental data obtained from the multi-zone thermal manikin measurements. By refining the mesh near the head and carefully selecting boundary layer treatment methods, the model was optimized to predict local and overall convective heat transfer with high accuracy, thus enabling credible comparisons with experimental observations and supporting the development of reliable heat transfer correlations.

4.1.2 Simulation of mixed convection and flow visualization

Mixed convection heat transfer has been a subject of extensive study for decades, with numerous researchers approaching the problem from both experimental and numerical perspectives. These studies have yielded valuable correlations for certain ranges of Reynolds number (Re), Grashof number (Gr), and Prandtl number (Pr) (Churchill, 1977; Metais & Eckert, 1964; Raju et al., 1984; Ahmad & Qureshi, 1992; Maughan & Incropera, 1987). However, predicting mixed convection accurately remains a significant challenge.

From a computational standpoint, the difficulty lies in the fact that mixed convection involves the simultaneous presence of buoyancy-driven natural convection and externally imposed forced convection, each influencing the flow field and thermal gradients in different ways. Capturing these coupled effects with high accuracy requires fine spatial and temporal resolution in numerical simulations, which translates into large computational grids and long solution times making such analyses computationally expensive.

From an experimental perspective, resolving mixed convection effects is equally challenging. Laboratory experiments require precisely controlled environmental conditions, accurate measurement of temperature and velocity fields, and reliable methods for quantifying both convective and radiative heat transfer components. Such setups like the large environmental chamber used in this thesis, and running a sufficient number of test cases to map out the full parameter space (Re, Gr, Pr) can be extremely time-consuming.

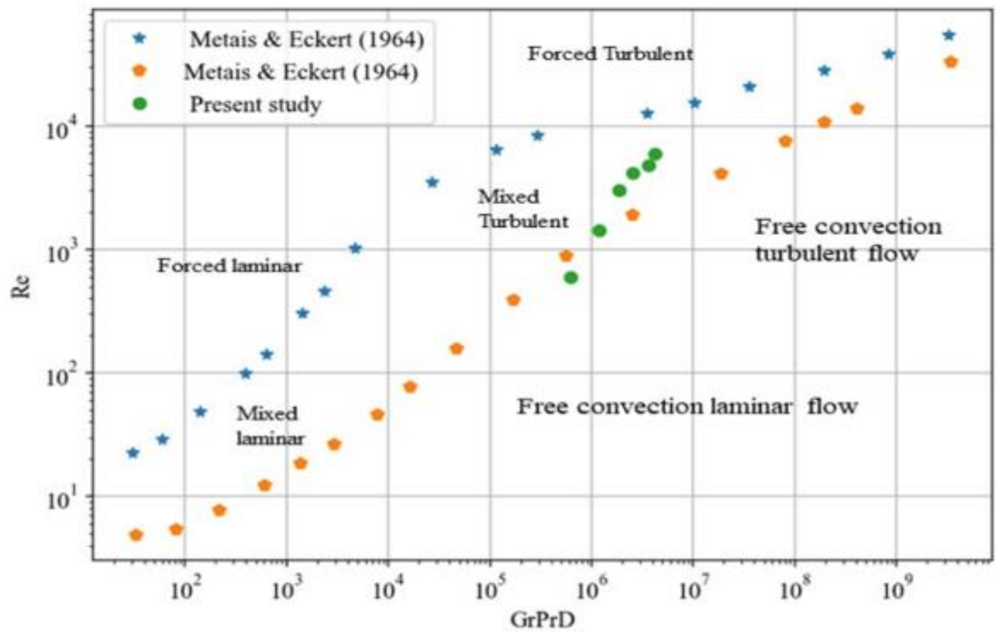

Figure 4.3 Metais & Eckert map (Metais, 1964), and experimental Re and (Gr Pr D) data.

The interaction between natural and forced convection can be classified into different regimes based on the relative strength of buoyancy and inertial forces. Metais and Eckert (1964) provided one of the most widely cited regime maps, plotting the Reynolds number (Re) on the vertical axis against the parameter Gr·Pr·(D) on the horizontal axis, where D is the characteristic diameter. The characteristic diameter of the head, D_{head}, was taken as 0.19 m, corresponding to the effective equivalent diameter of the thermal head manikin and used consistently in all non-dimensional analyses.

The map, reproduced in Figure 4.3, defines clear boundaries between pure natural convection, pure forced convection, and the mixed convection regime, with subdivisions for laminar and turbulent flows. The experimental conditions of the present thesis from the thermal head tests fall within the mixed convection region for both laminar and turbulent flow cases. This positioning reflects the environmental range tested: low-to-moderate Reynolds numbers combined with significant buoyancy effects due to temperature differences between the heated surface and the ambient air.

In the present study, the physical scenario involves airflow past a heated human head inside a climate-controlled chamber. Heat is transferred from the head to the surrounding air by two primary modes: convection and thermal radiation.

The temperature difference between the manikin head surface and the chamber walls induces a net radiative heat exchange, which can account for up to 50% of the total heat loss. Ignoring radiation in such a case would significantly underestimate the total heat transfer, leading to incorrect estimates of convective heat transfer coefficients. Therefore, radiative heat transfer is explicitly included in the CFD simulations, and the total heat flux from the head is defined as:

$$q''_{tot} = q''_{rad} + q''_{conv} \tag{4.1}$$

Here, q''_{rad} represents the radiative heat flux, and q''_{conv} is the convective heat flux. In ANSYS FLUENT, the radiative component is obtained using surface integrals, with radiation calculated via the Discrete Ordinates Model (DOM). The driving force for radiation is the temperature difference between the heated head surface and the cooler surrounding walls.

The convective heat transfer coefficient h_c is obtained by isolating the convective portion of the total heat flux:

$$h_c = \frac{q''_{conv}}{(T_{head} - T_{air})} \tag{4.2}$$

Where:

- The T_{head} is the mean head surface temperature (set by the thermal manikin control system),

- T_{air} is the ambient air temperature at the inlet boundary,
- q''_{conv} is the convective heat flux, determined from the CFD results after subtracting the radiative component.

Since:

$$q''_{conv} = q''_{tot} - q''_{rad,DOM} \tag{4.3}$$

The convective heat transfer coefficient can also be expressed as:

$$h_c = \frac{q''_{tot} - q''_{rad,DOM}}{(T_{head} - T_{air})} \tag{4.4}$$

The value of h_c depends not only on the head and air temperatures, but also on the air velocity, fluid properties, and the geometric features of the head. These factors combine to determine the local flow regime laminar, transitional, or turbulent around different parts of the head. Once h_c is known, the average Nusselt number (Nu) for the head is calculated to nondimensionalize the results and enable comparison with established correlations:

$$\mathrm{Nu} = \frac{h_c D_{head}}{k_f} \tag{4.5}$$

Where:

- D_{head} is the characteristic head diameter,
- k_f is the thermal conductivity of the fluid (air) evaluated at the film temperature, T_f = $(T_{head}$+ $T_{air})$/2.

The Nusselt number represents the ratio of convective to conductive heat transfer in the surrounding fluid. A total of 44 CFD simulations were conducted covering a range of ambiant air temperatures, air velocities, and head circumferences corresponding to adult male, adult female, and child dimensions these findings will be examined in greater detail in the subsequent chapters. From these simulations, the calculated Nusselt numbers spanned from 22.81 at the lowest air velocity 0.05 m/s to 57.25 at the highest air velocity (0.5 m/s), a more comprehensive discussion of these results is presented in the following sections of this thesis.

This variation demonstrates the strong dependence of convective heat transfer on airflow conditions, even in the presence of significant buoyancy effects. The combined experimental numerical dataset enables a robust analysis of mixed convection heat transfer for complex human geometries, offering new insight into how radiative contributions, flow regime, and head geometry interact to determine heat loss in realistic thermal environments.

4.1.3 CFD modeling – governing equations and numerical models

The fundamental equations for almost all CFD problems are based on conservation of mass, momentum, and energy. The CFD software performs these simulations using the finite volume method (FVM), which mainly involves discretization and integration of the governing equations over the entire finite volume. Equations 6, 7, and 8 represent the continuity, Navier-Stokes, and energy respectively in tensor form:

$$\frac{\partial \rho}{\partial t} + \frac{\partial(\rho u_i)}{\partial\left(x_{\{i\}}\right)} = 0 \tag{4.6}$$

$$\rho\left(\frac{\partial u_i}{\partial t} + u_j \frac{\partial u_i}{\partial x_j}\right) = \rho g_i - \frac{\partial \mathrm{p}}{\partial x_i} - \frac{2}{3}\frac{\partial}{\partial x_i}\left(\mu \frac{\partial u_j}{\partial x_j}\right) + \frac{\partial}{\partial x_j}\left[\mu\left(\frac{\partial u_i}{\partial x_j} + \frac{\partial u_j}{\partial x_i}\right)\right] \tag{4.7}$$

$$\rho\, c_p\left(\frac{\partial \mathrm{T}}{\partial t} + u_i \frac{\partial \mathrm{T}}{\partial x_i}\right) = -\rho\, \dot{q}_g + \frac{\partial}{\partial x_i}\left(k\, \frac{\partial \mathrm{T}}{\partial x_i}\right) + \beta\, T\left(\frac{\partial P}{\partial t} + u_i\, \frac{\partial P}{\partial x_i}\right) + \Phi \tag{4.8}$$

Where, $\dot{q}_g$ is rate of heat generation per unit volume, “k” is thermal conductivity, and Φ is the viscous dissipation rate.

FLUENT offers a wide variety of turbulent models and the choice of the turbulent model depends on the required level of accuracy. The Reynolds-Averaged Navier-Stokes (RANS) formulation is selected for all simulations in the present study. The results section of the thesis selects the best turbulence model for steady flow by comparing them with the experimental data. A brief review of the RANS momentum formulation and the turbulence models will help add insight to the final models selected and thus are included here.

The renormalization group (RNG) turbulence model was selected to enhance accuracy for flows at Reynolds numbers ranging from 500 to 7,000. The Reynolds-averaged form of the Navier–Stoke equation is shown in Equation 9 (Garbrecht, Kabelac, & Kneer, 2017):

$$\rho\left(\frac{\partial \bar{u}_i}{\partial t} + \bar{u}_j \frac{\partial \bar{u}_i}{\partial x_j}\right) = -\frac{\partial \bar{p}}{\partial x_i} + \frac{\partial}{\partial x_j}\left(\mu \frac{\partial \bar{u}_i}{\partial x_j}\right) + \frac{\partial\left(-\rho\, \overline{u_i' \, u_j'}\right)}{\partial x_j} + \rho g_i \tag{4.9}$$

Where, $\overline{u_i' \, u_j'}$ is the time-averaged value of the velocity fluctuating tensors and are generally identified as Reynolds stresses. Because the Navier-Stokes equations cannot provide sufficient information for a direct solution, modeling of the Reynolds-stress tensor is needed. In the present study, the gravity force acts in the "z" direction (i.e., $g_i = g_z$, while $g_x,\ and\ g_y = 0$ in Cartesian coordinates).

The pressure-based solver in FLUENT sequentially solves the momentum, continuity, and energy equations, in addition to turbulent quantities and radiation intensity one after another using the most recent updated values of air properties (e.g., density, viscosity, and specific heat), pressure, and velocity field. For a turbulent steady-state incompressible flow, the following items are important: 1) convection and radiation occur at manikin surface, 2) no other heat is generated inside the chamber 3) viscous heating, pressure work, and kinetic energy are neglected. The momentum Reynolds-averaged equation is expressed as follows:

$$\frac{\partial(\rho\,\overline{u_i u_j})}{\partial x_j} = -\frac{\partial P}{\partial x_i} + \frac{\partial}{\partial x_i}\left[\frac{\partial u_i}{\partial x_j} - \rho\overline{u_i'\,u_j'}\right] + \rho g_i \tag{4.10}$$

In the k-ε model, the Reynolds stresses are linearly related to the mean rate of strain by a scalar eddy viscosity as follows:

$$-\rho\,\overline{u_i'\,u_j'} = 2\mu_t S_{ij} - \frac{2}{3}\rho k \delta_{ij} \tag{4.11}$$

Where S_{ij} and μ_t are the mean rate of strain tensor and the eddy viscosity which are given as:

$$S_{ij} = \frac{1}{2}\left[\frac{\partial u_i}{\partial x_j} + \frac{\partial u_j}{\partial x_i}\right] \tag{4.12}$$

$$\mu_t = C_\mu \rho \frac{k^2}{\varepsilon} \tag{4.13}$$

and k and ϵ are the turbulent kinetic energy and dissipation rate, respectively, which are expressed as:

$$k = \frac{1}{2}\overline{u_l u_l} \tag{4.14}$$

$$\varepsilon = v\,\overline{\frac{\partial u_l}{\partial x_j}\frac{\partial u_l}{\partial x_j}} \tag{4.15}$$

Finally, the k-ε model consists of the following transport equations for k and ε using definitions in Equations 10-15.

$$\frac{\partial(\rho u_j k)}{\partial x_j} = \frac{\partial}{\partial x_j}\left[(\mu + \frac{\mu_t}{\sigma_k})\frac{\partial k}{\partial x_j}\right] + 2\mu_t S_{ij} S_{ij} - \rho\varepsilon \tag{4.16}$$

$$\frac{\partial(\rho u_j \varepsilon)}{\partial x_j} = \frac{\partial}{\partial x_j}\left[\left(\mu + \frac{\mu_t}{\sigma_\varepsilon}\right)\frac{\partial \varepsilon}{\partial x_j}\right] + 2C_{1\varepsilon}\frac{\varepsilon}{k}\mu_t S_{ij} S_{ij} - C_{2\varepsilon}\rho\frac{\varepsilon^2}{k} \tag{4.17}$$

The RNG k-ε model is derived by using a mathematical technique called the RNG method to derive velocity correlations generated by the Navier-Stokes equation with a random force term. Parallel to Equations 16 and 17 for standard k-ε model, the following equations of turbulent kinetic energy, k, and its dissipation rate, ε, are used with the RNG k-εmodel:

$$\frac{\partial(\rho k)}{\partial t} + \frac{\partial}{\partial x_i}(\rho u_i k) = \frac{\partial}{\partial x_j}\left[\alpha_k \mu_{eff} \frac{\partial k}{\partial x_j}\right] + G_k + G_b - \rho\varepsilon - Y_M + S_k \tag{4.18}$$

$$\frac{\partial(\rho\varepsilon)}{\partial t} + \frac{\partial}{\partial x_i}(\rho u_i \varepsilon) = \frac{\partial}{\partial x_j}\left[\alpha_\varepsilon \mu_{eff} \frac{\partial \varepsilon}{\partial x_j}\right] + C_{1\varepsilon} \frac{\varepsilon}{k}(G_k + C_{3\varepsilon} G_b) - C_{2\varepsilon}\rho\frac{\varepsilon^2}{k} - R_\varepsilon + S_\varepsilon \tag{4.19}$$

Here $\alpha_k, \alpha_\varepsilon$ are the inverse effective Prandtl numbers, $R_\varepsilon = C_\mu \rho \eta^3 \frac{(\frac{1-\eta}{\eta_0})\varepsilon^2}{(k(1+\beta\eta^3)}$, $\eta = \frac{sk}{\varepsilon}$, $C_{1\varepsilon}$ = 1.42, $C_{2\varepsilon}$= = 1.68, η_0= 4.38, and β = 0.012 are model constants. The empirical constants were assumed reasonable for the current study (ANSYS, Inc., 2024).

The k-ε model requires EWT to capture correct viscous sublayer behavior. The RNG k-ε model has significant changes in the ε equation, which improves the ability to model flows with large streamline curvature and has additional options aid in predicting low Reynolds number flows.

The boundary conditions included specified uniform field temperature and velocity profile, no-slip condition, and specified temperature at the head surface. The convective terms were discretized using second-order upwind scheme. The coupled algorithm was used to handle the pressure-velocity coupling. Typical values of under-relaxation factors were set from 0.1 to 0.5. A convergence criterion of 10^{-6} for each scaled residual component was specified for the relative error between two successive iterations. Tables 4.1 and 2 summarize the details of the numerical method and boundary conditions.

Table 4.1 Details of simulation models and numerical schemes.

Category	Model / Method
Viscous Model	• RNG k–ε model • Enhanced wall treatment • Full buoyancy effects • Curvature correction
Radiation Model	• Discrete Ordinates (DO) model
Fluid	• Air
Solid (Head Base/Box)	• Stainless Steel 316
Solution Method	Pressure–Velocity Coupling Scheme: • Coupled method Spatial Discretization: • Pressure: Body force weighted • Momentum: Second-order upwind • Turbulent Kinetic Energy: Second-order upwind • Turbulent Dissipation Rate: Second-order upwind • Energy: Second-order upwind • DO Radiation: Second-order upwind

Table 4.2 Boundary conditions for simulation setups.

Boundary Name	Type	Specified Variables / Range
Chamber air inflow	Inlet velocity	Air velocity: 0.05–0.5 m/s
Inlet temperature	Temperature	Air temperature: 5–25 °C (278.15–298.15 K)
Chamber air outflow	Outlet pressure	Gauge pressure: 0 Pa; Temperature range: 5–25 °C (278.15–298.15 K)
Chamber walls	Wall	Adiabatic condition (no heat flux)

Manikin's head	Wall (constant-T)	Surface temperature: 30–35 °C (303.15–308.15 K)

New empirical correlations were developed to express the temperature dependence of key thermodynamic properties using a curve-fitting approach. This method was adopted to ensure continuous, smooth property variation across the temperature ranges relevant to the present experimental and numerical investigations. Discrete property data obtained from standard references were first evaluated over the operating temperature interval, and polynomial regression techniques were then applied to obtain best-fit expressions. The resulting correlations provide analytical relationships that accurately capture nonlinear temperature effects while remaining computationally efficient for implementation within the CFD solver as shown below:

$$\mu = 9.585\times 10^{-7} + 7.087\times 10^{-8} \times T - 4.038\times 10^{-11} \times T^2 \tag{4.20}$$

$$\rho = 7.036 - 0.0550\times T + 0.0002\times T^2 - 4.018\times 10^{-7} \times T^3 + 3.008\times 10^{-10} \times T^4 \tag{4.21}$$

$$\boldsymbol{\beta} = 0.014 - 0.000071\times T + 1.618\times 10^{-7} \times T^2 - 1.38\times 10^{-10} \times T^3 \tag{4.22}$$

$$k = 0.001 + 0.00009\times T - 2.601\times 10^{-8} \times T^2 \tag{4.23}$$

$$c_p = 999.672 + 0.023 \times T \tag{4.24}$$

4.1.4 Experimental data and study cases

Following the experimental methodology outlined in Section 3.3, the experimental data collected from the thermal head manikin formed the foundation for model validation and selection in this thesis. The experiments were conducted under carefully controlled chamber conditions, where the skin temperature of the thermal head was maintained at a constant 35 °C to mimic realistic human thermal conditions. A series of test cases were designed to capture the combined influence of ambient air temperature and air velocity on the total heat flux from the head. Specifically, data were recorded for multiple airspeeds ranging from natural convection levels (0.12 m/s) to higher forced convection levels (0.4 m/s), across ambient temperatures spanning 5 °C to 25 °C. The resulting datasets give a detailed view of how heat is distributed across the head surface over space. These measurements captured not only the magnitude of total heat loss but also the influence of flow regime transitions, where buoyancy-driven effects at low velocities were gradually replaced by inertia-driven convection at higher flow rates (see the flow visualization results section). The experimental results demonstrated clear trends: total heat flux increased with both rising air velocity and greater temperature differentials between the head surface and surrounding air, as expected from classical convective heat transfer principles. This high-quality dataset was used directly to calibrate the CFD simulations, ensuring that the selected turbulence model, mesh refinement strategy, and wall boundary conditions were consistent with physical reality. In subsequent validation steps, numerical predictions of convective heat transfer coefficients (h_{conv}) and Nusselt numbers were compared against these experimental benchmarks. The close agreement between experimental observations and simulation outputs confirmed the reliability of the modeling framework, while also highlighting the sensitivity of the system to both air velocity and thermal gradients. As detailed in the study cases presented in this section, this experimental dataset provided the critical link between theory and practice, allowing the development of reliable correlations for mixed convection heat transfer around the human head (see chapter 5). The study case tables 4.3 – 4.6 summarize the comparison between experimental measurements and CFD predictions of the total heat loss from the thermal head (Q_{total}, W/m^2) which revealed important differences depending on the turbulence model and near-wall treatment employed. The accuracy of each configuration is quantified through the absolute relative error, showing that the enhanced wall treatment combined with low-Re turbulence models yielded the closest match to experimental data, while standard wall functions exhibited larger deviations.

Discrepancy of simulated and experimental heat flux was then normalized and regarded as relative percentage difference (RPD), which was determined by the ratio of absolute difference value and experimental value then multiplying these ratios by 100%:

$$\mathrm{RPD} = \frac{|\mathrm{HF_{exp}} - \mathrm{HF}_{CFD}|}{\mathrm{HF_{exp}}} \times 100\% \tag{4.25}$$

Where HF_{exp} stands for experimental heat flux (W/m^2), $\mathrm{HF_{CFD}}$ stands for simulated heat flux (W/m^2).

Table 4.3 Comparison of the results obtained for T_{head} = 308.15 K, T_{air} = 293.15 K, D_{head} = 0.19 m, V_{air}= 0.4, and various flow models and near-wall treatments.

Turbulence Model	Near-Wall Treatment	Q_{total} (CFD) [W/m²]	Q_{total} (Exp Data) [W/m²]	Error (%)
Standard (ST) k–ε	EWT	192.92	194.05	0.58
Standard (ST) k–ε	SWF	236.47	194.05	21.86
Renormalization Group (RNG) k–ε	EWT	193.46	194.05	0.30

Renormalization Group (RNG) k–ε	SWF	226.69	194.05	16.82
Realizable (Rl) k–ε	EWT	192.29	194.05	0.91
Realizable (Rl) k–ε	SWF	222.05	194.05	14.43
Standard (ST) k–ω	NA	180.43	194.05	7.02
Shear-Stress Transport (SST) k–ω	NA	183.93	194.05	5.22
Laminar	NA	179.02	194.05	7.75

Table 4.4 Comparison of the results obtained for T_{head} = 308.15 K, T_{air} = 293.15 K, D= 0.19m, V_{air}= 0.25 and various flow models and near-wall treatments.

Turbulence Model	Near-Wall Treatment	Q_{total} (CFD) [W/m²]	Q_{total} (Exp Data) [W/m²]	Error (%)
Standard (ST) k–ε	EWT	174.77	179.79	2.80
Standard (ST) k–ε	SWF	206.00	179.79	14.60
Renormalization Group (RNG) k–ε	EWT	174.82	179.79	2.76
Renormalization Group (RNG) k–ε	SWF	202.43	179.79	12.60
Realizable (Rl) k–ε	EWT	174.45	179.79	2.80
Realizable (Rl) k–ε	SWF	198.79	179.79	10.57
Standard (ST) k–ω	NA	168.95	179.79	6.02
Shear-Stress Transport (SST) k–ω	NA	169.75	179.79	5.58
Laminar	NA	166.90	179.79	7.17

Table 4.5 Comparison of the results obtained for T_{head} = 308.15 K, T_{air} = 293.15 K, D= 0.19m, V_{air} =0.12 and various flow models and near-wall treatments.

Turbulence Model	Near-Wall Treatment	Q_{total} (CFD) [W/m²]	Q_{total} (Exp Data) [W/m²]	Error (%)
Standard (ST) k–ε	EWT	159.77	161.00	0.76
Standard (ST) k–ε	SWF	180.24	161.00	12.00
Renormalization Group (RNG) k–ε	EWT	160.16	161.00	0.62
Renormalization Group (RNG) k–ε	SWF	174.69	161.00	8.40
Realizable (Rl) k–ε	EWT	159.85	161.00	0.71
Realizable (Rl) k–ε	SWF	172.67	161.00	7.25
Standard (ST) k–ω	NA	160.05	161.00	0.59
Shear-Stress Transport (SST)	NA	160.08	161.00	0.57

k–ω				
Laminar	NA	161.00	161.00	0.00

Table 4.6 Comparison of the results obtained for T_{head} = 308.15 K, T_{air} =288.15 K, D= 0.19m, V_{air} = 0.4, and various flow models and near-wall treatments.

Turbulence Model	Near-Wall Treatment	Q_{total} (CFD) [W/m²]	Q_{total} (Exp Data) [W/m²]	Error (%)
Standard (ST) k–ε	EWT	253.75	249.79	1.58
Standard (ST) k–ε	SWF	312.03	249.79	24.91
Renormalization Group (RNG) k–ε	EWT	253.40	249.79	1.44
Renormalization Group (RNG) k–ε	SWF	297.18	249.79	18.97
Realizable (Rl) k–ε	EWT	252.83	249.79	1.23
Realizable (Rl) k–ε	SWF	293.13	249.79	17.35
Standard (ST) k–ω	NA	237.67	249.79	4.85

Shear-Stress Transport (SST) k–ω	NA	242.22	249.79	3.03
Laminar	NA	237.27	249.79	5.01

The relative error between the RNG k-ε model and experimental data is about 3% when incorporating the full buoyancy effects along with the EWT. The ST k-ε model achieved around the same margin; however, literature suggest the RNG k-ε model has some refinements, such as adding an additional term in the turbulence kinetic energy dissipation rate equation (R_{ε}) as shown in equation (14) above, which improves the accuracy of the RNG k-ε (Shamami and Birouk (2008)). The standard (ST) k-ω turbulence model, which is an empirical model that incorporates modifications for low-Reynolds-number effects, and the laminar model both gave a margin of error less than 1% for low velocities, hence low-Reynolds-numbers. However, for high Reynolds numbers, accuracy becomes a challenge. The following options must be used with the RNG k-ε turbulence model and heat transfer to get consistent results:

- Buoyance effects enabled.
- Near-wall mesh is fine enough to be able to capture the viscous sublayer.
- First cell must be located such that y+ equal 1.
- For complicated geometries, the EWT achieved higher accuracy."

4.1.5 Effect of flow parameters on mixed convection behavior

Simulation and experimental investigations of mixed convection in cross-flow configurations, where the airflow direction is perpendicular (90°) to the gravitational vector, remain relatively limited in the literature. To better understand this complex flow regime, velocity vector plots were generated to visualize airflow behavior around the heated head model for various inlet air velocities. Figures 4.a through 4.e illustrate the flow field development at inlet air velocities of 0.05, 0.12, 0.25, 0.40, and 0.50 m/s, respectively.

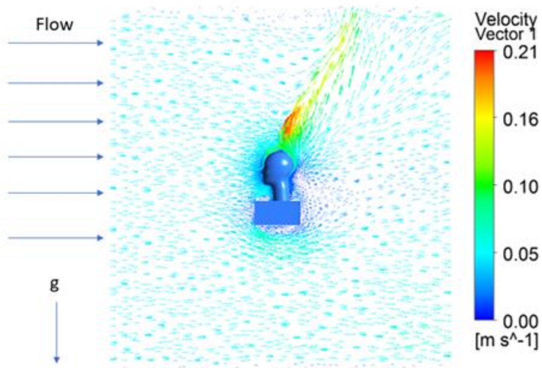

(a)

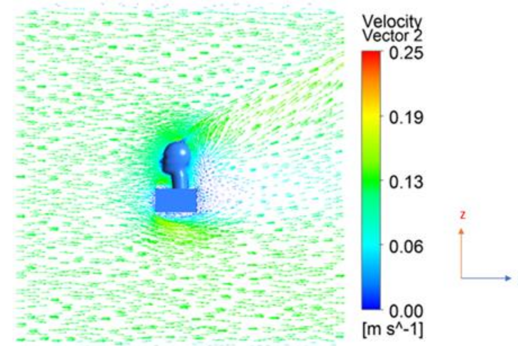

(b)

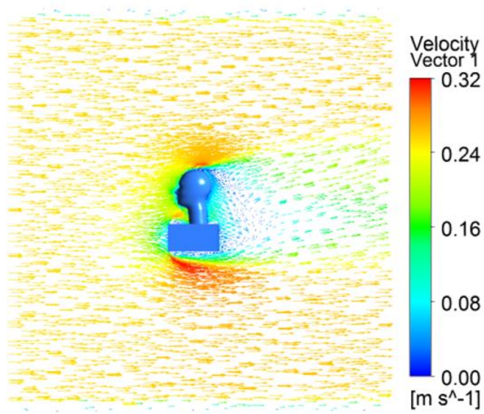

(c)

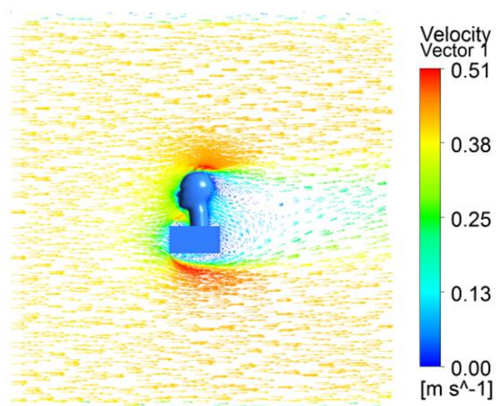

(d)

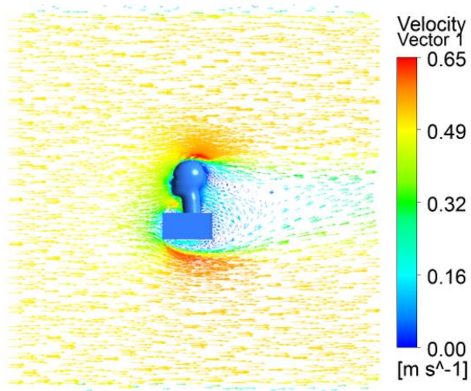

(e)

Figure 4.4: Assisting cross flow over a thermal head, velocity vector map (a) V_air= 0.05m/s, T_air= 293.15K; (b) contours at V_air= 0.12m/s, T_air= 293.15K; (c) contours V_air= 0.25m/s, T_air= 293.15K; (d) contours V_air= 0.4m/s, T_air= 293.15K; (e) contours V_air=

At the lowest air velocity see Figure 4. (a), the buoyancy forces dominate the flow field. The heated air surrounding the head rises due to natural convection, forming a well-defined steady-state thermal plume extending upward. This buoyant plume, however, is slightly inclined from the vertical axis because of the influence of weak forced convection imposed by the cross-flow. The flow pattern reveals the formation of small recirculation zones near the lateral sides of the head, which characterize the transition between pure natural and mixed convection.

As the air velocity increases (Figures 4. (b) – 4. (e)), the influence of forced convection becomes progressively more pronounced. The thermal plume is increasingly deflected downstream, and the buoyancy-induced upward motion is gradually suppressed. At moderate flow velocities, such as 0.25 m/s, a notable interaction between buoyant and inertial forces leads to asymmetric flow separation and an elongation of the recirculation zones located downstream of the head. For higher velocities (≥ 0.40 m/s), inertial forces fully dominate, leading to a pronounced wake region and a flattened thermal boundary layer at the head's upper surface.

At the maximum tested air velocity of 0.50 m/s (Figure 4. (e)), the plume is almost completely aligned with the direction of the cross-flow. The buoyant updraft is replaced by a horizontally driven flow field, and the low-velocity recirculation zones expand downstream, indicating a significant shift from mixed to forced convection dominance. This transition highlights the strong dependence of heat transfer and flow structure on the balance between buoyancy and inertial effects.

4.2 CFD modeling of the standing human body

In the experimental phase, the full-body manikin “Stan,” provided detailed spatial data on convective and radiative heat flux distribution across the body. Airflow was introduced through a controlled inlet wall, ensuring well-defined velocity profiles and minimal turbulence fluctuations in the absence of intentional disturbances.

The experimental results provided two critical inputs for the CFD modeling stage:

1. Boundary condition calibration: Measured zone surface temperatures from the manikin were directly applied as thermal boundary conditions in the CFD simulations. This eliminated uncertainty about the skin temperature distribution and ensured that the numerical model operated under precisely the same thermal driving forces as the physical experiments.
2. Mesh refinement strategy: The spatial resolution of measured heat flux patterns revealed where the largest local gradients occurred such as along the forehead, ears, and back of the neck for the head model. These regions were specifically targeted for localized mesh refinement in the CFD domain, ensuring that the numerical model could capture subtle but important differences in heat transfer between anatomical zones.

4.2.1 Integration of shrink-wrap and 3D scanning for manikin geometry development

The three-dimensional geometry of the nude standing thermal manikin was carefully developed by integrating two complementary approaches, ensuring both physical accuracy and computational robustness for CFD simulations. The first approach relied on the shrink-wrap function in ANSYS SpaceClaim to generate a smooth, continuous envelope around the raw 3D geometry of the manikin. This step was particularly important because the initial CAD model contained discontinuities, gaps, and irregular features around anatomically complex areas such as the joints, which would otherwise hinder high-quality mesh generation. Through shrink-wrapping, followed by post-processing operations such as hole filling, surface merging, and smoothing, a watertight and mesh-compatible surface was achieved. The second approach involved direct 3D body scanning of the manikin using high-resolution scanning technologies combined with Geomagic Studio and SpaceClaim. This process captured fine-scale anatomical features of the manikin while minimizing geometric distortions. The scans were cleaned to remove noise, patched in regions with missing data, and reduced in data density to create a computationally manageable yet physically accurate model. By combining these two approaches, the shrink-wrap ensured numerical stability and meshing efficiency, while the 3D scans preserved critical surface details and geometric fidelity of the average adult male representation. The integration of both techniques ultimately enhanced the validity of the CFD models by providing geometry capable of capturing localized convective and radiative heat transfer effects around key body regions, including the head, torso, and extremities.

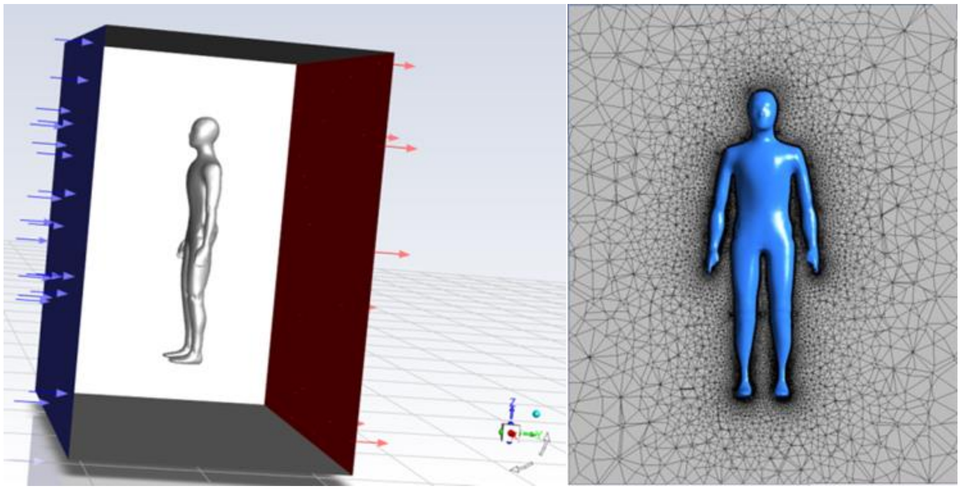

Figure 4.5 3D model of the chamber and thermal Manikin.

The numerical modeling in this thesis was performed using ANSYS FLUENT (version 2020 R2, Ansys Inc.) see Figure 4.5, a finite-volume based computational fluid dynamics (CFD) solver. A steady-state model was developed to simulate the coupled fluid flow and heat transfer phenomena occurring inside the environmental chamber during thermal manikin testing.

Mesh refinement was applied in regions of high temperature and velocity gradients most notably, the immediate area of the manikin surface where accurate resolution of boundary layer behavior was critical. The final mesh configuration contained approximately 828,992 nodes and 4 million elements.

Near-wall treatment played a central role in the simulation accuracy. To fully resolve the viscous sublayer, the non-dimensional wall distance (y^+) for the first grid point adjacent to the manikin surface was maintained close to $y^+ \approx 1$, with 10 inflation layers applied in the wall-normal direction as shown in Figure 4.5. This configuration allowed proper capture of velocity and temperature gradients in the near-wall region and improved prediction of local heat transfer coefficients.

For turbulence modeling, the realizable k–ε model with Enhanced Wall Treatment (EWT) was selected. This approach combines the advantages of resolving near-wall flows with the robustness of wall functions, making it suitable for the mixed convection regime and the low-to-moderate Reynolds number flows encountered in the experiments.

Boundary conditions were set to replicate the experimental environment. The inlet was assigned a uniform velocity profile and a prescribed air temperature matching the controlled chamber settings. The outlet employed a pressure-outlet boundary condition with zero gauge pressure. All solid walls were modeled with no-slip conditions, and the manikin's skin surface was assigned a constant temperature (35 °C) to represent typical human skin conditions.

Numerical schemes included a second-order upwind discretization for convective terms to minimize numerical diffusion, and the coupled pressure-velocity solver for stable and efficient convergence in steady-state simulations. Under-relaxation factors for momentum, turbulence, and energy were set between 0.1 and 0.5 to ensure stable iteration behavior. Convergence was defined by a residual tolerance of 10^{-6} for all governing equations, combined with monitoring of heat flux stability over successive iterations.

Radiative heat transfer was included due to its significant contribution up to 50% of total heat loss from the manikin surface under certain conditions. The Discrete Ordinates Model (DOM) was employed to solve the Radiative Transfer Equation (RTE) across the computational domain. Given that the manikin surface was discretized into millions of finite elements, calculation of the radiation view factors required substantial computational time and memory resources.

Empirical polynomial correlations for all thermophysical properties of air including density, viscosity, thermal conductivity, specific heat, and thermal expansion coefficient (temperature dependent properties) were developed using curve fitting to experimental property data.

Chapter 5. Empirical Correlation Development for the Head Model

5.1 Derivation of empirical correlation

One of the objectives of this study was to develop simplified empirical models that could reliably represent the computational fluid dynamics (CFD) results obtained for convective heat transfer from the thermal head. The goal was to refine the numerical data into compact correlations that are both physically meaningful and practically useful for engineering applications. To achieve this, the Buckingham π-Theorem was applied, which provides a systematic framework for identifying the governing nondimensional parameters in a physical problem. This theorem is particularly effective for heat transfer studies, as it reduces the number of variables into a set of dimensionless groups that capture the underlying physics.

For the case of forced convection heat transfer from the head, the relevant variables are determined by considering the effects of geometry, environmental conditions, and fluid thermophysical properties. The heat transfer coefficient "h" is a function of the following independent variables:

$$h = f\,(\rho, \mu, v, k, Cp, D) \tag{5.1}$$

Where, ρ is fluid density, μ is kinematic viscosity, v is fluid velocity, k is thermal conductivity of fluid, c_p is specific heat of fluid, and D is the characteristic diameter of the head. Here, h is the dependent variable, while the others serve as independent variables.

According to Buckingham's π-Theorem, the heat transfer problem can be represented in terms of dimensionless π-groups. The choice of repeating variables is critical to ensuring that these groups capture the physics of the system. In this study:

- D (diameter) was selected to represent geometry.

- V (velocity) was selected to represent flow conditions.
- ρ, μ, and c_p were used to capture fluid properties.

By systematically combining the repeating variables with the remaining quantities, the following dimensionless groups emerge:

Nusselt number: $Nu = \frac{hD}{k}$ (ratio of convective to conductive heat transfer).

Reynolds number: $Re = \frac{\rho v D}{\mu}$ (ratio of inertial to viscous forces).

Prandtl number: $Pr = \frac{\mu c_p}{K}$ (ratio of momentum diffusivity to thermal diffusivity).

This yields the general forced convection relationship:

$$Nu = \phi\ (Re, Pr) \tag{5.2}$$

The physical properties of air were evaluated at the film temperature; $T_f = (T_{head} + T_{air})/2$.

In this thesis, Reynolds numbers ranged from 500 to 7,000, spanning laminar, transitional, and low-turbulent regimes. The Prandtl number remained nearly constant at 0.72 for the 5–35 °C temperature range. A power-law form was adopted for the correlation, following conventional forced convection studies:

$$Nu_{forced} = C_1\ Re^{n2}\ Pr^{n1} \tag{5.3}$$

Here, C_1 and exponents "n1" and "n2" are empirical constants determined by curve-fitting to CFD results (see Table 5.1).

Table 5.1 Summary of CFD simulation cases for the thermal head: input conditions, Reynolds Numbers, heat transfer coefficients, and Nusselt Numbers.

Case	$T_{skin-head}$ (K)	T_{air} (K)	D_{head} (m)	V_{air} (m/s)	Re	h_{conv} (W/m²·K)	Nu_{num}
1	303.15	298.15	0.19	0.05	5.99E+02	3.09	2.28E+01
2	308.15	298.15	0.19	0.05	5.90E+02	3.48	2.56E+01
3	308.15	293.15	0.19	0.05	5.99E+02	3.8	2.81E+01
4	308.15	288.15	0.19	0.05	6.08E+02	4.04	3.01E+01
5	303.15	278.15	0.19	0.05	6.35E+02	4.3	3.27E+01
6	308.15	278.15	0.19	0.05	6.26E+02	4.49	3.40E+01
7	308.15	298.15	0.19	0.12	1.44E+03	6.0	2.75E+01
8	308.15	298.15	0.19	0.12	1.42E+03	6.0	2.99E+01
9	308.15	293.15	0.19	0.12	1.44E+03	6.0	3.19E+01
10	308.15	288.15	0.19	0.12	1.46E+03	6.0	3.37E+01
11	308.15	278.15	0.19	0.12	1.53E+03	6.0	3.61E+01
12	308.15	278.15	0.19	0.12	1.50E+03	6.0	3.70E+01
13	308.15	298.15	0.19	0.25	2.99E+03	6.0	3.66E+01
14	308.15	298.15	0.19	0.25	2.95E+03	6.0	3.75E+01
15	308.15	293.15	0.19	0.25	2.99E+03	6.0	3.90E+01
16	308.15	288.15	0.19	0.25	3.04E+03	6.0	4.08E+01
17	308.15	278.15	0.19	0.25	3.18E+03	6.0	4.31E+01
18	308.15	278.15	0.19	0.25	3.13E+03	6.0	4.38E+01
19	308.15	298.15	0.19	0.35	4.19E+03	6.0	4.38E+01
20	308.15	298.15	0.19	0.35	4.13E+03	6.0	4.40E+01
21	308.15	293.15	0.19	0.35	4.19E+03	6.0	4.51E+01
22	308.15	288.15	0.19	0.35	4.25E+03	6.0	4.62E+01
23	308.15	278.15	0.19	0.35	4.45E+03	6.0	4.81E+01
24	308.15	278.15	0.19	0.35	4.38E+03	6.0	4.84E+01
25	308.15	298.15	0.19	0.4	4.79E+03	6.0	4.72E+01
26	308.15	298.15	0.19	0.4	4.72E+03	6.0	4.72E+01
27	308.15	293.15	0.19	0.4	4.79E+03	6.0	4.82E+01
28	308.15	288.15	0.19	0.4	4.86E+03	6.0	4.92E+01
29	308.15	278.15	0.19	0.4	5.08E+03	6.0	5.11E+01
30	308.15	278.15	0.19	0.4	5.01E+03	6.0	5.12E+01
31	308.15	298.15	0.19	0.5	5.99E+03	6.0	5.38E+01
32	308.15	298.15	0.19	0.5	5.90E+03	6.0	5.35E+01
33	308.15	293.15	0.19	0.5	5.99E+03	6.0	5.44E+01
34	308.15	288.15	0.19	0.5	6.08E+03	6.0	5.52E+01
35	308.15	278.15	0.19	0.5	6.35E+03	6.0	5.73E+01
36	308.15	278.15	0.19	0.5	6.26E+03	6.0	5.71E+01
37	308.15	298.15	0.169	0.25	2.62E+03	6.0	3.54E+01
38	308.15	293.15	0.169	0.4	4.25E+03	6.0	4.51E+01

39	308.15	288.15	0.169	0.12	1.29E+03	6.0	3.11E+01
40	308.15	278.15	0.169	0.35	3.95E+03	6.0	4.48E+01
41	308.15	288.15	0.169	0.4	4.32E+03	6.0	4.58E+01
42	308.15	278.15	0.169	0.12	1.33E+03	6.0	3.40E+01

Table 5.1 presents the numerical results (44 cases) obtained from the CFD simulations for the thermal head model under various air velocities and temperature differences. The convective heat transfer coefficient (h_{conv}) and the corresponding average Nusselt number (Nu_{numer}) both exhibit a clear increasing trend with higher air velocity (V_{air}) and greater temperature difference (T_{head}–T_{air}). Specifically, the Nusselt number increased from approximately 22.8 at 0.05 m/s to about 57.1 at 0.5 m/s, indicating enhanced convective transport under stronger forced convection. The corresponding Reynolds number varied between 5.9×10^2 and 6.35×10^3, spanning the transition from laminar to turbulent mixed-convection regimes. For a head model, transition is gradual. Laminar flow dominates below Re ≈ 500, a transitional mixed regime exists between 500 and 3,000, and fully turbulent wakes occur above about Re ≈ 4,000–5,000. These trends align closely with the theoretical expectations and experimental observations discussed earlier in Chapter 3 (Experimental Validation) and Chapter 5 (Nusselt Number Correlation Development), providing strong evidence for the reliability of the adopted CFD modeling approach and mesh resolution strategy.

For pure natural convection, the velocity field is induced mainly by buoyancy forces rather than external flow. The relevant variables include the gravitational constant and thermal expansion effects:

$$h = f(\rho, \mu, k, Cp, D, \Delta T, \beta, g) \tag{5.4}$$

Where "g" is gravitational constant, "β" is volumetric expansion coefficient, and "α" is thermal diffusivity. However, in free convection, (ΔT β g) will be treated as single parameter as the velocity of fluid particles is a function of these three parameters. $\Delta T = (T_{head} \quad T_{air})$ is temperature difference driving buoyancy. Applying Buckingham's π-Theorem leads to:

$$Nu = \phi\ (Pr, Gr) \tag{5.5}$$

Where the Grashof number is given by:

$$Gr = \frac{g\beta(T_h - T_c)D^3}{v^2} \tag{5.6}$$

The Grashof number represents the ratio of buoyancy to viscous forces. Increasing ΔT increases Gr, leading to stronger natural convection and a thinner thermal boundary layer. The natural convection Nusselt number correlation was assumed to follow:

$$Nu_{natural} = C_2\ Pr^{n3}\ Gr^{n4} \tag{5.7}$$

Here, C_2 and exponents "n3" and "n4" are obtained from regression analysis of simulation results.

$$H = f\,(\rho, \mu, k, c_p,\ D, (\Delta T\ \beta\ g), v) \tag{5.8}$$

The average Nusselt number becomes a function of three dimensionless parameters:

$$Nu = \varphi\ (Re, Gr, Pr) \tag{5.9}$$

Deriving a universal form for the equation above is challenging due to the complex interaction between natural and forced convection. However, based on literature trends and the present CFD data (Churchill & Bernstein, 1977; Metais & Eckert, 1964; Raju et al., 1984), a composite power-law model was adopted:

$$Nu = (\ Nu_{forced}^{m} \ \pm\ Nu_{natural}^{m}\ )^{1/m} \tag{5.10}$$

In this equation the plus sign is used for buoyancy-assisting flows, where natural convection enhances forced convection. The minus sign applies to buoyancy-opposing flows, where natural convection resists the forced flow. The exponent m determines the degree of interaction between the two modes. The simulations in this study covered a broad range of conditions:

Reynolds number: $500 \leq Re \leq 7{,}000$

Grashof number: $4.45 \times 10^6 \leq Gr \leq 2.99 \times 10^7$

Prandtl number: $Pr = 0.72$

Richardson number: $0.13 \leq Ri \leq 40$

The resulting correlation allows accurate estimation of the average Nusselt number across laminar, transitional, and turbulent mixed-convection regimes.

The CFD simulations produced a broad dataset characterizing the convective heat transfer behavior of the head under different environmental conditions as shown in Table 5.1. With the head surface maintained at 35 °C, simulations spanned temperature differences between the head and ambient air ranging from 5 °C to 30 °C and inlet air velocities from 0.05 m/s up to 0.5 m/s. The calculated convective heat transfer coefficient h_{conv} values increased systematically with both greater air velocity and larger temperature differences, as expected for mixed convection. For example, at the lowest velocity of 0.05 m/s, h_{conv} values ranged from about 3.1 to 4.5 W/m²·K depending on the temperature difference, while at the highest velocity of 0.5 m/s, coefficients rose to above 7.5 W/m²·K. These variations directly translated into Nusselt number trends: values ranged from roughly 23 at the lowest velocities to above 57 at the upper range of air speed, demonstrating the strong velocity dependence of forced convection.

The data also revealed that Reynolds numbers spanned from approximately 600 at 0.05 m/s up to nearly 6,000 at 0.5 m/s, covering both laminar and transitional flow regimes. Importantly, the numerical Nusselt number predictions were consistent with established heat transfer theory, showing monotonic increases with Reynolds number and validating the methodology applied in the mesh refinement and turbulence modeling. Cases with reduced head diameter (D=0.169 m) demonstrated slightly higher h_{conv} values for comparable Reynolds numbers, confirming the role of geometry in modulating convective transport.

5.2 Validation and error analysis

Based on the present numerical simulation results, a new empirical correlation was derived for the average Nusselt number in terms of the Grashof number (Gr), Reynolds number (Re), and Prandtl number (Pr). The correlation is specifically developed for predicting the average Nusselt number at the surface of the thermal head located at the center of the environmental chamber, under mixed convection conditions. The proposed general form is:

$$\mathrm{Nu} = ((C_1\, Pr^{n1}\, Re^{n2})^m + (C_2\, Pr^{n3}\, Gr^{n4})^m)^{1/m} \tag{5.11}$$

Many previous studies have examined external forced and natural convection from different geometries such as flat plates, infinite circular cylinders, and spheres. However, the geometry of a human head introduces unique curvature effects, complex stagnation regions, and localized boundary layer interactions that cannot be directly addressed by such canonical correlations. The numerical dataset used for the fitting process covered a wide range of conditions:

- Reynolds number: $500 \leq \mathrm{Re} \leq 7{,}000500$
- Grashof number: $4.45\times 10^6 \leq \mathrm{Gr} \leq 2.99\times 10^7$
- Prandtl number: Pr = 0.72 (evaluated at the film temperature)

The optimized correlation for mixed convection heat transfer is:

$$\mathrm{Nu}_{mixed} = ((0.37 * Re^{0.58} * Pr^{\frac{1}{3}})^3 + (0.485 * Gr^{\frac{1}{4}} * Pr^{\frac{1}{4}})^3)^{\frac{1}{3}} \tag{5.12}$$

To address these complexities, the Generalized Reduced Gradient (GRG) optimization method was employed to fit the correlation to our numerical dataset. The GRG method is designed for solving nonlinear equation systems, with the objective function defined to minimize the sum of squared residuals between the CFD-predicted Nusselt numbers and the values calculated from the proposed correlation. Here, the residual represents the difference between the observed simulation point and the predicted value, and minimizing this quantity ensures that the fitted correlation provides the closest possible match across all tested conditions. To validate the proposed correlation, its predictions were compared to:

1. CFD results from 44 simulation cases covering different combinations of air velocity, ambient temperature, and head surface temperature.
2. Experimental data collected from the environmental chamber measurements using the segmented thermal head manikin.

Validation was performed by computing the Root Mean Square Error (RMSE) and Mean Absolute Percentage Error (MAPE):

$$\mathrm{RMSE} = \sqrt{\frac{1}{N}\sum_{i=1}^{N}(Nu_{pred,i} - Nu_{ref,i})^2} \tag{5.13}$$

Where $Nu_{pred,i}$ is the correlation prediction, $Nu_{ref,i}$ is the CFD or experimental value, and N is the total number of cases.

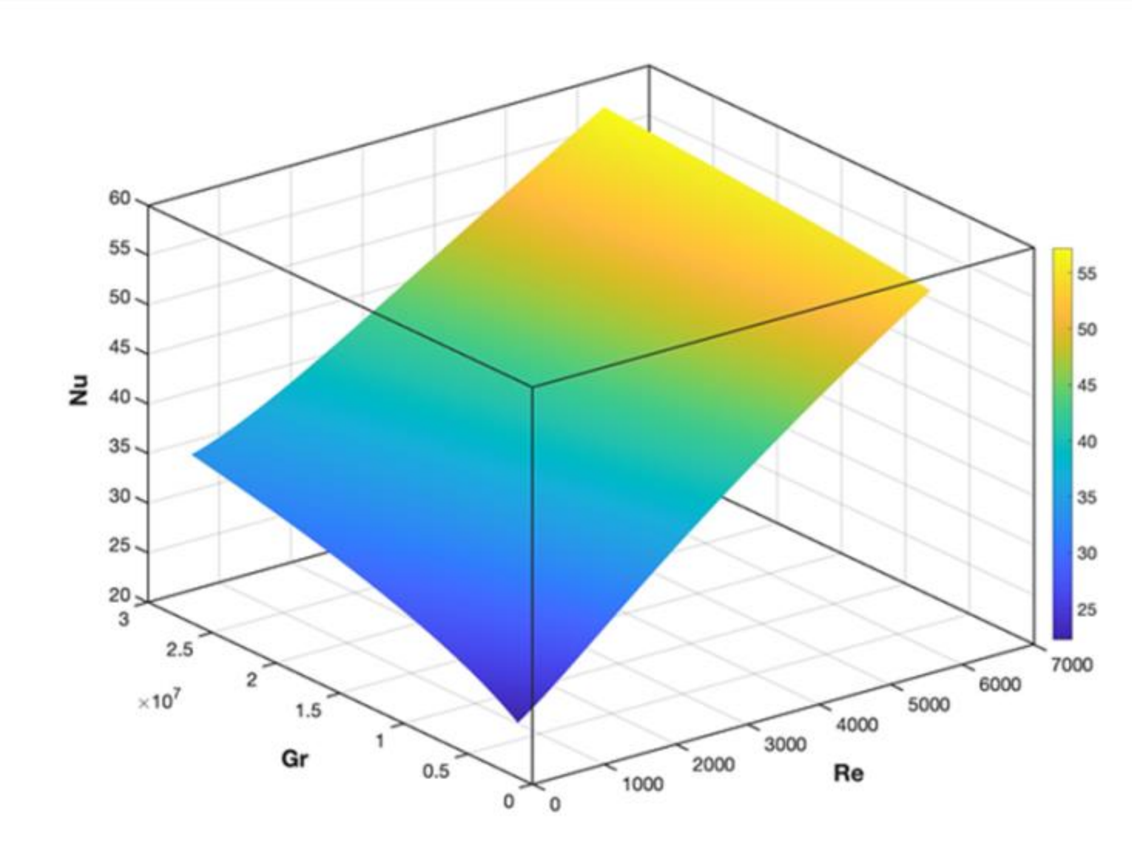

Figure 5.1 The predicted average Nusselt number at the head's surface versus Reynolds Numbers and Grashof Numbers. Pr = 0.72.

Figure 5.1 compares the predicted average Nusselt numbers from the proposed correlation with reference values obtained from both CFD simulations and experimental measurements across the studied ranges of Reynolds and Grashof numbers. The predicted CFD values exhibit strong agreement with the benchmark data, with most points closely clustering along the 1:1 parity line, confirming the accuracy of the developed correlation in capturing mixed convection behavior. Quantitatively, the root mean square error (RMSE) between CFD and correlation results was 1.42 for forced-convection-dominant cases and 1.97 for mixed-convection-dominant cases. Similarly, the RMSE between experimental and correlation results was 1.85 and 2.35 for the respective regimes. Slightly greater scatter was observed at low air velocities within the mixed convection range, where buoyancy and forced flow act in partially opposing directions. This deviation is consistent with established observations of flow instabilities and localized separation zones typical of opposing buoyancy configurations in mixed convection systems.

5.3 Discussion of practical implications

Figure 5.2 illustrates the variation of the convective heat transfer coefficient (h_c) as predicted by the CFD simulations across a range of temperature differences $(T_{head} - T_{air})$ and airflow velocities. The results clearly demonstrate that h_c increases progressively with both rising temperature difference and air velocity, confirming the expected behavior for mixed convection heat transfer. At low air velocities (e.g., 0.05 m/s), buoyancy forces dominate, resulting in relatively modest convective coefficients. However, as the air velocity increases up to 0.5 m/s, forced convection effects become increasingly pronounced, significantly enhancing convective heat transfer at the head's surface.

As the temperature difference between the head surface and ambient air rises from 5°C to 30°C, the thermal driving potential across the boundary layer increases, intensifying buoyancy-induced motion near the surface. This, combined with higher momentum transport from stronger airflow, leads to a pronounced increase in $h_c$values. The results align closely with theoretical and empirical findings in convective heat transfer literature, where both the Reynolds number (representing inertial forces) and the Grashof number (representing buoyancy effects) contribute to the overall heat exchange rate. The smooth gradient of h_c observed in the simulations further validates the accuracy of the turbulence model and near-wall treatment employed, confirming that the CFD framework successfully captures the transition between natural and forced convection regimes.

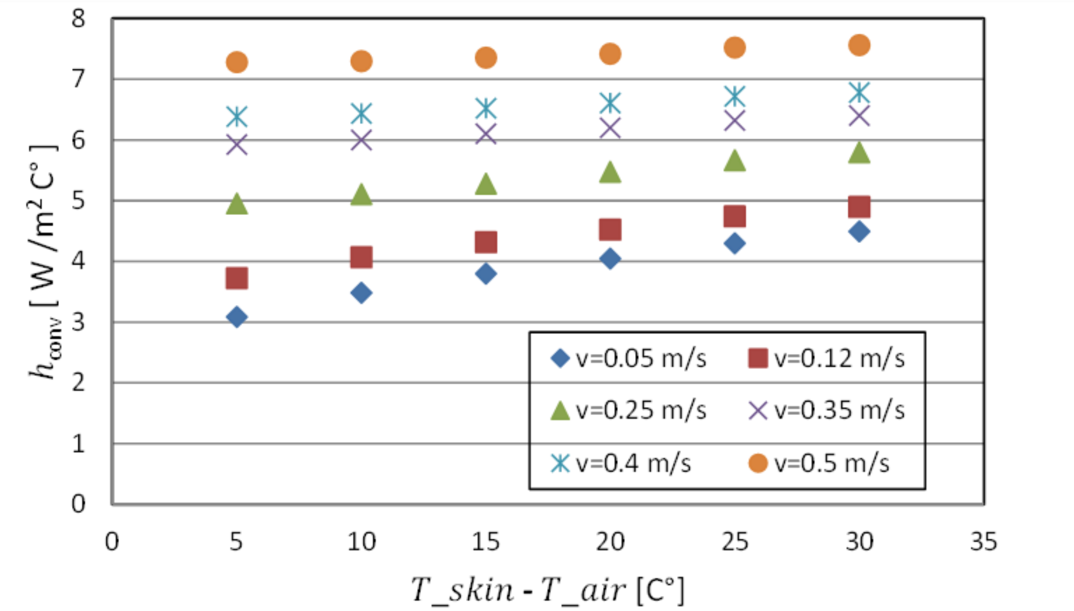

Figure 5.2 Convective heat transfer coefficients (h_c) using the CFD method for different ($T_{head} - T_{air}$).

To validate the CFD methodology and the regression-based correlation developed in this thesis, five experimental cases were conducted under comparable boundary conditions. The experimentally determined h_c values were then compared directly with CFD predictions. The results demonstrate strong agreement, providing confidence in the accuracy of both the numerical model and the regression formulation for practical predictive applications.

The convective heat transfer coefficient for the human head has been investigated by numerous researchers (Sørensen & Voigt, 2003; De Dear, Arens, Hui, & Oguro, 1997; Silva & Coelho, 2002; Yang, Kato, Hayashi, & Murakami, 2004), but published values show substantial variability. This inconsistency is largely due to the complex interplay of environmental and geometric factors, including:

- Air velocity and turbulence intensity in the surrounding flow.
- Airflow direction relative to head geometry.
- Surface temperature distribution on the head.
- Presence of hair or other coverings, which can act as a thermal and aerodynamic shield.

Table 5.2 presents a comparative summary of convective heat transfer coefficients (h_c) for the human head under still-air conditions, combining results from the present CFD–experimental approach with those reported in earlier studies. Overall, the convective coefficients obtained in this study align well with the ranges established in prior research, confirming both the validity of the numerical model and the representativeness of the experimental data. Specifically, the $h_c$values predicted here are in close agreement with those reported by Sørensen and Voigt (2003) and De Dear et al. (1997), who analyzed seated and semi-still human subjects using both CFD simulations and controlled laboratory experiments. Their findings, which reported convective coefficients around 3.6–3.7 W/m²•°C, are nearly identical to the current study's value of approximately 3.8 W/m²•°C at a similar ambient air velocity and surface temperature, indicating that the thermal boundary conditions and near-wall treatments adopted in the CFD framework accurately capture physical behavior around the head.

In contrast, Silva and Coelho (2002) reported substantially lower h_c values approximately 26% lower than those obtained here. This discrepancy can be attributed to the physical characteristics of their experimental setup, notably the presence of hair on the thermal manikin, which served as an insulating layer that reduced convective heat exchange. In addition, their configuration allowed for backflow effects near the rear of the head, generating localized zones of low velocity and reduced turbulence intensity. These effects act as a "shielding mechanism," diminishing the overall convective efficiency by impeding air renewal at the surface. Yang et al. (2002), on the other hand, reported higher h_c values (≈6.2 W/m²•°C), which they associated with enhanced turbulence and localized flow acceleration over the forehead region in their indoor environment experiments.

Table 5.2 Comparison of the convective heat transfer coefficients h_c of a human head in still air.

Researchers	Year	Approach	Ambient air velocity m/s	Air temperature C°	$\mathrm{h_c}$ W/m^2 C°
Sørensen and Voigt	2003	CFD	Stagnant	20	3.62
De Dear et al.	1997	Experiment	> 0.1	20.4	3.7
Silva and Coelho	2002	Experiment	> 0.05	20	0.6
Yang et al.	2002	Experiment	Stagnant	20	6.2
Present study		CFD + Experiment	0.05	20	3.8

The present CFD–experimental results fall well within the midrange of these previously published values, reinforcing the robustness of the adopted turbulence model and near-wall treatment in replicating realistic heat transfer behavior. It is noteworthy that the predicted h_c values for the head are also consistent with generalized correlations for the whole human body, such as those presented in the ASHRAE Handbook of Fundamentals (2017), which specify:

$$h_c = 4.0 \qquad \text{for } 0 < v_{air} < 0.15 \text{ m/s} \tag{5.14}$$

$$h_c = 14.8\, v_{air}^{0.69} \qquad \text{for } 0.15 < v_{air} < 1.5\text{m/s.} \tag{5.15}$$

Numerous studies over the past decades have sought to determine appropriate convective heat transfer coefficients $(\mathrm{h_c})$ for the whole human body under various environmental and posture conditions (De Dear et al., 1997; Ichihara et al., 1995; Murakami et al., 2000; Topp et al., 2002; Danielsson, 1993; Brohus, 1997). Reported values vary considerably, a reflection of the fact that convective heat transfer from the human body to its surroundings is influenced by multiple interrelated factors, including air velocity, ambient air temperature, flow direction, and turbulence intensity. These factors interact with the body's geometry and surface temperature distribution, producing significant variability in experimental and numerical results as shown in Table 5.3.

Table 5.3 Comparison of the mean convective heat transfer coefficients h_c of a human body.

Researchers	Year	Approach	Ambient air velocity m/s	Posture	h_c $W\ m^{-2}\ {}^{\circ}C^{-1}$
Fanger	1970	Experimental	Stagnant	Standing	4.4
Danielsson	1993	Experiment	Stagnant	Standing	3.6
Murakami et al	1997	CFD	<0.12	Standing	4.3
De Dear et al	1997	Experiment	< 0.1	Standing	3.4
			0.2 < v < 0.8		$10.3v^{0.6}$
Brohus	2001	Experiment	<0.05	Standing	3.86
Sørensen and Voigt	2003	CFD	Stagnant	Seated	3.13
ASHRAE Handbook	2017	Seppänen et al	0.15< v <1.5	Standing	$14.8v^{0.69}$
Present study		CFD + Experiment	0.05	Standing	4.05
			0.35		7.09

This thesis's predictions are in close agreement with values reported by Fanger (1970), Murakami et al. (1997), and Brohus (2001), specifically for the standing posture. Table 5.3 summarizes representative literature values and compares them with the results of this work. For natural convection, the whole-body h_c obtained in this thesis was 3.76 W/m²·K, which lies in the mid-range of previously published results for the standing posture. In the forced convection regime, the predicted h_c values were noticeably higher, as expected due to the enhanced contribution of inertial forces over buoyancy forces. The close alignment between the present study's predictions and established literature values lends confidence to the CFD–experimental methodology applied here. In stagnant or low-velocity conditions, predicted coefficients are in the same range as the classic results of Fanger and Murakami, both widely referenced in thermal comfort and human heat balance studies. At higher velocities, the results match the increasing trend described by ASHRAE's velocity-dependent correlations, confirming that the model accurately captures the velocity dependence of convective heat transfer.

Experimental measurements of h_r for the standing human body have been reported by Ichihara et al. (1995) , who used a simplified human geometry in their radiative heat transfer simulations. Their estimated h_r value of 4.3 $W/m^2{\cdot}K$ is slightly lower but remains well within the expected range and is consistent with both the ASHRAE reference and the results from this thesis. Such agreement across independent sources suggests that the thermal radiative exchange properties of the human body are relatively stable across a variety of modeling approaches, provided surface emissivity and environmental parameters are defined accurately.

In summary, this thesis's estimates for both convective and radiative heat transfer coefficients for the whole human body are in strong agreement with established literature values, confirming the validity of the simulation approach and parameterization (The emissivity of the skin surface was assumed to be constant and equal to 0.98 for all simulations). These findings provide a reliable foundation for extending the analysis to segmental heat transfer, such as that from the head, under varying environmental conditions.

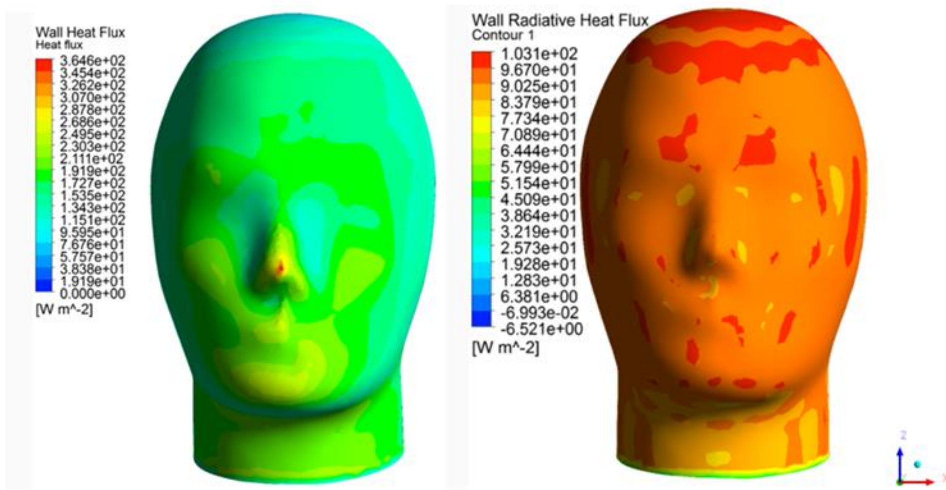

(a) (b)

Figure 5.3 (a) The total heat flux estimated by FLUENT (b) the radiative heat flux distribution on the head surface at T_{head}= 35 C°, T_{air}= 20 C° and V_{air}= 0.4 m/s.

CFD simulations also provide detailed spatial distributions of total heat flux and radiative heat flux on the head surface (Figure 5.3). The total heat flux is highly non-uniform, ranging from approximately 68 W/m² in lower exchange zones to as high as 364 W/m² at the tip of the nose (Figure 5.3 A). This concentration at the nose is expected, as protruding features tend to experience both higher convective exposure and more intense radiative exchange with the surrounding environment.

The radiative heat flux accounts for up to 50% of the total heat loss from the head and similarly exhibits spatial variation, ranging from 36 W/m² to 103 W/m² (Figure 5.3 B). These findings underscore the necessity of including radiation models in CFD simulations of human thermal environments, especially for detailed segmental heat balance studies.

While the proposed correlation demonstrates strong predictive capability for the human head geometry under the tested conditions, it is important to recognize the inherent limitations of empirical correlations:

- They are valid only within the tested parameter ranges of Re, Gr, and Pr.
- They are geometry-specific, meaning that applying the same correlation to drastically different shapes (e.g., flat plates, spheres, or clothed bodies) would require recalibration.
- Radiation effects, while included in CFD, are not explicitly parameterized in the final form of the correlation and are implicitly embedded within the fitted constants.

No previous research has modeled heat transfer from the human head under realistic environmental conditions using this combined CFD-experimental approach. The proposed correlation therefore represents a novel, geometry-specific, and validated tool for predicting mixed convection heat transfer from the human head in indoor environmental conditions.

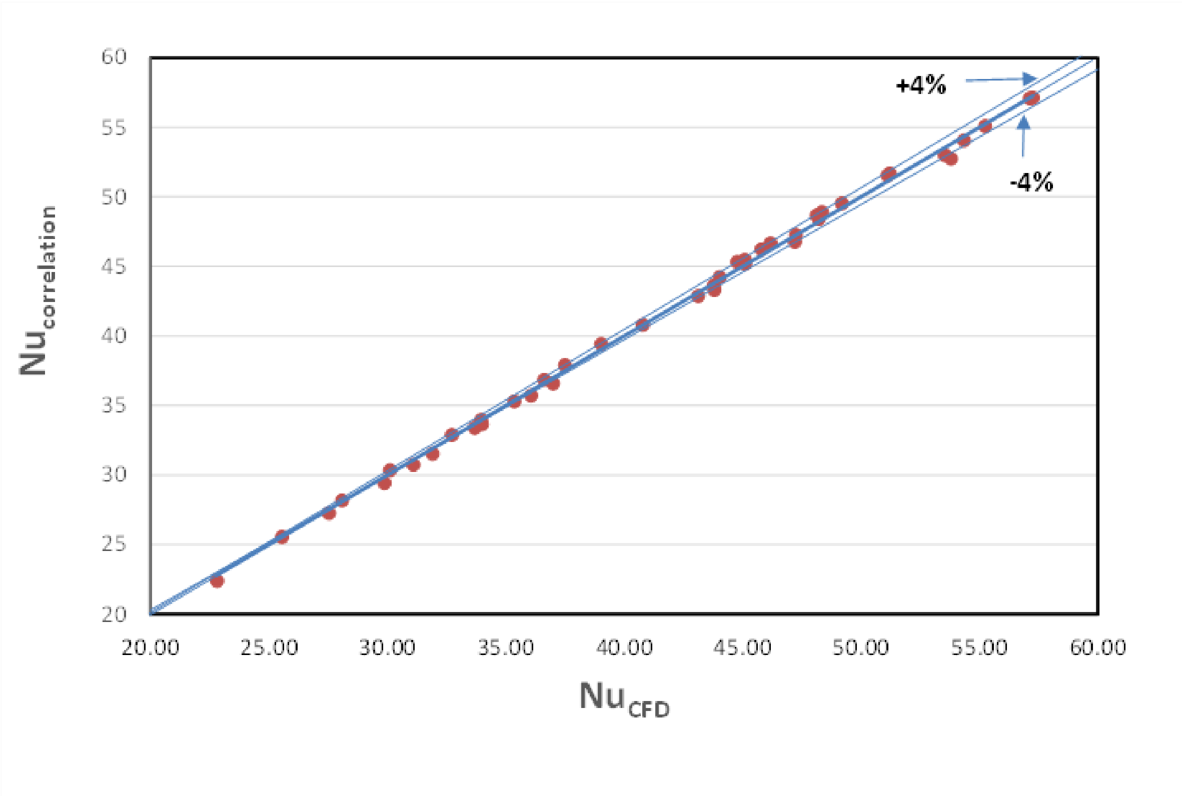

Figure 5.4 The predicted average Nusselt number at the head's surface (correlation) versus calculated average Nusselt number (CFD).

The predicted values from the new mixed-convection correlation demonstrate excellent agreement with CFD results, with a relative percentage difference (RPD) within ±2% for all studied cases (see Figure 5.4). The RPD was calculated using:

$$\mathrm{RPD} = \frac{|Nu_{CFD} - Nu_{corr}|}{CFD_{CFD}} \times 100\% \tag{5.15}$$

In addition to low RPD values, the sum of squared residuals (SSR) a measure of the overall discrepancy between CFD-predicted and correlation-predicted values was found to be 4.62, indicating a tight fit and minimal predictive error. This combination of low RPD and small SSR confirms the accuracy and stability of the proposed correlation over the tested range.

The Richardson number (Ri) serves as a useful non-dimensional parameter for quantifying the relative importance of buoyancy (natural convection) versus inertial forces (forced convection):

- Ri < 0.01: Free convection effects negligible; forced convection dominant.
- Ri < 1: Forced convection predominant.
- Ri > 10: Natural convection predominant.
- 0.1 < Ri < 10: Mixed convection regime neither forced nor natural convection is negligible.

These classification baselines are consistent with the findings of Yuge (1960), and they were used to evaluate the present dataset. For data points with Ri >10, buoyancy forces dominated the heat transfer process, and the natural convection term in Equation (32) was sufficient to match the mixed convection CFD results. In these cases, the forced convection contribution was minimal.

Table 5.4 summarizes the predicted mixed convection parameters for high Richardson number (Ri > 10) cases, which represent conditions dominated by natural convection. The presented data show the relationship between the Nusselt numbers derived from forced and natural convection correlations and their combined effect in mixed convection. As the Richardson number increases, buoyancy forces become increasingly significant, leading to a stronger contribution from natural convection in the overall heat transfer process. The computed mixed Nusselt numbers ($\mathrm{Nu}_{\mathrm{mixed}}$) demonstrate a smooth transition from forced-dominated to buoyancy-dominated regimes, aligning well with theoretical expectations. This behavior validates the proposed correlation used to predict average Nusselt numbers across different regimes. Notably, the results highlight how combined convection mechanisms interact to determine total heat transfer rates for complex human geometries, an essential consideration when developing semi-empirical correlations applicable to both engineering and physiological thermal modeling.

Table 5.4 Free convection is the dominant when Ri > 10.

Case	$Nu_{forced}=0.37\ Re^{0.58}\ Pr^{\frac{1}{3}}$	$Nu_{natural}=0.485\ Gr^{\frac{1}{4}}\ Pr^{\frac{1}{4}}$	Ri	Nu_{mixed}
1	13.593	20.580	12.399	22.807
2	13.475	24.241	13.046	25.553
3	13.593	27.085	19.768	28.095
4	13.713	29.386	26.627	30.109
5	14.086	31.999	34.326	32.734
6	13.960	33.162	40.768	33.956

In the following, Table 5.5 presents mixed convection cases where both forced and natural convection contributions are comparable (0.1 < Ri < 10), indicating that neither mechanism can be neglected. In this transitional regime, the interaction between buoyancy and inertial forces creates complex flow structures and heat transfer behaviors. The presented data show that as the Richardson number decreases below 10, forced convection begins to play a greater role, while buoyancy remains significant enough to influence the overall Nusselt number. The resulting Nu_{mixed} values fall between those predicted by purely forced and purely natural convection correlations, confirming the mixed convection nature of these conditions. The strong agreement between numerical results and established theoretical correlations demonstrates the reliability of the computational framework in accurately resolving both regimes. These findings bridge the gap between fully buoyancy-driven and inertia-dominated flows, representing the most thermally complex range observed in this study.

Table 5.5 Neither is negligible when 0.1 < Ri < 10.

Case	Nu_{forced}=0.37 $Re^{0.58}$ $Pr^{\frac{1}{3}}$	$Nu_{natural}$= 0.485 $Gr^{\frac{1}{4}}$ $Pr^{\frac{1}{4}}$	Ri	Nu_{mixed}
1	22.585	20.580	1.143	27.541
2	34.876	29.386	1.065	40.786
3	35.825	31.999	1.373	43.134
4	41.656	24.240	0.266	44.028
5	45.405	20.579	0.102	47.208
6	47.053	31.999	0.536	51.133
7	46.629	33.162	0.637	53.535
8	51.678	20.579	0.198	54.356
9	52.135	29.386	0.266	55.247
10	53.554	31.999	0.343	57.251
11	53.073	33.162	0.408	57.131

In several cases with Ri≈1, the interaction between buoyancy and forced flow was particularly strong, resulting in enhanced heat transfer compared to purely additive effects. These results highlight the importance of correctly blending the two mechanisms using the nonlinear superposition form in Equation (5.12), rather than a simple linear sum.

In summary, the findings reinforce the importance of incorporating both buoyancy and inertial contributions when modeling mixed convection heat transfer over complex human geometries. The proposed correlation provides a reliable predictive tool for such applications, with potential adaptability to other irregular geometries under similar environmental conditions.

Chapter 6. Human Thermal Comfort and Clothing Microclimate

Understanding human thermal comfort requires a comprehensive evaluation of the complex heat and mass transfer processes occurring between the skin, clothing, and surrounding air. This chapter integrates experimental and computational findings to examine how clothing insulation, fabric porosity, and fabric thickness influence the thermal balance within the microclimate adjacent to the skin. The study extends beyond whole-body and localized heat transfer analyses presented in earlier chapters, focusing on the interactive role of the clothing system as a semi-permeable barrier that modulates convective, conductive, and radiative heat exchanges. By combining validated CFD models with experimental data, this chapter aims to discuss the mechanisms governing heat and mass transfer through the skin–air–fabric interface and their implications for human thermal comfort under varying environmental and airflow conditions.

As shown in Figure 6.1, a hierarchical modeling strategy was adopted to progressively simplify the geometry from a full-body configuration to a two-dimensional (2D) fabric-covered cylinder, balancing physical realism with computational efficiency. Full-body simulations of a clothed manikin offer the most anatomically accurate description of convective and radiative heat transfer, but they also impose significant computational challenges. The large number of grid points required to resolve both the complex body geometry and the fine-scale fabric layers leads to excessive memory consumption and long run times. In addition, the inconsistency in characteristic length scales between the human body and the thin fabric layers makes it difficult to maintain stable numerical performance without overly refining the mesh.

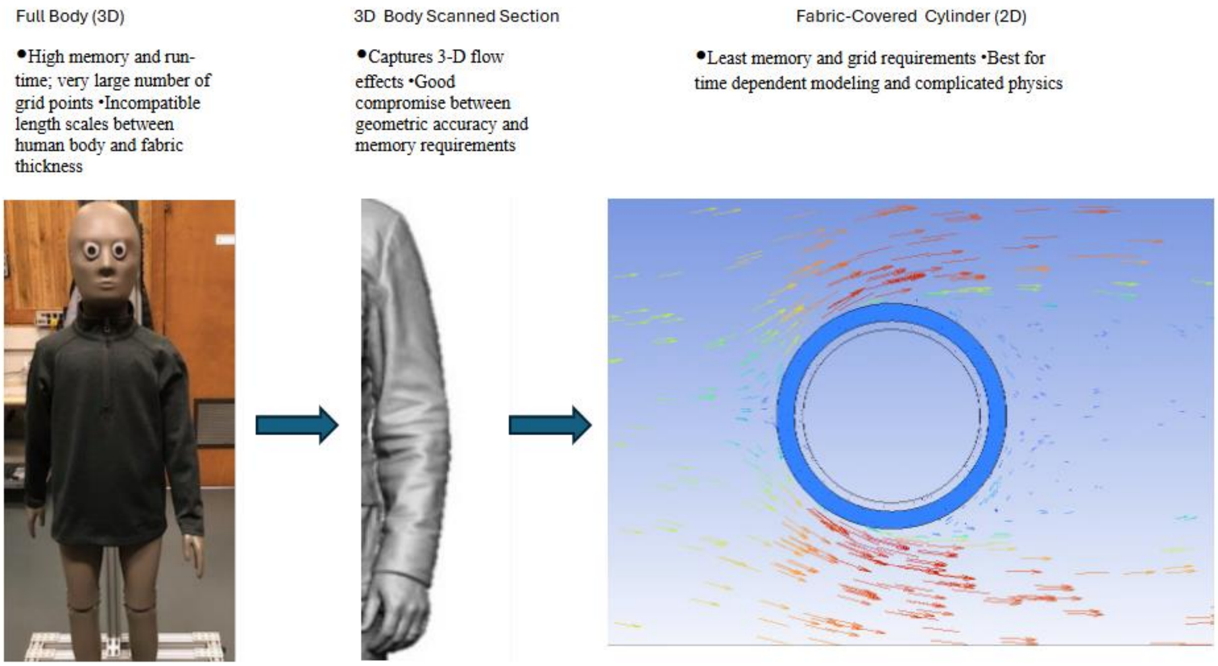

Figure 6.1 Fabric-covered cylinders can be more computationally efficient but lose the detail of specific body regions (Manikin model picture).

To overcome these challenges, an intermediate modeling approach based on 3D scanned body sections was introduced. These models preserve the essential curvature and local flow features of realistic body parts such as the torso or upper limbs while substantially reducing computational cost. They represent a good compromise between geometric fidelity and memory requirements and allow detailed analysis of local flow recirculation and heat exchange patterns.

Finally, the simplified 2D fabric-covered cylinder model, shown on the right of Figure 1, was developed to isolate and study the fundamental heat-transfer mechanisms within the skin–air–fabric system. Fabric-covered cylinders provide a well-defined experimental and computational framework for studying the system-level effects that govern heat and mass transfer through clothing layers. In particular, they enable precise control of parameters such as air spacing between fabric layers and permeability of the fabric, which is critical in determining how much heat, is transferred to or from the skin surface (Gao & McCullough, 2000; Gibson, 1997; Gibson, 2002; Havenith et al., 2006). This reduced-order model also allows time-dependent simulations of coupled thermal and flow phenomena at much lower memory and grid requirements, making it especially suitable for exploring the influence of porous media behavior and unsteady flow interactions.

6.1 3D Full-body scanning and geometry preparation for CFD simulation

Accurate geometry acquisition is a critical step in simulating heat transfer and airflow around human body, particularly when evaluating thermal interactions involving clothing systems. In this study, high-resolution 3D full-body scanning technology manufactured by Human Solutions GmbH was employed to capture the geometry of both a nude thermal manikin and the same manikin clothed in a single fabric layer. This dual-scan approach enables the precise modeling of the clothing-air-skin microclimate, a key factor in determining heat transfer behavior see Figure 6.2.

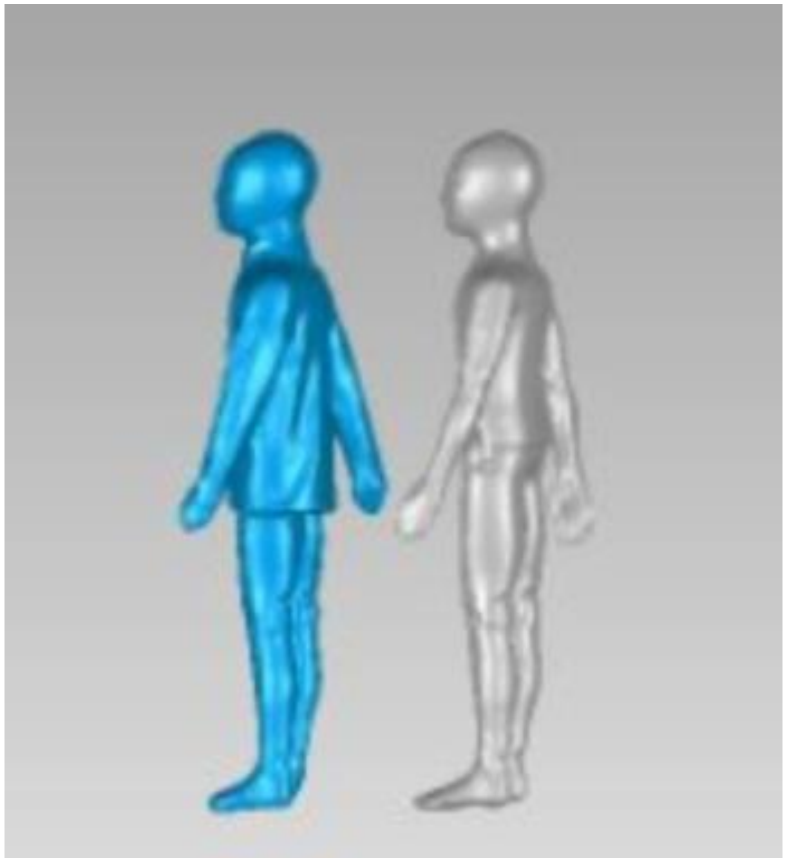

Figure 6.2 Ilustrates the 3D body scans of the nude thermal manikin (gray) and the same manikin dressed in a single-layer fabric ensemble (blue).

The scanning process was conducted using a commercial-grade 3D whole-body scanner. The 3D body scanning procedure was conducted manually by moving the handheld scanner around the stationary thermal manikin in a full 360-degree sweep. As was circled the manikin, the scanner projected structured light patterns onto its surface while simultaneously capturing the reflected images from multiple angles. Using triangulation algorithms, the system reconstructed the geometry point by point, ensuring detailed capture of all body contours, including recessed and complex areas. This hands-on scanning approach allowed for complete surface coverage and minimized obstruction, especially in areas where clothing layered over the body. The resulting high-resolution 3D mesh provided an accurate digital representation suitable for computational modeling. Separate scans were conducted for the nude manikin and the clothed version to ensure the capture of both body and garment surface details. The resulting raw scan data were exported in Standard Tessellation Language (STL) format, a widely used file type in 3D modeling that represents the object's surface geometry using triangular mesh elements.

Once acquired, the STL files were imported into Autodesk Meshmixer (Autodesk Inc., USA), a powerful mesh-editing software used for post-processing 3D models. Meshmixer enables essential operations such as noise reduction, hole filling, smoothing, and the removal of scanning artifacts. Both the nude and clothed manikin models underwent these cleaning steps independently to ensure surface and geometric continuity. Following this, the two models were aligned and merged with high precision using reference landmarks on the body, such as the torso and extremities, ensuring that the clothing layer was correctly positioned relative to the underlying skin surface.

After alignment, the merged geometry was exported again as a new STL file, now representing both the skin and fabric layers in a unified model. This composite STL was then imported into ANSYS SpaceClaim, a CAD and mesh preparation software widely used for simulation pre-processing. Within SpaceClaim, the geometry was further refined, and the mesh was generated to ensure a high-fidelity representation suitable for computational fluid dynamics (CFD) analysis. The resulting model enabled the accurate simulation of airflow and dry heat transfer through the complex clothing-air-skin system Figure 6.3 that illustrates workflow from 3D scanning to CFD results.

Recent advancements in 3D scanning technologies have significantly enhanced the ability to replicate realistic human geometries for engineering applications. The integration of high-resolution scanning with mesh editing and simulation preparation tools such as Meshmixer and SpaceClaim ensures the generation of clean and physically accurate geometries. These processes are essential for producing reliable CFD models capable of capturing thermal interactions and contributing to improved clothing system design and human thermal comfort analysis.

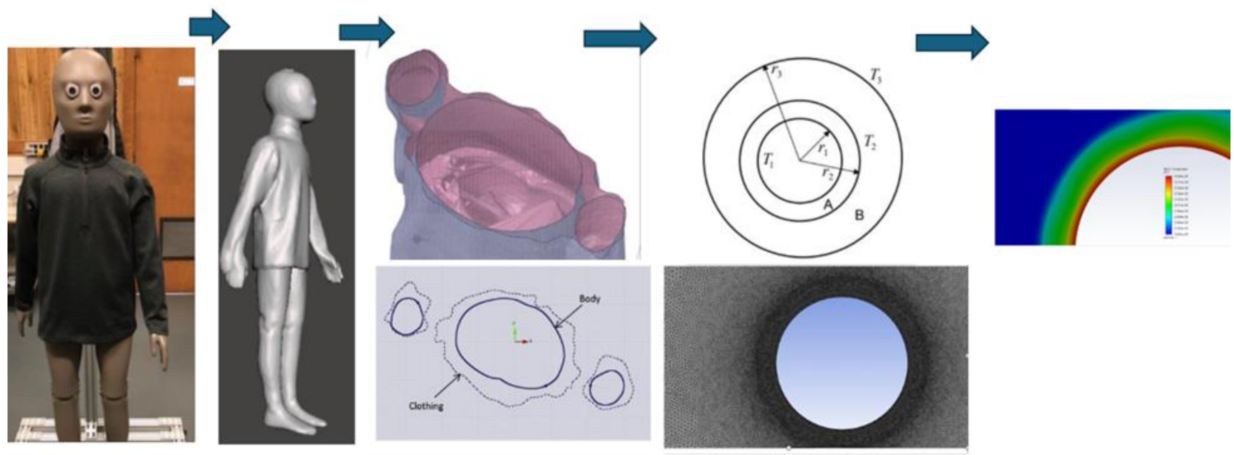

Figure 6.3 Workflow from 3D scanning to CFD results: clothed manikin, STL model, Meshmixer processing, layer segmentation, analytical diagram, meshed domain, and final temperature contour.

6.2 Modeling approaches

CFD simulations: Using specialized software (Ansys) to simulate airflow through a fabric's porous structure, allowing for detailed analysis of air velocity and temperature distribution within the clothing layer as shown in Figure 6.4. Equivalent porous medium approach: Simplifying the fabric structure as a porous medium with effective properties like permeability and thermal conductivity to analyze heat transfer.

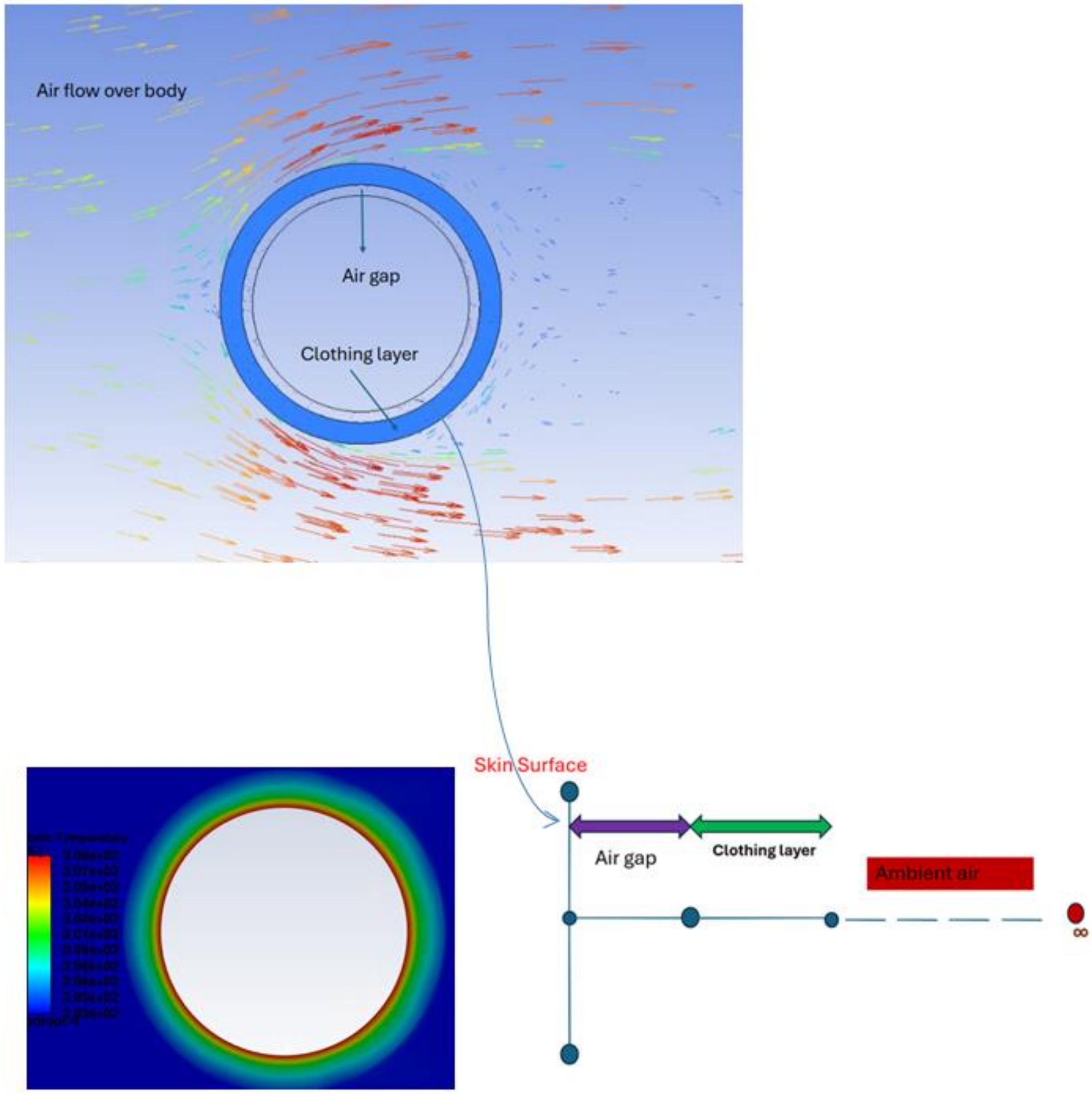

Figure 6.4 Fabric-covered cylinder: Fabric porosity 27%, air speed: 5 m/s.

A computational model enables systematic variation of individual material properties while holding other parameters constant an approach that is often challenging to achieve experimentally. In physical testing, altering one characteristic, such as thermal insulation, frequently leads to unintended changes in other dependent properties. The fabric-covered cylinder model is particularly well-suited for iterative analyses, allowing precise evaluation of how variations in a single material property influence overall thermal behavior as shown in.

6.2.1 Numerical modeling

A numerical model was developed to analyze heat transfer and fluid flow within the microclimate, specifically focusing on air circulation around the clothing. The simulation was based on the three-dimensional, steady-state forms of the continuity, momentum, and energy equations for incompressible flow. To account for the effects of turbulence, a suitable turbulence model was employed. The Reynolds-averaged governing equations used in the analysis are summarized below:

$$\frac{\partial(\rho u_i)}{\partial x_i} = 0 \tag{6.1}$$

$$\frac{\partial(\rho u_i u_j)}{\partial x_j} = -\frac{\partial p}{\partial x_i} + \frac{\partial}{\partial x_j}\left[\mu\left(\frac{\partial u_i}{\partial x_j} + \frac{\partial u_j}{\partial x_i}\right) - \rho u_i{}' u_j{}'\right] + \rho\beta(T - T^0)\delta_i{}^3 \tag{6.2}$$

$$\frac{\partial(\rho c_p u_i T)}{\partial x_i} = -\frac{\partial}{\partial x_i}\left(-\frac{k_f \partial T}{\partial x_i} + \rho c_p u_i{}' T'\right) \tag{6.3}$$

Where, u_i, p, T, and g_i represent the velocity vector, pressure, temperature, and gravitational acceleration, respectively. The terms ρ, k_f, c_p, μ,nd β denote the air density, thermal conductivity, specific heat capacity, dynamic viscosity, and volumetric thermal expansion coefficient, respectively. The Reynolds stress term, which arises from the statistical averaging of the Navier–Stokes equations, introduces additional unknowns into the system. To address this closure problem, the standard k–ε turbulence model is employed. The governing equations for the turbulent kinetic energy k and its dissipation rate ε are given as follows:

$$\partial(\rho k\, u_i)/\partial x_i = \partial/\partial x_j\, [\,(\mu + \mu_t/\sigma\_k)\ \partial k/\partial x_j\,] + \mu_t/2\ (\partial u_i/\partial x_j + \partial u_j/\partial x_i)^2 - \rho\, \varepsilon \tag{6.4}$$

$$\partial(\rho\varepsilon\, u_i)/\partial x_i = \partial/\partial x_j\, [\,(\mu + \mu_t/\sigma\_\varepsilon)\ \partial\varepsilon/\partial x_j\,] + C_1\varepsilon\ (\varepsilon\, \mu_t / k)\ (1/2)(\partial u_i/\partial x_j + \partial u_j/\partial x_i)^2 - C_2\varepsilon\, \rho\, \varepsilon^2 / k \tag{6.5}$$

Where μ_t is the turbulent viscosity, defined as:

$$\mu_t = \rho \cdot C_\mu \cdot k^2 / \varepsilon \tag{6.6}$$

The following default values for the model constants were used:

$C_\mu = 0.09$, $C_{1\varepsilon} = 1.44$, $C_{2\varepsilon} = 1.92$, $\sigma_k = 1.0$, $\sigma_\varepsilon = 1.3$

Some of the important simplifying assumptions considered in the present numerical model to make the problem manageable, heat transfer is considered to be one-dimensional in cylindrical coordinates. In developing the model, the following assumptions are made:

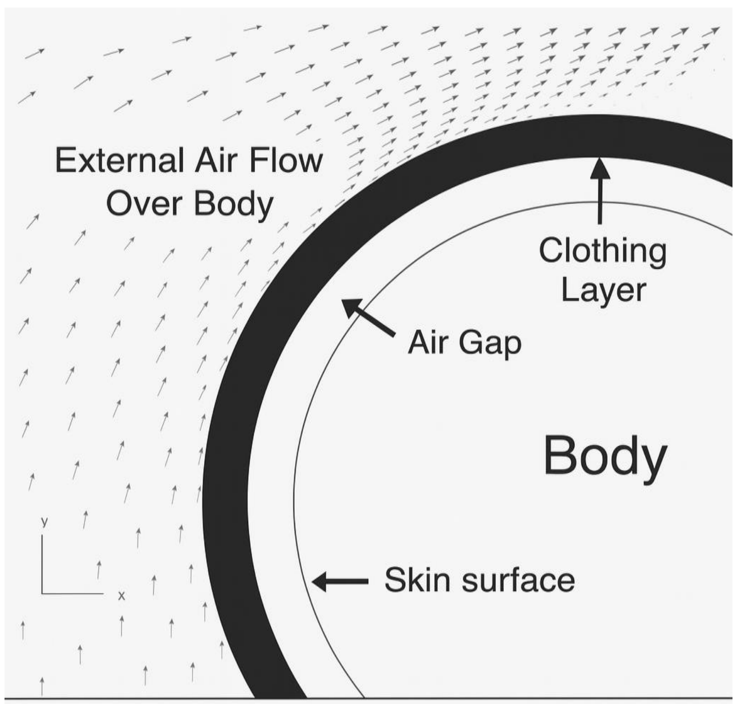

Figure 6.5 Fabric-covered cylinder model.

The configuration considered in this thesis consists of a vertical cylinder of radius r, enclosed by a porous fabric layer, as illustrated in Figure 6.5. To simplify the analysis, heat transfer is assumed to be one-dimensional in cylindrical coordinates. The development of the model is based on the following assumptions:

1. The fabric is treated as a gray body with wavelength-independent emissivity.
2. Mass transfer is neglected; the model assumes dry conditions without sweating, focusing exclusively on convective (sensible) heat transfer rather than evaporative cooling.
3. The incident heat flux on the outer surface of the fabric is assumed to be uniform across the heated region.
4. The body core temperature is maintained at a constant value of 35 °C.
5. The system is considered axisymmetric, reducing the complexity of the spatial domain.
6. Heat transfer through the fabric layer occurs in one dimension, perpendicular to its thickness.
7. Convective heat transfer within the porous fabric's entrapped air is neglected due to its complexity. Instead, local thermal equilibrium is assumed between the air and the solid fabric material in the porous medium.

The current study emphasizes conduction as the primary mechanism of heat transfer across the fabric layer. This mechanism is modeled using effective temperature-independent thermophysical properties of both the fabric material and the entrapped air within its structure. The assumption of constant properties simplifies the modeling process while maintaining physical accuracy within the studied thermal conditions.

As illustrated in Figure 6.6, the thermal exchange begins from the ambient air and chamber walls, which act as the surrounding thermal environment. These boundary conditions impose a combination of radiative and convective heat fluxes onto the external surface of the fabric. The optical characteristics of the fabric, including reflection, transmission, absorption and emission, play a critical role in determining the magnitude of these incoming fluxes. Values for these optical properties are obtained from well-documented literature sources (Su et al., 2022;

Choudhary et al., 2020; Asawo et al., 2023; Cernei et al., 2025), ensuring reliable estimates for the energy absorbed or reflected at the fabric surface.

In the 2D fabric-covered cylinder model, radiative heat transfer within the porous fabric layer is not neglected but explicitly considered as an internal heat transport mechanism. Radiation represents the internal heat energy transferred into the fabric's interior through the transmissibility of the fibrous medium. Due to the semi-transparent nature of many fabrics, part of the radiative energy emitted from the heated inner surface of the cylinder penetrates the fabric layer rather than being entirely reflected or absorbed at the surface. This transmitted radiation interacts with the fabric fibers and the entrapped air, where multiple scattering and absorption events occur. As a result, the radiative component effectively contributes to the overall heat transfer within the porous region by increasing the local energy flux toward the outer surface (Verschoor and Greebler, 1952; Torvi and Dale, 1999; Talukdar et al., 2016).

In the computational framework, this behavior is modeled by coupling the radiative transfer equation (RTE) with the porous energy equation, treating the fabric as a semi-transparent medium with finite transmissivity and absorptivity. The internal radiation is, therefore, represented as an additional volumetric heat source term that enhances conductive and convective heat transfer inside the fabric matrix. This approach captures the physical reality that radiation can traverse partially through the porous textile structure, influencing the overall thermal resistance and temperature distribution. Incorporating this mechanism ensures that the model more accurately reflects real fabric performance under thermal exposure, especially when dealing with fabrics subjected to elevated surface temperatures or low-density weaves where radiative penetration becomes significant.

Upon interaction with the fabric's external layer, a portion of the incoming radiation is reflected to the ambient environment, while the remainder is absorbed and conducted through the fabric thickness. Conduction heat transfer dominates this region and is shown at the fabric's bottom boundary in the schematic. The fabric inner surface then serves as a thermal boundary to the adjacent air gap (microclimate), which is treated as a participating medium a thermally active domain that allows all three modes of heat transfer: radiation, convection, and conduction.

In this microclimate zone, radiative exchange occurs between the inner fabric surface and the skin surface, accounting for emissive properties of both. Simultaneously, natural or forced convection within the air gap influences heat transfer depending on local temperature gradients and air velocity, while conduction through stagnant air continues to transfer thermal energy directly toward the skin.

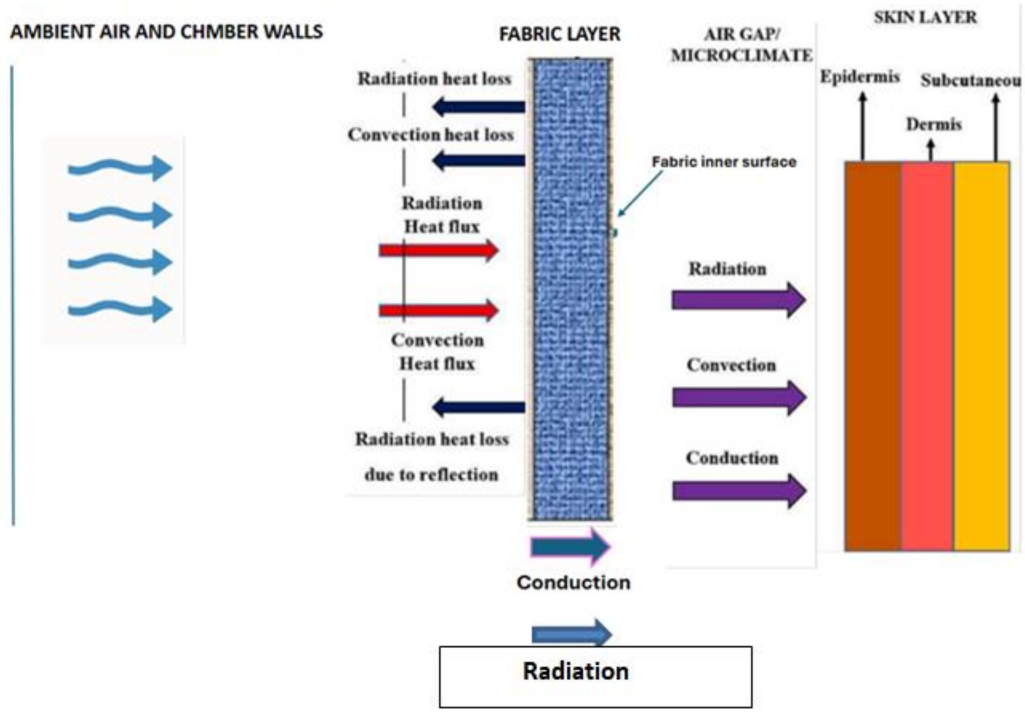

Figure 6.6 Schematic representation of the fabric-air gap microclimate-skin arrangement.

The air gap or microclimate, situated between the skin surface and the inner surface of the fabric plays a critical role in determining the overall thermal performance of the clothing system. This layer serves as a transitional zone through which heat is transferred via both conduction and convection, depending on the thickness of the air space and the thermal conditions present.

A well-established principle in thermal insulation is that stagnant air can act as an effective insulator due to its low thermal conductivity. When the air within the gap remains motionless, conduction dominates the mode of heat transfer. In such a scenario, the air gap contributes significantly to reducing heat flow from the outer fabric toward the skin, thereby enhancing thermal protection. Furthermore, it is known that the thermal resistance of a stagnant air layer tends to increase with the thickness of the air space up to a critical point.

However, as the thickness of the air gap increases beyond a certain point, the potential for natural convection arises. When the air becomes sufficiently buoyant due to temperature gradients, it begins to circulate, forming convective cells that enhance thermal transport. This onset of convection reduces the insulating capability of the air layer, leading to increased heat transfer toward the skin surface. As a result, the protective performance of the air gap may decline, especially under conditions of high external heat flux.

Along with conduction and convection, thermal radiation in the air gap can significantly contribute to the overall heat transfer process, especially since the inner surface of the fabric usually has higher temperatures than the outer surface. In this model, the radiative heat transfer between the two primary surfaces the inner fabric surface and the opposing skin surface simplifies the problem while accurately representing the radiative heat exchange. In the present study, radiation and convection are treated as independent (uncoupled) phenomena, enabling their separate quantification and subsequent summation to obtain the total thermal flux across the air gap. This integrated approach provides a more complete representation of the thermal microclimate behavior, ensuring that both surface emissivity effects and buoyancy-driven convective currents are appropriately accounted for in predicting the skin thermal response under varying environmental and fabric.

6.2.2 Thermal models for porous media

In heat transfer analysis involving porous materials such as fabrics, two principal thermal modeling approaches are typically used: the thermal equilibrium model and the non-equilibrium model. The distinction between these approaches lies in how they represent the temperature relationship between the solid matrix and the fluid within the porous medium (ANSYS Fluent Theory Guide, 2020 R2).

The thermal equilibrium model assumes that the solid matrix and the fluid phase are at the same temperature at all points within the porous structure (Cengel & Ghajar, 2015). This simplification implies instantaneous thermal exchange between the two phases, eliminating the need to solve separate energy equations for the solid and fluid components. Such an assumption is valid when the characteristic time of heat transfer between the solid and the fluid is much smaller than the overall timescale of the process, or when the conductivity and heat capacity of both phases are comparable. In the present thesis, this equilibrium model is adopted, as it provides an efficient and physically consistent representation of the fabric's thermal response under steady-state conditions, particularly where temperature gradients between the solid and air phases are minimal.

Conversely, the non-equilibrium model allows for different temperatures between the solid and fluid phases. In this case, two separate energy equations are solved one for the solid matrix and another for the fluid. Coupling between these equations occurs through an interfacial heat transfer term that depends on the interfacial area density (the surface area of solid-fluid contact per unit volume) and the heat transfer coefficient between the phases. These parameters must be determined experimentally through specialized laboratory measurements, as they depend on the fabric's microstructure, porosity, and fiber distribution. The non-equilibrium model provides higher fidelity for cases involving rapid transients or materials with large thermal property differences, but it significantly increases computational cost and data requirements.

Porosity (ε) is another critical property of porous media and is defined as the ratio of void (air) volume to the total volume of the material. It governs both thermal and momentum transfer by affecting conduction through solid and fluid phases and by determining the effective flow permeability of the medium.

Under the thermal equilibrium assumption used in this study, the one-dimensional steady-state radial heat transfer equation for a homogeneous, isotropic porous medium is expressed as (Cengel & Ghajar, 2015):

$$\frac{1}{r}\frac{d}{dr}\left(r k_{eff}\frac{dT}{dr}\right) + q''_{rad} = 0 \tag{6.7}$$

Where r is the radial coordinate, k_{eff} is the effective thermal conductivity of the porous material (accounting for both solid and fluid conduction and radiative transfer), T is the temperature, and q''_{rad} represents the volumetric radiative heat flux transmitted through the porous fabric layer due to its finite transmissivity.

This equation forms the foundation of the numerical modeling in this thesis, describing how heat via conduction, radiation, and convection within the pores is distributed across the fabric-covered cylinder. By incorporating the equilibrium assumption and the radiative term, the model accurately represents steady-state thermal behavior within the porous fabric system while maintaining computational efficiency.

The governing one-dimensional steady-state radial heat transfer equation for the porous fabric layer can be described in greater detail by incorporating both conductive and radiative components within the porous medium. Following the formulation by Torvi and Dale

(1994), the general form of the energy balance for heat transfer through a fabric layer exposed to thermal radiation can be expressed as:

$$\frac{\partial}{\partial r}\left(k_{fab}\left(\frac{\partial T}{\partial r}\right)\right)+\left(\frac{k_{fab}}{r}\frac{\partial T}{\partial r}\right)-\ \gamma_{fab}q_{rad}\exp\left(\gamma_{fab}(r-r_{of})\right)=0 \tag{6.8}$$

Where T is fabric temperature and k_{fab} is the temperature-independent thermal conductivity, respectively. q_{rad} is the portion of the directly transmitted incident heat flux on the surface of the element due to thermal radiation from the surrounding (chamber walls) and γ_{fab} is the extinction coefficient for the fabric. Hence, the term $\gamma_{fab}q_{rad}\exp\left(\gamma_{fab}(r-r_{of})\right)$ represents the internal heat by the radiation transferred to the internal region of the fabric by the transmissibility of the fabric τ_{fab}. γ_{fab} is evaluated as:

$$\gamma_{fab}=\frac{\ln\tau_{fab}}{L_{fab}} \tag{6.9}$$

Where $L_{fab}$is the thickness of the fabric.

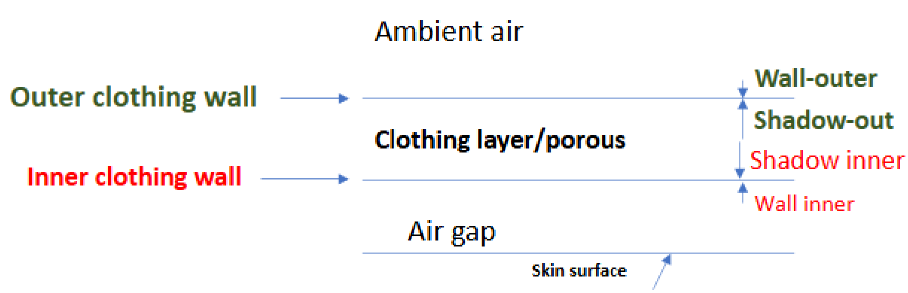

Figure 6.7 Schematic representation of fabric layer boundaries.

As illustrated in Figure 6.7, the fabric layer in the model is defined by two key thermal boundaries, one exposed to the ambient environment and the other in direct contact with the skin surface. The outer boundary interacts with the external air or surrounding thermal conditions, where convective and radiative exchanges primarily occur between the fabric's exterior and the environment. This interface governs how external heat or cold exposure is transmitted through the fabric structure. In contrast, the inner boundary represents the interface between the fabric and the skin (or underlying surface), where the heat flux is influenced by both conduction through the fabric and radiation transmitted into the microclimate layer. Modeling these two boundaries is crucial for accurately simulating the coupled heat transfer processes in clothing systems. The outer surface determines the rate at which environmental heat penetrates the fabric, while the inner surface determines how this energy is transferred to the skin, ultimately affecting thermal comfort and skin temperature. Together, these boundaries define the thermal resistance and energy balance across the fabric layer, forming the basis for calculating the net heat flux, and temperature gradients in the CFD model.

6.2.3 Thermal resistance network across skin-air gap-clothing layers

Figure 6.8 illustrates the complex network of heat transfer mechanisms occurring through the multilayer system comprising the skin surface, the air gap (or microclimate), the fabric layer, and the surrounding ambient air. This system is modeled as a thermal resistance network, representing how energy moves through the concentric layers by means of conduction, convection, and radiation. Each layer contributes a distinct resistance to heat flow, depending on its physical and thermal properties such as thickness, thermal conductivity, and emissivity.

Starting at the skin interface, heat is primarily generated by metabolic processes and conducted through the skin surface into the adjacent air gap. Within this microclimate region, heat transfer occurs by both radiation and natural convection due to buoyancy-driven motion caused by temperature gradients. The air gap thickness plays a crucial role when small, conduction dominates (conduction through stagnant air); when larger, convective currents enhance overall heat transport. Simultaneously, radiative exchange occurs between the warmer skin and the inner surface of the fabric, contributing to the total heat flux across this zone. The radiative component is especially significant because the skin and fabric surfaces often exhibit different emissivities, allowing for a measurable portion of heat to be transmitted even without direct contact.

The fabric layer itself behaves as a porous medium, allowing for both conductive heat transfer through the solid fibers and convective flow through interconnected air channels. Additionally, radiative transmission within the porous structure governed by the fabric's transmissivity and extinction coefficient permits partial penetration of thermal radiation into the fabric's interior. This combined conduction–radiation effect defines the fabric's effective thermal conductivity. At the outer fabric surface, convective and radiative exchanges with the ambient air complete the thermal network. The ambient side experiences forced convection driven by external air movement, while the radiative heat loss occurs toward the surrounding environment or chamber walls.

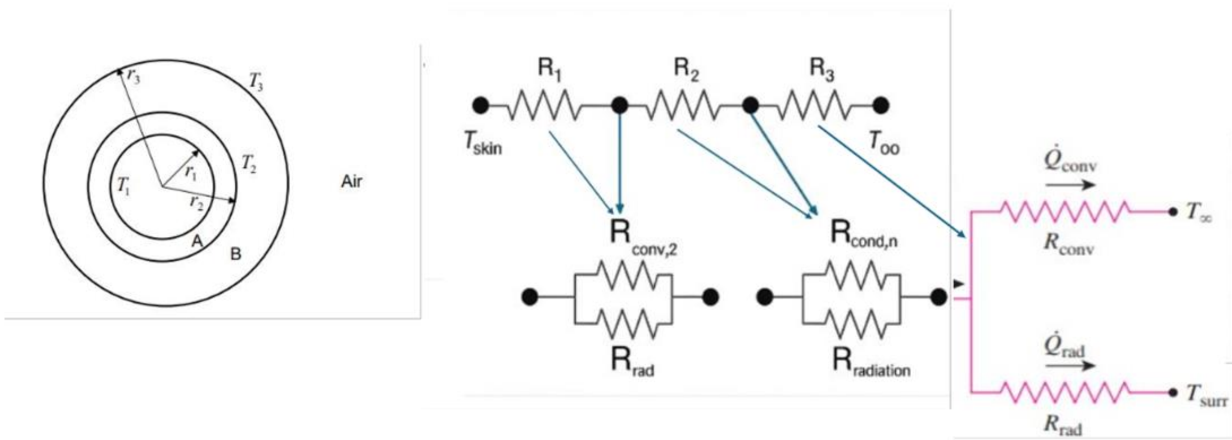

Figure 6.8 The overall network of thermal resistances for heat transfer across the fabric-air gap microclimate-skin arrangement.

Where:

A: Air gap layer

B: Clothing layer

T_1: Skin surface temperature

T_2: Inner clothing wall temperature

T_3: Outer clothing wall temperature

$T\infty$: Ambient air temperature

By quantifying each thermal resistance skin-to-air gap ($R_{\text{skin-air}}$), air gap (R_{gap}), fabric layer (R_{fab}), and fabric-to-ambient ($R_{\text{fab-amb}}$) the model effectively captures the overall rate of heat transfer across the clothing–microclimate–skin system. The total thermal resistance represents the cumulative opposition to heat flow and is obtained by summing all individual resistances, thereby enabling the calculation of an equivalent heat transfer coefficient. This approach provides valuable insights into how material properties, clothing fit, air gap thickness, and external airflow conditions influence human thermal comfort and heat dissipation. In the thermal resistance network, R_1 corresponds to the equivalent thermal resistance (including convection and radiation) within the air gap between the skin and clothing, R_2 represents the combined conduction and radiation resistance through the clothing layer, and R_3 denotes the outer ambient air layer resistance encompassing both convective and radiative effects. This networked representation aligns closely with the steady-state one-dimensional heat transfer model discussed earlier in this thesis, establishing a unified framework that facilitates the comparison of CFD predictions with analytical formulations and experimental data under controlled environmental conditions.

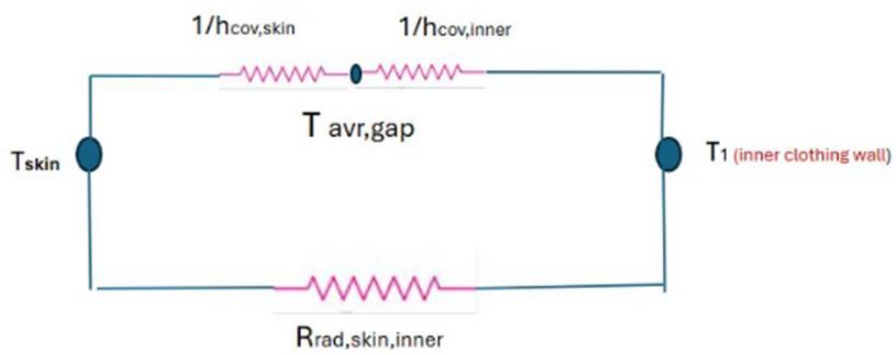

Figure 6.9 Thermal resistances in the air gap microclimate.

The thermal resistance network shown in the schematic (Figure 6.9) represents the heat transfer mechanisms occurring across the air gap microclimate between the skin surface (T_{skin}) and the inner surface of the clothing wall (T_1). This air gap layer plays a crucial role in regulating heat flow between the human body and the fabric, and the diagram breaks it into parallel modes of heat transfer: convection and radiation.

The first pathway consists of two convective resistances acting in series across the air gap. The initial thermal resistance arises from natural convective heat transfer between the skin surface and the adjacent air layer. It is governed by the convective heat transfer coefficient at the skin interface$\left(h_{cov,skin}\right)$. This value depends on factors such as air gap thickness, body posture, and surface temperature difference. The second resistance corresponds to convective heat transfer from the air layer to the fabric's inner surface, governed by $\left(h_{cov,inner}\right)$.

The second pathway represents thermal radiation exchange between the skin surface and the inner fabric surface. Since radiation is a line-of-sight transfer mechanism, this resistance encompasses surface emissivities of the skin and the fabric, the temperature difference between them, the geometrical configuration (such as view factor), and the Stefan-Boltzmann law. Radiation occurs in parallel to convection and becomes increasingly significant when temperatures are high, such as during exposure to hot ambient conditions.

The overall equivalent thermal resistance of the air gap is derived from the parallel combination of the series convective path $(\frac{1}{\mathrm{h_{cov,skin}}). + \frac{1}{\mathrm{h_{cov,inner}}})$ and the radiative resistance $(R_{rad,skin,inner})$. mathematically, this is expressed as:

$$\frac{1}{\mathrm{R_{1,gap}}} = \frac{1}{(\frac{1}{\mathrm{h_{cov,skin}}}). + \frac{1}{\mathrm{h_{cov,inner}}})} + \frac{1}{\mathrm{R_{rad,skin,inner}}} \tag{6.10}$$

The average temperature of the air gap $(T_{avr,gap})$ is shown at the midpoint of the convection path, which is used in some formulations for calculating effective radiative and convective properties. This schematic captures how both convective and radiative heat transfer mechanisms work (in parallel) to govern the total energy flux across the air gap microclimate.

The equations shown below describe the radiative heat transfer and thermal resistance between the skin surface and the inner clothing wall through the microclimate air gap.

The first equation represents the radiative thermal resistance between the skin surface and the inner clothing surface. This resistance is denoted as:

$$R_{\mathrm{rad,skin-inner\ wall}} = \frac{1}{2\pi\ \mathrm{r_1}\ \mathrm{L}\ h_{\mathrm{rad\ skin-inner\ clothing\ wall(gap)}}} \tag{6.11}$$

It is inversely proportional to the product of the surface area (represented by $2\pi r_1 L$) and the effective radiative heat transfer coefficient h_{rad} skin–inner clothing wall (gap). The area assumes cylindrical geometry, where r_1 is the radius of the skin surface, and L is the vertical length of the section under analysis.

The equation that calculates the radiative heat flux q_{rad}, skin–inner between the skin and the inner wall using the Stefan-Boltzmann law for radiation is:

$$q_{\text{rad,skin-inner}} = \frac{2\pi r_1 \, L \, \sigma \, (T^4{}_{\text{skin}} - T^4{}_{\text{inner-wall}})}{\frac{1}{\varepsilon_{skin}} + \frac{1-\varepsilon_{inner-wall}}{\varepsilon_{inner-wall}}\left(\frac{r_1}{r_2}\right)} \tag{6.12}$$

The denominator incorporates surface emissivities ε_{skin} and $\varepsilon_{inner-wall}l$, which govern the radiative properties of the skin and clothing, respectively. The emissivity of both the inner and outer fabric surfaces was assumed to be ε = 0.9 and skin emissivity of 0.98 was used for all simulations. It also includes a geometrical correction factor (r_1/r_2), representing the curvature effect between the concentric layers.

The next equation defines the effective radiative heat transfer coefficient h_{rad}, which linearizes the radiation heat flux over the temperature difference:

$$h_{\text{rad skin-inner clothing wall(gap)}} = \frac{\sigma \, (T^2{}_{\text{skin}} + T^2{}_{\text{inner-wall}})(T_{\text{skin}} + T_{\text{inner-wall}})}{\frac{1}{\varepsilon_{skin}} + \frac{1-\varepsilon_{inner-wall}}{\varepsilon_{inner-wall}}\left(\frac{r_1}{r_2}\right)} \tag{6.13}$$

Finally, the geometry simplifies such that the skin and inner wall radii are approximately equal ($r_1/r_2 \approx 1$), the expression simplifies to:

$$h_{\text{rad skin-inner clothing wall(gap)}} = \frac{\sigma \, (T^2{}_{\text{skin}} + T^2{}_{\text{inner-wall}})(T_{\text{skin}} + T_{\text{inner-wall}})}{\frac{1}{\varepsilon_{skin}} + \frac{1}{\varepsilon_{inner-wall}} - 1} \tag{6.14}$$

Denote by R_2 the equivalent thermal resistance of the fabric layer, accounting for both conduction and radiation heat transfer. The fabric serves as a cylindrical layer through which heat travels from the inner surface to the outer surface. This resistance is modeled as the sum of conductive and radiative resistances in parallel, reflecting the dual nature of heat transport across textile materials exposed to thermal gradients. The total resistance R_2 is given by:

$$R_2 = \left[\frac{1}{\frac{ln\left(\frac{r_3}{r_2}\right)}{2\pi * k_{\text{fabric}} * L}} + \frac{1}{\frac{1}{h_{(\text{rad})\_\text{fabric}} * 2\pi * r_2 * L}} \right]^{-1} \tag{6.15}$$

Denote by R_3 the thermal resistance due to the combined effects of convection and radiation from the outer surface of the clothing to the ambient environment. This resistance plays a critical role in determining the total heat loss from the clothed body to the surrounding air. The expression below provides a combined form of this resistance, accounting for the convective and radiative heat transfer coefficients. These coefficients, $h_{\text{conv,out-fab-wall}}$ and $h_{\text{rad,out-fab-wall}}$, are evaluated at the outer fabric surface and represent the effectiveness of heat transfer due to air movement and electromagnetic radiation, respectively. The equivalent thermal resistance R_3 can be expressed as:

$$R_3 = \left[\frac{1}{\frac{1}{h_{(\text{conv})\text{out\_fabric\_wall}} * 2\pi * r3 * L}} + \frac{1}{\frac{1}{h_{(\text{rad})\text{out\_fabric\_wall}} * 2\pi * r3 * L}} \right]^{-1} \tag{6.16}$$

Sensible heat exchange from the skin surface must pass through air gap then clothing to the surrounding environment. These paths are treated in series as described in detail earlier. The transport of sensible heat through clothing involves a combination of conduction, convection, and radiation mechanisms. In practical thermal analysis, it is often convenient to consolidate these heat transfer processes into a single effective thermal resistance term. This term is known as the clothing thermal resistance R_{cl}, which represents the combined resistance offered by the clothing layer against the passage of heat from the skin to the environment. The basic relationship is:

$$q_1 = \frac{(T_{skin} - T_{cloth-outer-wall})}{\mathrm{R_{cl}}} \tag{6.17}$$

Where, T_{skin} is the skin surface and $T_{cloth-outer-wall}$ is the mean temperature at the outer surface of the clothing. R_{cl} is the overall clothing thermal resistance expressed in units of

$m^2 \cdot K/W. R_{cl} = R_1 + R_2$

$$q_1 = (C + R)_{outer-fab-wall} \tag{6.18}$$

C and R represent the convective and radiative heat losses from the clothing outer wall respectively.

6.3 Benchmark simulations – bare cylinder

The bare cylinder simulation serves as a critical validation step, offering a means to directly compare computational results with both experimental measurements and well-established theoretical models for heat and mass transfer around a cylinder subjected to crossflow conditions. This baseline configuration eliminates the complexities introduced by fabric layers, thereby isolating fundamental flow and thermal phenomena.

The computational domain for the benchmark simulations consists of a two-dimensional cross-section of a bare cylinder with a diameter of 100 mm, positioned at the center of a surrounding fluid region inside an enclosure (environmental chamber). This simplified geometric representation is used to study heat transfer behavior around a cylindrical body subjected to crossflow conditions. The model assumes axisymmetric conditions and treats the problem in 2D to reduce computational cost while preserving the essential physics.

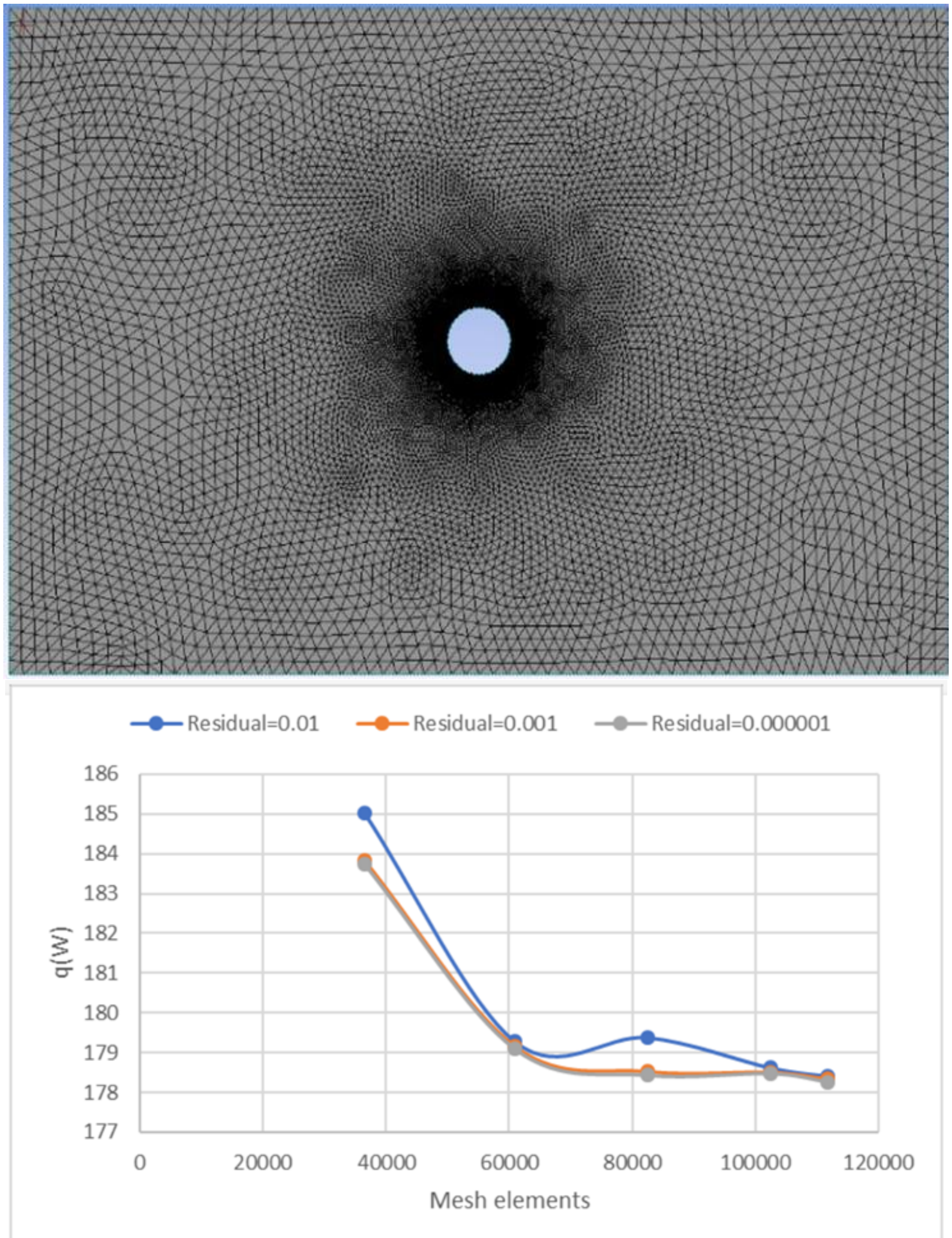

Figure 6.10 Mesh and grid independence test/2D bare cylinder model.

To discretize the domain, an unstructured mesh composed of triangular elements was generated, with 41,950 nodes and 82,480 elements. The mesh is refined near the cylinder surface to accurately capture boundary layer effects and steep thermal gradients, ensuring accuracy in the predicted flow and temperature fields. A grid independence test was performed to validate the adequacy of the mesh resolution as shown in Figure 6.10. This involved comparing key output parameters such as total heat transfer across multiple mesh refinements. The results confirmed that further refinement had negligible impact on the solution, thus validating the chosen mesh for subsequent simulations. This balance between accuracy and computational efficiency makes the mesh suitable for both verification studies and more advanced fabric-covered configurations/models.

6.3.1 Thermal resistance calculation and validation – bare cylinder

To simulate both convective and radiative heat transfer around a bare cylinder using ANSYS Fluent, specific boundary conditions are defined to accurately model the physical environment. The cylinder surface is maintained at a constant temperature of 35°C, with no-slip velocity conditions (u = v = 0) to represent a stationary heated body. The inlet is modeled with a uniform air temperature of 5°C and a variable inlet velocity ranging from 0.05 to 1 m/s in the horizontal direction (u), while the vertical component (v) is set to zero. The enclosure walls surrounding the simulation domain are treated as adiabatic, meaning no heat transfer occurs through these boundaries. Finally, the outlet boundary condition is set to gauge pressure of 0 Pa to simulate an open flow exit as shown in Table 6.1. These conditions are essential for ensuring accurate and realistic simulation results.

Table 6.1 Boundary conditions for the cylinder simulation setup.

Boundary name	Boundary conditions
Cylinder surface	T_{skin}= 35°C, T_{air}= 5°C
Inlet-velocity	u = 0.05 - 1 m/s, v = 0
Enclosure walls	Adiabatic
Outlet pressure	Gauge pressure = 0 Pa

The thermal resistance $\left(R_{cylinder}\right)$ of the bare cylinder is calculated using the following expression:

$$R_{cylinder} = \frac{A(T_{cylinder} - T_{\infty})}{E} = \frac{\Delta T}{q''_{total}} \tag{6.19}$$

Where:

- ΔT = 30 K (Temperature difference between cylinder surface and surrounding air)
- q''_{total} = 392.479 W/m² (Total heat flux from the cylinder: Both convection and radiation) obtained from CFD simulation.

Substituting the values into the formula:

$$R_{cylinder} = \frac{30}{392.479} = 0.0764 \text{ m}^2\cdot\text{K/W} \tag{6.20}$$

Table 6.2 Steady-state average thermal resistance values for each zone of the nude thermal manikin (Stan).

Zone No.	Body Region	Average surface temperature (°C)	Heat flux (W/m^2)	Thermal Resistance, R, ($m^2 \cdot K/W$)
1	Head	35.997	155.906	0.094
2	Upper Arm (Left)	34.998	205.799	0.072
3	Upper Arm (Right)	34.998	186.228	0.079
4	Forearm (Left)	34.998	230.673	0.064
5	Forearm (Right)	35.005	206.284	0.071
6	Hand (Left)	35.00	232.713	0.063
7	Hand (Right)	34.998	220.316	0.067

Table 6.2 display the steady-state thermal resistance data for each of the 7 independently controlled zones of the nude thermal manikin, Stan. The highlighted row indicates the mean resistance value across the body, summarizing overall heat transfer efficiency under nude conditions. These tests were conducted under controlled environmental conditions within the Institute for Environmental Research chamber at Kansas State University, with ambient air velocity at 0.35 m/s. The resulting data provide a key validation benchmark for the CFD model, ensuring that predicted total (both convective and radiative) heat transfer fluxes accurately represent experimentally measured values across different body regions.

This calculated result is in excellent agreement with experimental values obtained from the nude manikin test conducted at the IER, specifically, the thermal resistance for the forearm zone in the simulation, which accounts for radiation and buoyancy effects, is approximately 0.076. This close match confirms the validity of the computational model and supports the assumption that the simulation framework accurately captures the heat transfer characteristics of a bare cylindrical geometry under crossflow air conditions.

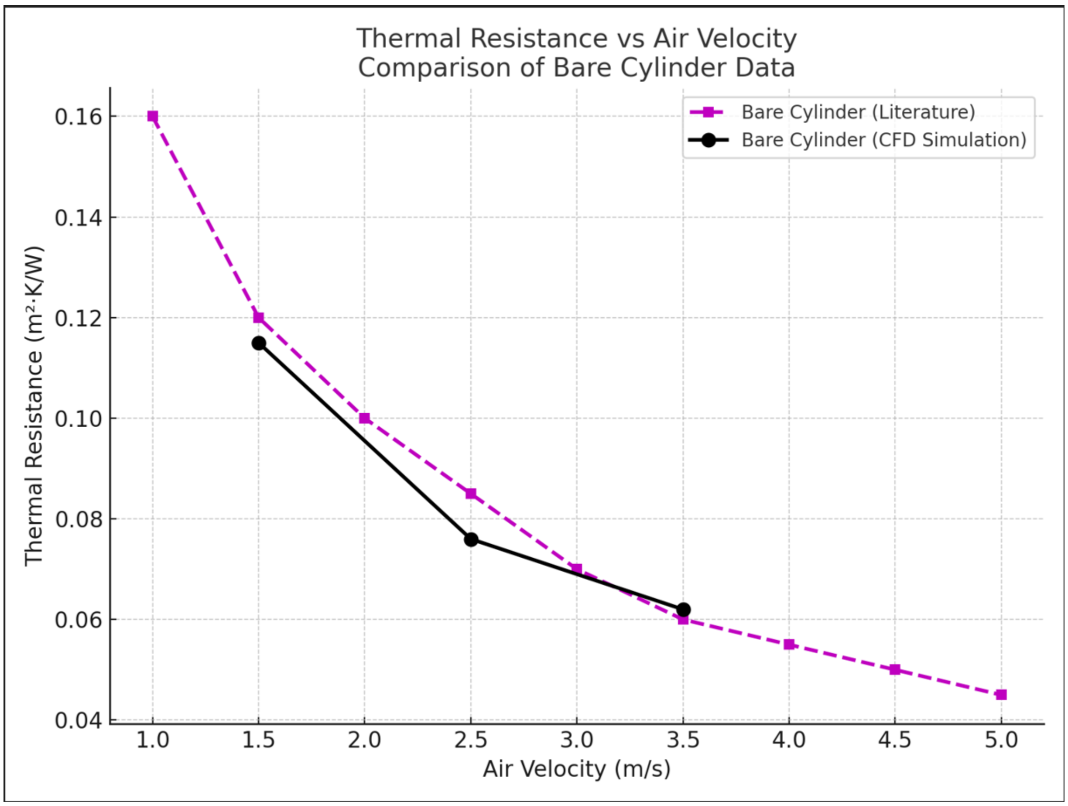

Figure 6.11 Thermal resistance vs air velocity comparison of bare cylinder data extracted from Churchill and Bernstein (1977) (magenta dashed line) with your CFD simulation data (black solid line).

In order to establish a meaningful comparison with classical heat transfer literature, the radiation model was temporarily deactivated in the CFD simulation, thereby isolating the convective component of total heat transfer from the cylindrical surface. This approach ensured that the results would correspond directly to those predicted by well-established empirical correlations for external forced convection. Specifically, the simulation results were compared against the Churchill and Bernstein (1977) correlation, which provides a generalized Nusselt number relationship for forced convection from a smooth, isothermal cylinder in crossflow. This correlation is widely recognized as a benchmark reference for assessing convective performance in mixed or forced flow conditions, and is particularly valuable for its broad Reynolds and Prandtl number applicability.

As shown in Figure 6.11, when radiation was excluded, the total thermal resistance derived from the CFD model exhibited a strong alignment with literature-based estimates, including those derived from the Churchill–Bernstein correlation. The predicted Nusselt numbers fell within the expected ±20% range reported by Bergman and Lavine (2017) for experimental and theoretical comparisons, indicating excellent consistency between the numerical and analytical methods. This level of agreement validates the CFD framework's ability to replicate standard forced convection behavior over a simple cylindrical geometry, which serves as the foundational model for the human body model. Consequently, this benchmarking step confirms that the turbulence modeling strategy, near-wall treatment, and mesh refinement adopted in this study are appropriately tuned to capture realistic flow and heat transfer behavior even before accounting for radiative or porous layer effects in subsequent models.

CFD Simulation Parameters:

- Air velocity, $V = 6$ m/s
- Surface heat transfer rate, $q = 406.899$ W
- Temperature difference, $\Delta T = 30$ K

- Cylinder surface area, A = π × D × L = π × 0.1 m × 1 m

Heat Transfer Coefficient Calculation:

$$h = \frac{q}{(A \times \Delta T)} = \frac{406.899}{(\pi \times 0.1 \times 1 \times 30)} = 39.8 \text{ W/m}^2\cdot\text{K} \tag{6.21}$$

Calculated Reynolds Number: Re = 40608

Nusselt Number from CFD:

$$Nu_{CFD} = \frac{h \times D}{k} = \frac{(39.8 \times 0.1)}{0.02568} = 154.8568 \tag{6.22}$$

Nusselt Number from Churchill and Bernstein (1977):

$$Nu_{CB} = 0.3 + \frac{0.62 \times Re^{1/2} \times Pr^{1/3}\}}{[1 + (0.4\ /\ Pr^{2/3}]^{1/4}} \left[1 + \left(\frac{Re}{282000}\right)^{1/2}\right] = 135.80 \tag{6.23}$$

Percentage error calculation:

$$\%\text{Error} = \frac{|Nu_{CFD} - Nu_{CB}|}{Nu_{CB}}| \times 100 = \frac{|154.8568 - 135.80|}{135.80} \times 100 = 14.617\% \tag{6.24}$$

The CFD-predicted Nusselt number is 154.86, while the empirical correlation predicts a value of 135.80. The resulting deviation of approximately 14.6% falls within the accepted range of 20% as noted by Bergman and Lavine (2017). This agreement validates the accuracy of the simulation framework and confirms its reliability for further investigations of heat transfer behavior around bare cylinders. Consequently, this validation gives confidence to the use of the same modeling approach for more complex scenarios, such as those involving fabric-covered cylinders. The consistency between simulated and documented results suggests that subsequent predictions—though applied to more complex configurations—are built upon a sound and verified computational foundation.

6.4 2D Fabric-covered cylinder model and mesh description

The computational model shown in Figure 6.12 represents a 2D axisymmetric cross-section of a fabric-covered cylinder used to study heat transfer phenomena in Ansys Fluent. The inner cylinder, which mimics the human skin surface, has a diameter of 100 mm. Surrounding this core is a 3 mm thick concentric air gap, enveloping the air gap is a 6.5 mm thick fabric. This layered setup is designed to accurately represent the complex interaction between skin, air insulation, and clothing during thermal analysis. Chen et al. (2004) investigated clothing thermal performance by dressing up a manikin in various fits. Both studies reported the existence of a critical microclimate thickness. When the microclimate thickness was less than the critical value of 10 mm, the heat resistance increased with increasing microclimate thickness. This critical thickness was attributed to the onset of natural convection in the microclimate.

The mesh used for this model is highly refined to capture detailed flow and thermal characteristics within each layer. A total of 6,196,19 nodes and 1,235,732 elements are employed, ensuring accurate resolution of gradients in temperature and velocity, especially across the air gap and fabric layer interfaces. The mesh appears to be structured and well-distributed, offering a good balance between computational cost and simulation fidelity.

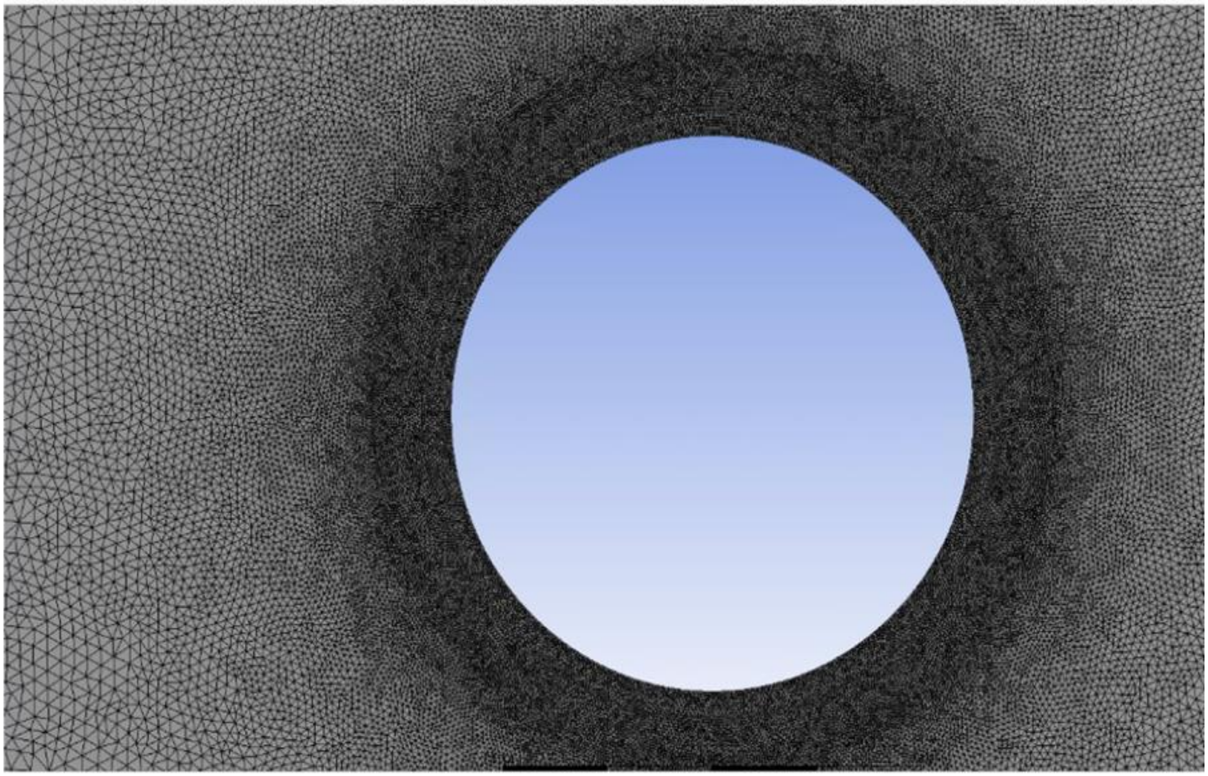

Figure 6.12 Geometry and mesh of the 2D fabric-covered cylinder model.

A grid independence test was conducted for the fabric-covered cylinder model by evaluating the total heat loss across different mesh densities (see Figure. 6.13). The results indicate convergence at approximately 600,000 elements, confirming that further mesh refinement has negligible impact on simulation accuracy.

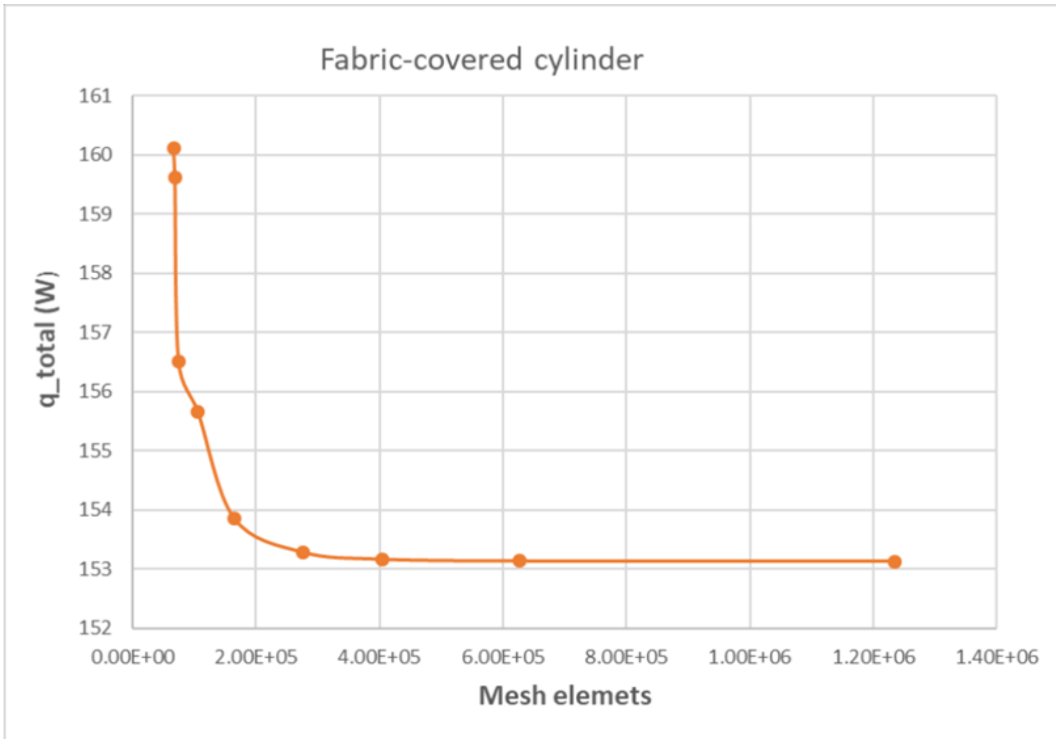

Figure 6.13 Mesh and grid independence test/2D fabric covered cylinder model.

The heat transfer through porous textiles is very complex due to coupled heat conduction and radiation interactions caused by air entrapped within the pores of the fabric. The modeling approach must therefore account for radiative transfer mechanisms in addition to standard conduction. In this study, a two-flux radiation model is used to simulate the radiation heat transport in porous fabric layers, including absorption, scattering, and self-emission.

From existing literature (Modest & Mazumder, 2022), it is observed that most prior studies on porous textiles have concentrated on modeling radiation heat transfer by incorporating absorption, transmission, and emission to surrounding walls or the skin. However, few studies have implemented the more comprehensive two-flux model that accounts for reflection and self-emission within the fabric's porous structure. This inclusion allows for a more accurate representation of the thermal behavior of textile materials exposed to thermal radiation.

In ANSYS Fluent, the fabric layer covering the cylinder is modeled as a porous zone to realistically capture the resistance encountered by air flow through the textile. The porous zone that participates in radiative heat transfer is modeled using a set of thermal and physical parameters within ANSYS Fluent's porous media framework. One of the key parameters is the viscous resistance coefficient (with units of m^{-2}), which quantifies the resistance to fluid flow arising from viscous effects within the porous structure. In addition, inertial resistance is defined to account for flow resistance at higher Reynolds numbers where inertial effects become significant. The model also requires specifying the porosity of the medium, which determines the void fraction available for fluid transport.

Beyond flow-related properties, the porous zone is characterized by the thermal and physical properties of the solid matrix (textile), including density, thermal conductivity, and specific heat capacity, which govern the conduction and thermal storage behavior of the fabric. To properly model radiative heat exchange within the porous textile, radiative properties must also be defined: these include surface emissivity, absorption coefficient, scattering coefficient, and refractive index. Together, these parameters allow for detailed modeling of radiative processes such as absorption, reflection, transmission, and self-emission occurring within the fabric’s microstructure.

When modeling fabric as a porous material, it is crucial to recognize that the boundary conditions at the interface between the porous medium and the surrounding fluid domain can significantly influence the predicted heat and mass transfer behavior. Fabrics, due to their fibrous structure, allow for varying degrees of permeability, meaning that air and moisture can flow through them depending on porosity, fiber arrangement, and weave tightness. In computational simulations, the treatment of these boundaries commonly referred to as wall type determines how momentum and thermal energy are exchanged between the porous interior and the external flow field. The classic work of Somerton and Wood (1988) on the effect of walls in modeling flow through porous media established that impermeable walls can artificially increase local velocities in the porous medium due to the suppression of cross-flow, leading to overestimation of pressure drops and altered velocity profiles. Conversely, fully open boundaries permit lateral flow, which can reduce velocity gradients near the interface and change the overall transport characteristics. In the context of clothing systems, this finding means that using a fully impermeable wall condition to represent a fabric-covered body segment could underestimate the heat and moisture transfer compared to a realistic semi-permeable condition, where some airflow penetrates the fabric.

To calculate thermal insulation to dry heat transfer for a one-layer fabric-covered cylinder (Cotton/porous zone), multiple simulations were conducted using a range of permeability values ranging from very high to very low to capture the thermal response of the system. Additionally, various porosity values were analyzed, including 5%, 27%, 50%, and 99% porosity.

Generally, higher porosity in a porous material leads to better insulation. This is because high porosity results in a larger amount of void space within the material, which is typically filled with air, thus reducing the efficiency of heat transfer through the fabric. Moreover, the presence of air gaps significantly reduces conduction and convection, making the material more thermally resistive.

While high porosity often correlates with high permeability in porous media, it is important to note that the relationship is not strictly linear. Permeability, defined as the material's ability to allow fluid to pass through it is also governed by the connectivity and geometry of the pores, as supported by multiple research studies on porous structures.

A permeability of 1×10^{-9} m² represents a very low capability for air or fluids to penetrate through the cotton fabric. In the context of clothing applications, such a low permeability implies a tightly woven or dense structure that limits air and moisture transport. Although cotton fabrics are generally considered breathable, a fabric with a permeability as low as 1×10^{-11} m² suggests an extremely compact structure, effectively reducing its porosity and subsequently increasing its thermal insulation capabilities.

Table 6.3 Parameters of the fabric simulated. (The air permeability values were obtained from the literature (Chen, Y. S., Fan, J., Qian, X., & Zhang, W., 2004).

Fabric parameters	**Value**
Thickness, l	6.5 mm
Porosity, φ	27%
Air permeability	1×10^{-9} m²
Fiber density, ρ_s	1380 kg/m³
Fiber specific heat, c_{ps}	1200 J/kg·K
Fiber thermal conductivity, k_s	0.136 W/m·K
Fabric surface emissivity, ε	0.9

Table 6.3 summarizes the thermal and physical properties of the fabric used in the simulation. A high surface emissivity of 0.9 suggests strong capability for thermal radiation exchange. These parameters were implemented to accurately model the fabric as a porous medium in ANSYS Fluent.

To make a fabric layer in Fluent, which is modeled as a porous medium, behave more like a solid layer we needed to adjust the porous media model parameters such as viscous and inertial resistance coefficients: These coefficients define the resistance to flow within the porous medium. To simulate a solid-like layer, we set these coefficients to very high values. High values for viscous and inertial resistance will significantly prevent fluid flow, effectively making the porous layer behave like a solid one. A porosity of 5% for a porous zone was set to represent the material of the fabric to simulate a solid like layer.

To model a highly permeable mesh-like fabric layer in ANSYS Fluent using the porous media approach, the viscous and inertial resistance coefficients were set to very low values. These low resistance values allow for minimal obstruction to airflow through the medium, mimicking the behavior of a lightweight, breathable mesh fabric. Additionally, a high porosity of 99% was assigned to reflect the large volume fraction of voids within the structure. This configuration enables the fabric layer to behave more like an open, air-permeable textile, accurately representing the characteristics of a mesh fabric in thermal and flow simulations.

The thermal insulation of a fabric layer can be evaluated using two distinct approaches, each offering a unique perspective on the heat transfer characteristics of clothing systems. The first method involves calculating the total heat loss at the skin surface and comparing it to a benchmark case using a bare cylinder. This approach uses the equation:

$$q_{tot}\left(\frac{W}{\mathrm{m2}}\right) = \frac{\Delta T=30}{R_{fab}+R_{cy}} \tag{6.25}$$

Where R_{fab} represents the thermal resistance of the fabric layer, and $R_{cy}$is the resistance of the bare cylinder. By obtaining the total heat transfer at the skin surface from CFD data, the equation can be rearranged to isolate R_{fab} , effectively quantifying the additional insulation provided by the fabric layer over the baseline. This method is particularly useful when trying to evaluate the net insulating impact of clothing under steady-state conditions.

The second approach focuses on local heat flux at the inner surface of the clothing (fabric wall), using the equation:

$$Q\ (\frac{W}{\mathrm{m2}}) = \frac{\Delta \mathrm{T}}{R_{fab}} \tag{6.26}$$

Where, ΔT is the temperature difference across the fabric layer. This method assumes one-dimensional heat conduction and radiation through the fabric and calculates insulation directly based on simulated thermal gradients and resulting flux. It is particularly useful in CFD modeling, where detailed temperature fields can be evaluated using area weighted average of the surface temperature at inner and outer clothing walls. This approach isolates the fabric layer itself, independent of external flow conditions, providing a direct measure of material performance. While the bare cylinder method gives a system-level overview, the temperature gradient method provides insight into the fundamental thermal resistance of the fabric, especially useful in comparing different textile materials or layer configurations. Both approaches yielded consistent results in evaluating the thermal insulation of porous or fabric-covered cylinders.

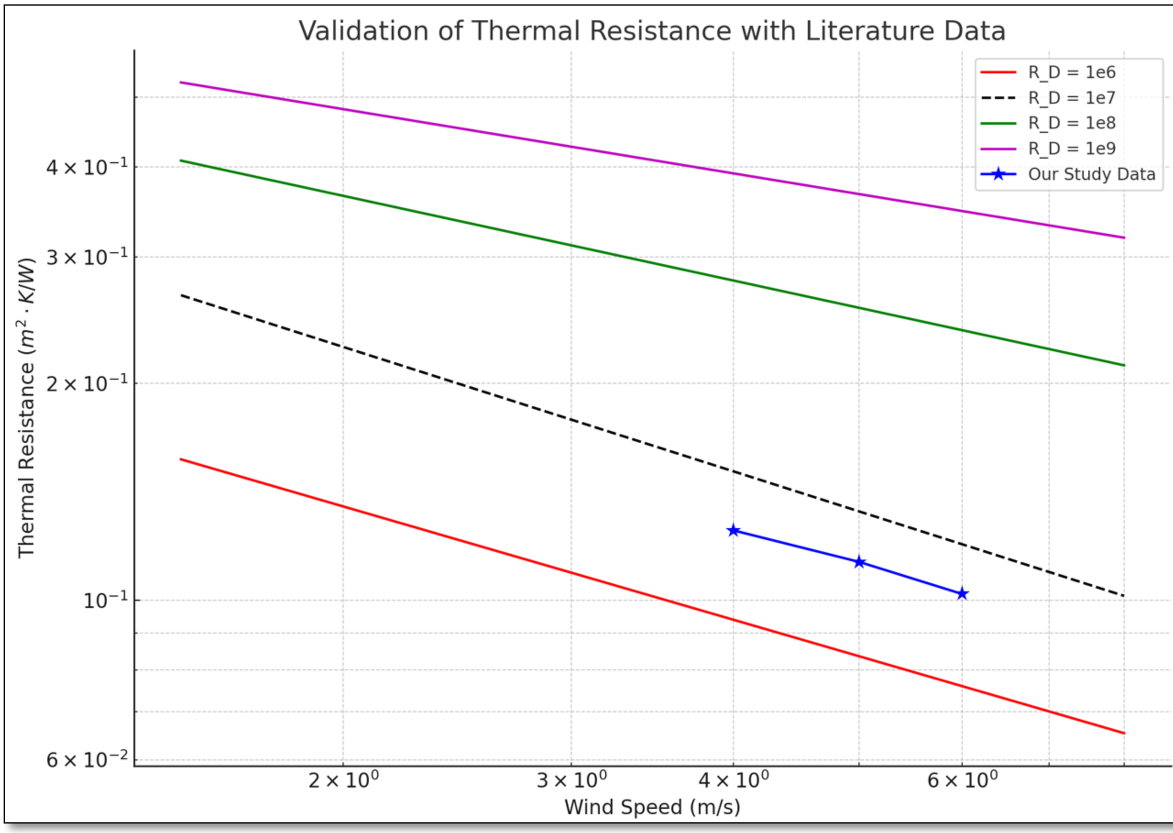

Figure 6.14 Validations of the thermal resistance results from our study against the benchmark data from literature for fabric-covered cylinders under crossflow conditions (U.S. Army Natick Soldier Research, Development & Engineering Center, 2003).

Figure 6.14 presents a detailed validation of the simulated thermal resistance results against benchmark data available in the literature for fabric-covered cylinders under crossflow conditions, originally reported by the U.S. Army Natick Soldier Research, Development & Engineering Center (2003). To enable a direct comparison, the data curves for different fabric air-flow resistances $R_D = 1 \times 10^6$, 10^7, 10^8, and 10^9 m^{-1} were digitally reconstructed from the published figures. Each curve illustrates the characteristic trend of decreasing thermal resistance with increasing wind speed, corresponding to the transition from conduction-dominated to convection-dominated heat transfer as the external flow intensifies. Lower-resistance fabrics (e.g., $R_D = 1 \times 10^6$ m^{-1}) permit greater permeability, leading to enhanced convective coupling and lower overall resistance, while highly resistive materials ($R_D \geq 10^8$ m^{-1}) behave more like impermeable barriers, maintaining higher insulation values across all flow regimes.

In this figure, our simulation data points (blue stars) represent the predicted thermal resistances for a porous fabric-covered cylinder exposed to airflow velocities of 4, 5, and 6 m/s. These results fall consistently between the literature curves corresponding to $R_D = 10^6$ and 10^7 m^{-1}, indicating that the porous-media parameters used in our CFD model accurately represent a moderately permeable textile layer, a condition characteristic of common single-layer clothing fabrics. This placement also confirms that the simulated flow resistance and effective permeability align well with empirical expectations, reinforcing that the chosen fabric properties, such as porosity, thickness, and viscous resistance coefficients, are physically realistic and correctly implemented within the porous-media formulation.

The strong agreement observed between our simulation results and the benchmark literature data validates both the numerical methodology and the porous-media modeling approach adopted in this study. The similar slope and magnitude of the resistance–velocity relationship across the datasets demonstrate that the CFD model reliably captures the essential physics of convective and conductive heat transfer through textile-covered cylindrical surfaces. This close correspondence provides confidence that the computational framework developed here can be extended to more complex geometries, such as human body segments or multi-layered protective garments, while maintaining fidelity to established experimental findings.

Figure 6.15 The experimental thermal insulation data recorded for different regions of the manikin test dressed in a single layer of a long-sleeved cotton T-shirt.

Table 6.4 Experimental thermal insulation data for selected body regions (single-layer long-sleeved cotton T-shirt).

Body Region	R_{CT} (Clo)
Right Upper Arm	0.828
Left Upper Arm	0.86
Right Forearm	0.821
Left Forearm	0.797

Moreover, to further validate the numerical results obtained from our CFD simulations, an experimental test was conducted using a thermal manikin dressed in a single layer of a long-sleeved cotton T-shirt. The manikin was placed inside a controlled environmental chamber, as illustrated in Figure 6.15 and Table 6.4, where environmental conditions such as ambient temperature and airflow were carefully regulated. In this setup, the average air velocity was maintained at approximately 3.5 m/s to match the simulation conditions.

The experimental thermal insulation data were recorded for different regions of the manikin body, including localized zones such as the upper arm and forearm. These regional fabric thermal resistance values were quantified in clo units (1 clo is equivalent to 0.155 K·m²/W), a standard measure of clothing insulation. The measured values were then directly compared with the thermal resistance values computed from the CFD simulations under identical conditions see equations below. The comparison aimed to assess the accuracy and predictive capability of the numerical model in estimating heat transfer through fabric-covered surfaces under forced convection.

$$132.985\ \frac{W}{m^2} = \frac{30\ K}{R_{fabric} + (R_{cy=0.0764})} \tag{6.27}$$

$$R_{fabric} = 0.1419\ \frac{m^2 K}{W} \longrightarrow \quad 0.9425 \text{ clo} \tag{6.28}$$

$$\%\text{error} = \frac{|0.86 - 0.9425|}{0.86} \times 100\% = 9.51\% \tag{6.29}$$

With a percent error of only 9.5% between the CFD simulation results and the manikin test data, the comparison falls well within acceptable validation margins. This close agreement confirms the reliability of the numerical model. Overall, this validation approach provided strong confidence in the simulation methodology, particularly in accurately capturing the heat transfer characteristics of porous textile layers exposed to dynamic airflow conditions.

6.5 Temperature distribution and air flow models

The velocity and temperature contour plots for the three modeled configurations, low-porosity fabric (5%), high-porosity fabric (99%), and the bare (nude) cylinder, illustrate different variations in airflow behavior and heat transfer performance across the cylindrical surface under crossflow conditions. As shown in Figures 6.17 through 6.19, the low-porosity case demonstrates significant flow blockage and higher boundary-layer thickness, indicating stronger thermal insulation and reduced convective heat exchange. On the other hand, the high-porosity configuration allows greater air penetration through the fabric layer, resulting in thinner thermal boundary layers and enhanced convective cooling. The bare cylinder, serving as the reference case, displays the most direct fluid–surface interaction, producing the highest local velocity gradients and heat transfer rates. Collectively, these results highlight how porosity governs the aerodynamic and thermal characteristics of fabric-covered cylindrical geometries, emphasizing the importance of accurately modeling fabric permeability when predicting mixed convection behavior.

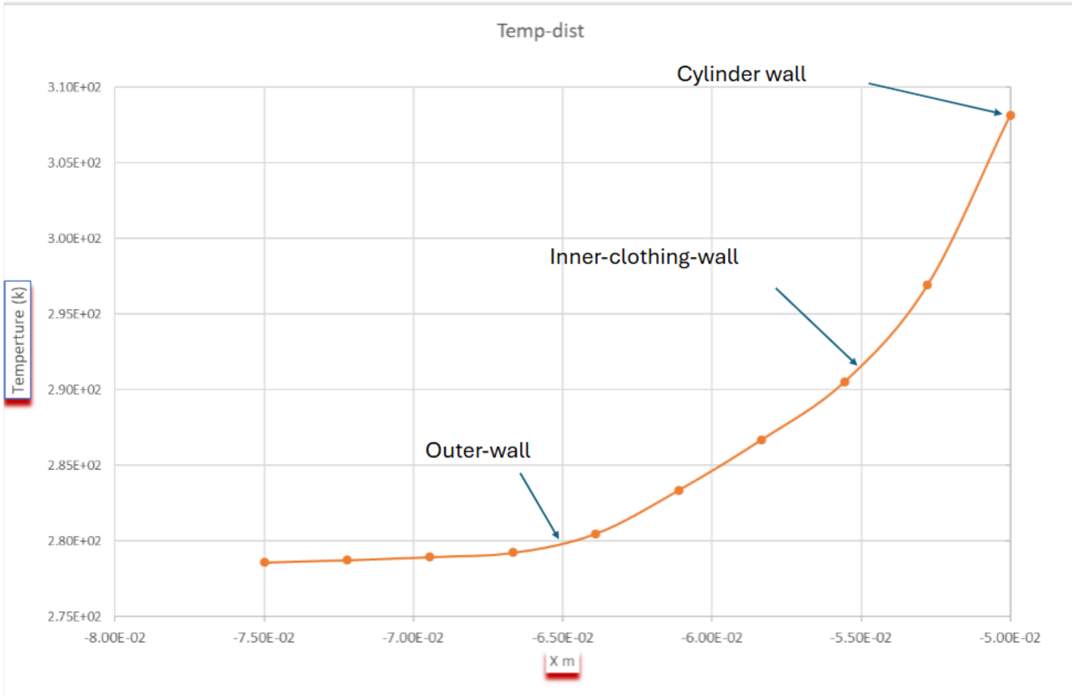

Figure 6.16 The temperature distribution across the cylinder-air gap-fabric layer configuration.

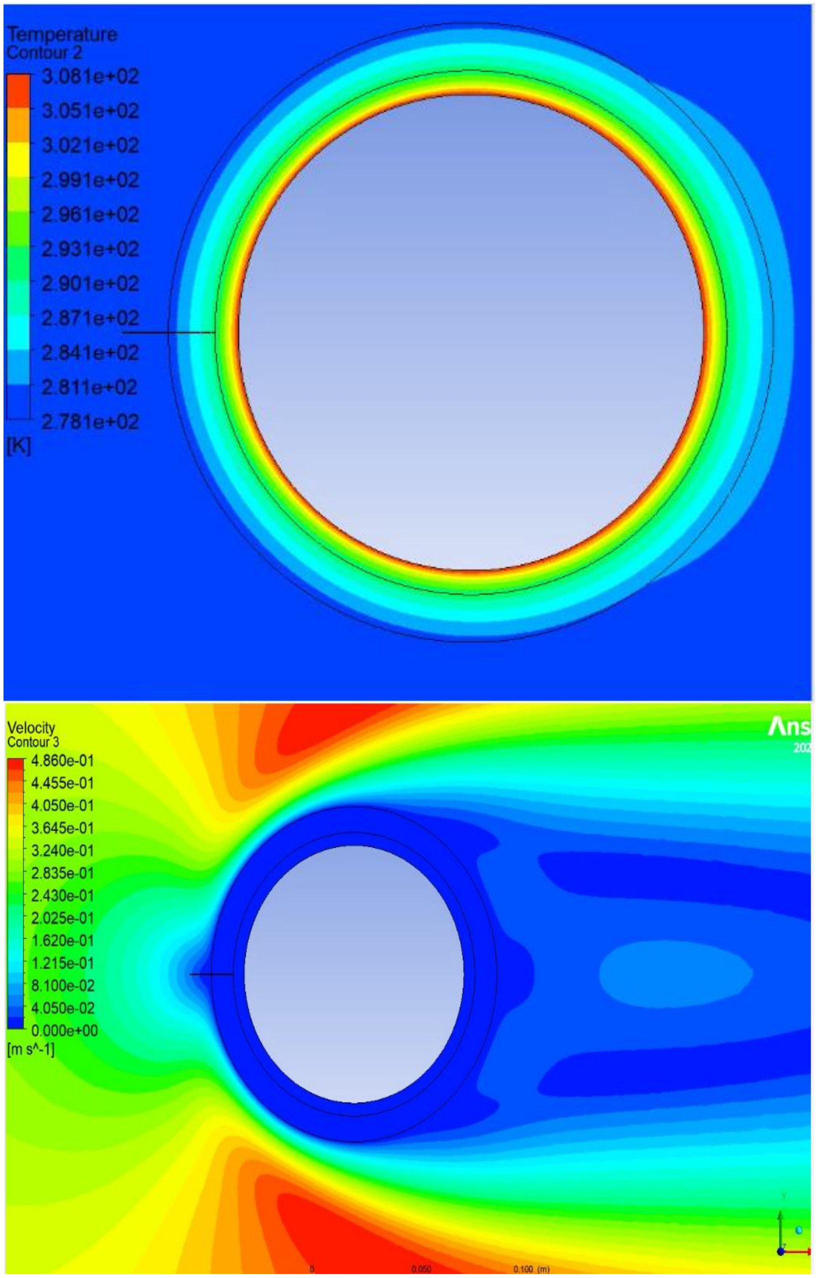

Figure 6.17 Temperature and velocity contours for flow over a 2D fabric covered cylinder (simplified 2D arm with single fabric layer), fabric modeled has very low permeability and porosity of (5%). Average air velocity= 3.5m/s.

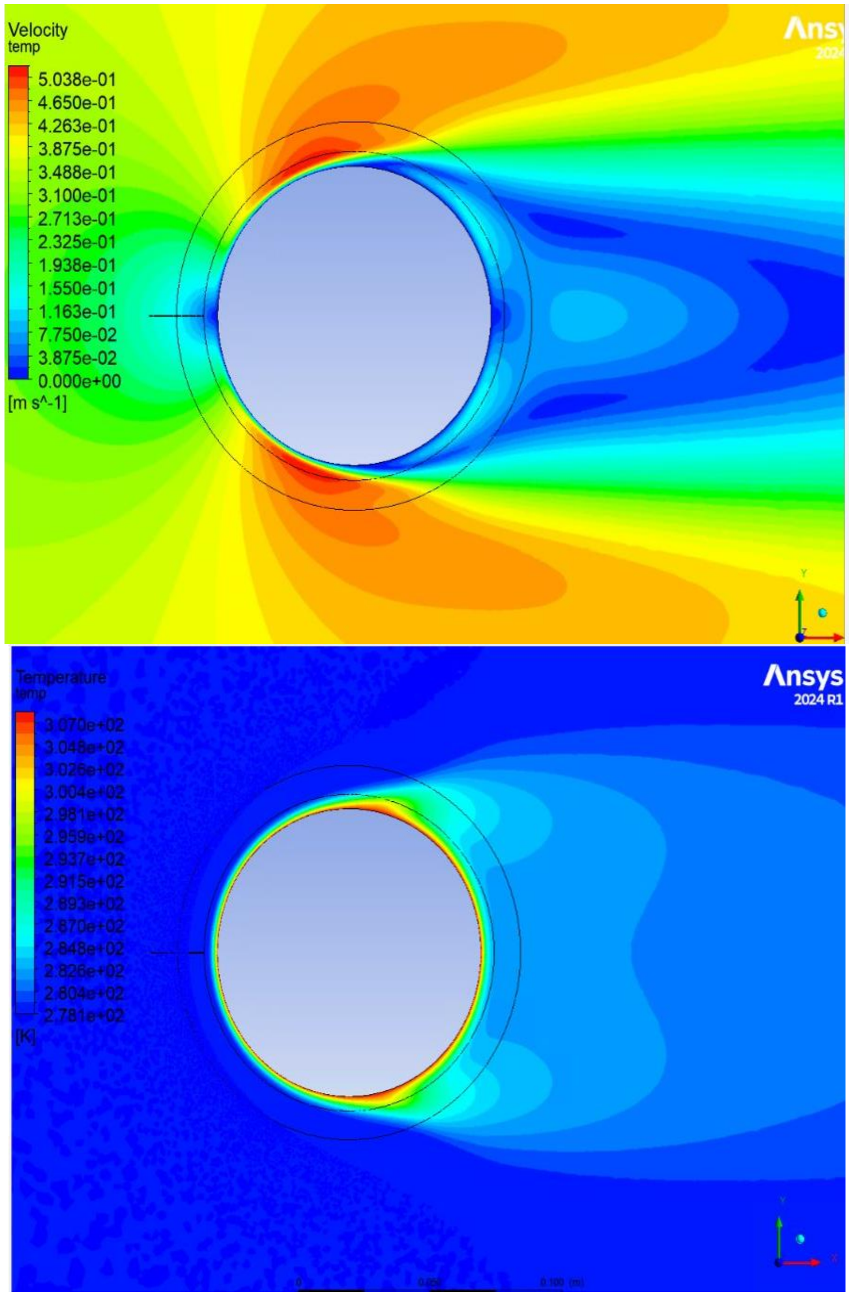

Figure 6.18 Temperature and velocity contours for flow over a 2D fabric covered cylinder (simplified 2D arm with single fabric layer), fabric modeled has very high permeability and porosity of (99%). Average air velocity= 3.5m/s.

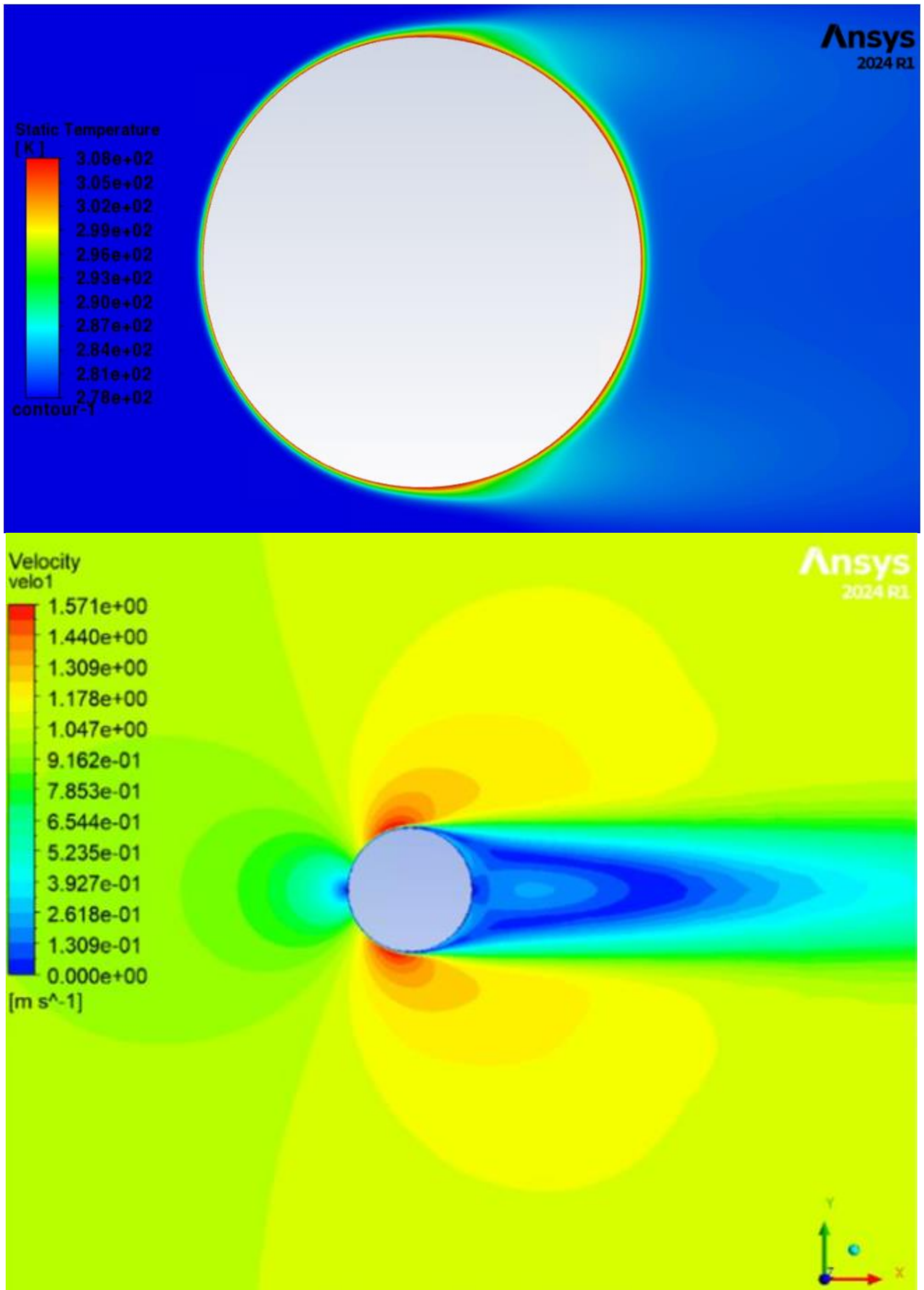

Figure 6.19 Temperature and velocity contours for flow over 2D bare cylinder. Average air velocity= 3.5m/s.

In the case of the low porosity (5%) contours, the fabric layer behaves similarly to a solid shell due to its extremely low permeability and high airflow resistance. The temperature contours show a clear thermal boundary layer close to the surface, with minimal convective penetration into the fabric, indicating strong insulation. The velocity contour reveals a clear flow detachment and wake region behind the cylinder, with very low velocities within and around the porous layer, suggesting that the airflow is effectively blocked. This configuration simulates a solid-like insulation where heat transfer from the cylinder to the external environment is significantly reduced. The temperature distribution across the fabric thickness (seen in the temperature profile plot, Figure 6.17) confirms the existence of a steep thermal gradient, reinforcing the strong insulating character of the material.

In contrast, the high porosity (99%) case represents a mesh-like, highly breathable fabric. The velocity contours show much greater air penetration through the porous layer, resulting in higher velocities around and inside the fabric. This increased permeability allows the external flow to interact with the cylinder surface more directly, enhancing convective heat transfer. The temperature contours indicate a more uniform distribution across the cylinder's surface, suggesting reduced thermal resistance compared to the low-porosity case. This behavior is typical for fabrics with high openness and low thermal insulation, such as mesh or net-like textiles used in hot climates.

Finally, the bare cylinder scenario, serving as the benchmark case, exhibits the highest surface exposure to airflow. The velocity field is characterized by an open, symmetrical wake pattern and maximum external flow velocity. Temperature contours indicate the thinnest boundary layer, resulting in the most effective convective cooling. As no insulating layer is present, the heat transfer is most efficient, and the surface temperature of the cylinder is lowest among all cases.

Comparing all three cases, the addition of a low-porosity fabric significantly increases the thermal resistance, effectively reducing heat loss and mimicking a solid layer. The high-porosity configuration, on the other hand, provides moderate resistance, allowing for airflow interaction and higher heat dissipation, making it suitable for breathable clothing. These comparisons are crucial for applications in thermal manikin modeling and human thermal comfort simulations, where accurately representing fabric insulation is essential. The results validate the modeling strategies used for simulating both solid-like and mesh-like textile behavior in CFD.

The temperature distribution across the cylinder–air gap–fabric layer configuration (see Figure 6.16) reveals the thermal resistance behavior of the composite system, which is critical for understanding heat transfer through clothing or protective textile layers. In this arrangement, the inner surface of the cylinder is maintained at a higher temperature (simulating human skin temperature at 308.15 K), and heat is transferred outward through the intervening layers to the ambient air.

Starting at the cylinder wall, the temperature is highest due to the internal heating condition. As heat moves radially outward, it first crosses a thin air gap, where conductive and convective heat transfer dominate. This gap introduces an initial temperature drop, which varies depending on the airflow and the thickness of the gap.

The heat then enters the inner surface of the fabric layer, where conduction through the solid matrix of the textile fibers, as well as potential radiative and convective interactions within the porous structure, governs the thermal transport. The temperature drops progressively across the fabric thickness, depending on the material’s porosity, thermal conductivity, specific heat, and flow resistance properties. For low-porosity fabrics, the drop is steeper due to the higher resistance to heat flow; for high-porosity fabrics, the gradient is more gradual due to enhanced convective mixing and lower insulation performance.

Finally, at the outer surface of the fabric, the temperature reaches its lowest value, where it is exposed to the ambient flow. The overall profile thus shows a continuous decline in temperature from the inner cylinder wall to the outer surface, with the steepness and shape of the gradient strongly influenced by the fabric's permeability and porosity. This distribution is essential in evaluating the thermal insulation performance of clothing systems and helps quantify the effective thermal resistance of multilayer assemblies.

Chapter 7. Results, Discussion, and Integration

7.1 Flow visualization results

Simulation-based flow visualization provides valuable insights into the interaction of forced and natural convection around the human body under mixed crossflow conditions. In this study, both computational fluid dynamics (CFD) simulations and controlled experiments were conducted for cases where the angle between the incoming air stream and the gravitational direction was 90° a realistic representation of typical indoor ventilation and certain environmental exposures. While natural and forced convection have been widely studied independently, there is limited research in the current literature on investigations that examine mixed cross-flow conditions involving complex human shapes.

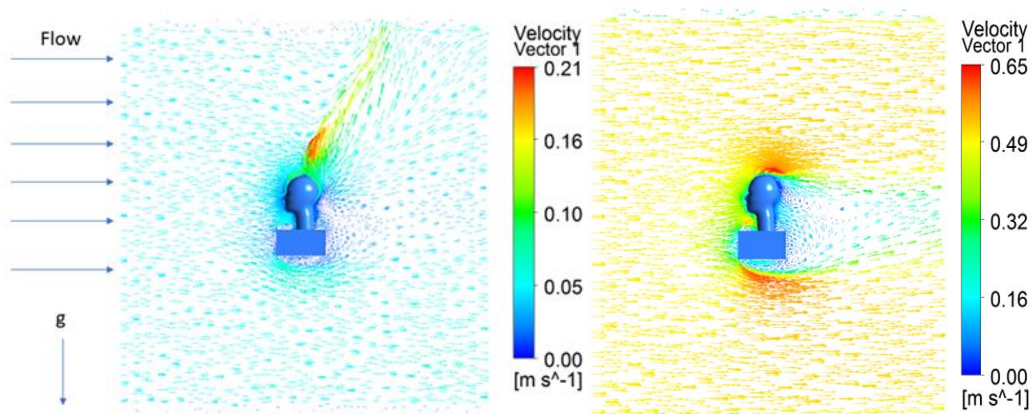

(A) (B)

Figure 7.1 Assisting cross flow over a thermal head, velocity vector map (A) V_{air} = 0.05m/s, T_{air} = 293.15K; (B) contours V_{air} = 0.5m/s, T_{air} = 293.15K.

Figure 7.1(B) illustrates the velocity contour map for assisting crossflow over the thermal head at an air velocity of 0.5 m/s and an ambient air temperature of 293.15 K. Compared to the lower velocity case (Figure 7.1A), the contours in Figure 7.1(B) reveal a more dominant forced convection regime, where inertial forces overcome buoyancy effects. The airflow is observed to sweep over the head's surface, reducing the thickness of the boundary layer and increasing the overall convective heat transfer. The thermal plume that was more vertically aligned in the low-velocity case becomes tilted and elongated downstream, indicating a stronger interaction between the incoming air and the wake region behind the head. This pattern confirms that at higher air velocities, forced convection governs the heat transfer mechanism, suppressing the buoyancy-driven plume typically seen in mixed convection scenarios. The CFD results presented here ensure that the observed flow structures and heat transfer patterns in this thesis analysis are physically meaningful and not numerical artifacts.

The human thermal manikin was positioned at the geometric center of the computational domain to ensure symmetric airflow development and eliminate wall effects. The inlet velocity and thermal boundary conditions were defined to replicate those used in the experimental setup, ensuring consistency between the CFD model and laboratory testing. Velocity contours were produced for a range of inlet velocities to visualize flow behavior, with particular emphasis on the 0.5 m/s case illustrated in Figure 7.2(A). At this velocity, forced convection becomes the dominant mechanism, effectively suppressing the buoyant rise of the thermal plume generated by the warm surface of the manikin. The stronger inertial forces redirect the plume downstream, resulting in a broad low-velocity recirculation zone above the head and the formation of symmetrical vortical structures along both sides of the body. These vortices extend downstream and enhance mixing in the wake region. This flow behavior aligns well with the Richardson number (Ri) analysis discussed earlier in Chapter 5: Nusselt Number Correlation Development, which demonstrated that when $Ri < 1$, inertial effects dominate buoyancy, marking the transition to a forced convection regime.

Figures 7.2 (B) and 7.2 (C) present the total heat flux and radiative heat flux distributions, respectively, for the 0.5 m/s case. The CFD-predicted total heat flux distribution exhibits improved left–right symmetry relative to experimental infrared imaging results, particularly around the thighs and calves. This improvement can be attributed to the idealized boundary conditions in simulation, which eliminate minor asymmetries in flow distribution and surface properties present in physical testing.

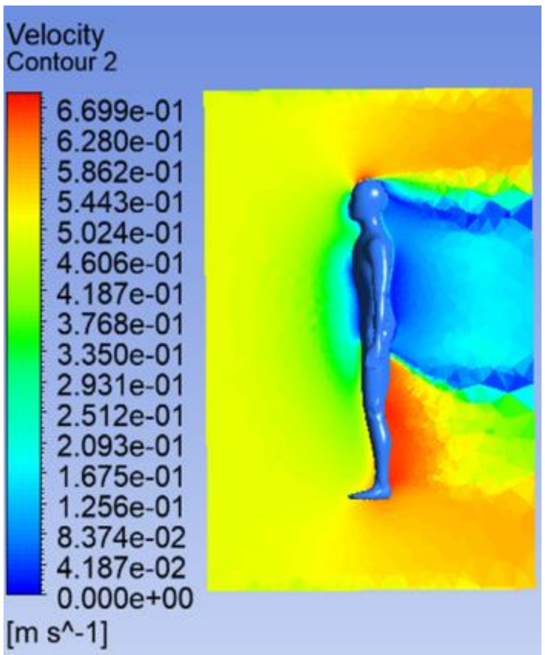

(A)

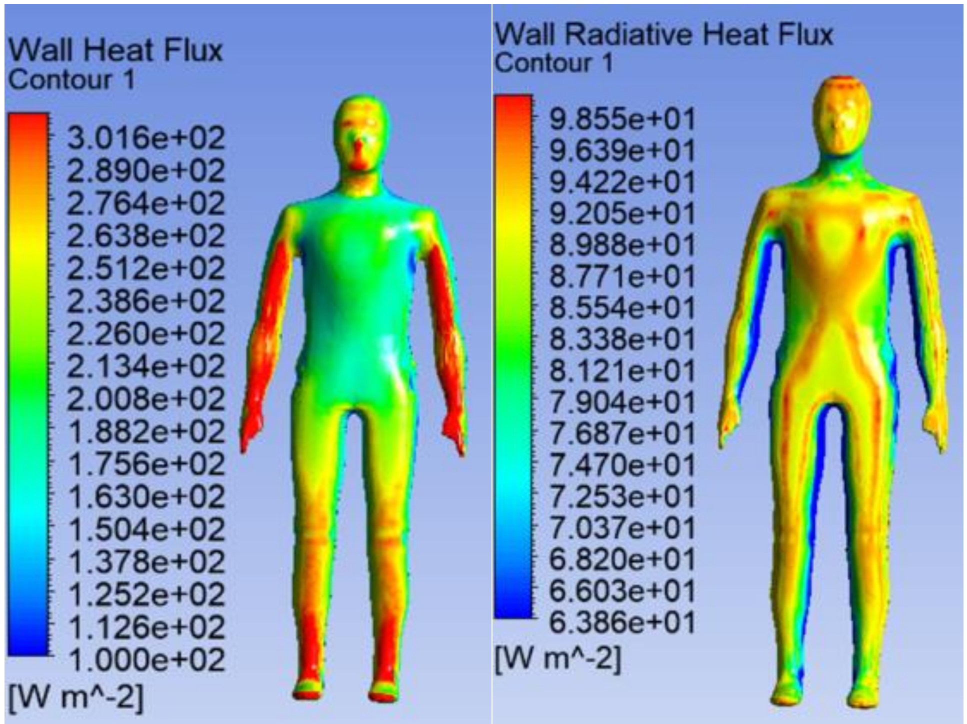

(B) (C)

Figure 7.2 (A) Velocity contours V_air = 0.5m/s, T_air = 293.15K (B) Heat flux distribution of manikin surface (C) Radiative heat flux distribution.

The windward regions including the forehead, nose, and chest exhibit the highest local heat flux values, driven by thinner thermal boundary layers and direct exposure to incoming flow. Conversely, downstream surfaces such as the rear torso and calves show reduced heat transfer rates due to wake effects and reduced flow impingement. This spatial variation in local heat transfer aligns with the local Nusselt number patterns predicted by the correlation development section, where Nu increases with local Reynolds number.

The radiative heat flux distribution (Figure 7.2 (C)) reveals that radiation accounts for up to 40–50% of total heat loss in certain regions, consistent with the findings in this thesis

(Radiative Heat Transfer Coefficient Analysis). Radiative contributions are highest in surfaces with a large view factor to the chamber walls, such as the upper torso and head, and lowest in recessed or shaded areas like the inner thighs. This pattern reinforces the conclusion from the correlation work that convective and radiative processes must be treated as coupled phenomena for accurate whole-body heat transfer predictions.

The insights from flow visualization directly support the derivation and structure of the mixed convection Nusselt number correlation, specifically:

1. Plume suppression at high Re (Figure 7.2 A) explains the dominant forced convection term in Equation 7.2, where Nu is proportional to Re^{n2} for high-velocity conditions.
2. Strong buoyancy-driven upward flow at low Re (observed in additional simulations) justifies the inclusion of the natural convection term Gr^{n4} in the correlation, with its influence increasing as Ri rises.
3. Region-specific heat transfer variations seen in Figures 7.2 (B) and 7.2 (C) highlight why a simple whole-body averaged h_c can cover local extremes supporting the correlation's applicability to both local and average Nusselt number estimation.

These qualitative and quantitative consistencies between flow visualization, CFD validation, and empirical correlation results enhance the robustness of the present work. The observed flow structures not only validate the simulation methodology but also confirm the physical plausibility of the derived correlation for predicting mixed convection heat transfer from complex human geometries.

Chapter 8. Conclusions and Future Work

8.1 Summary of key findings

This research integrates results from three complementary CFD studies: a detailed thermal manikin head model, a full standing nude manikin model, and a two-dimensional clothing microclimate model. Together, these analyses provide a multi-scale understanding of human heat transfer under mixed convection conditions.

The head segment simulations characterized local convective heat transfer coefficients (h_c), heat flux distributions, and the interplay of forced and natural convection over a range of air velocities $(0.05 \leq v_{air} \leq 1.00.05 m/s)$ and temperature differences $(T_{head} - T_{air} = 5 - 30 \circ C)$.

Key outcomes include:

- **Convective heat transfer behavior**: Increasing both velocity and temperature difference elevated h_c, with predicted values matching experimental measurements within ±2%, confirming model accuracy.
- **Flow regimes**: At low velocities, buoyancy dominated, producing vertical plumes that deviated due to crossflow; higher velocities suppressed plume rise and extended downstream wake regions.
- **Correlation development**: Using Buckingham's π-theorem, forced and natural convection correlations were derived and combined into a mixed-convection form:

$$\mathrm{N}u_{mixed} = ((0.37 \times Re^{0.58} \times Pr^{\frac{1}{3}})^3 + (0.485 \times Gr^{\frac{1}{4}} \times Pr^{\frac{1}{4}})^3)^{\frac{1}{3}}$$

Constants were determined using the Generalized Reduced Gradient (GRG) method, yielding high predictive accuracy.

- Local heat flux distribution: Maximum total heat flux reached approximately 364 W/m² at the nose tip, while radiant heat flux contributed up to 50% of the total heat loss in some regions.

These results guided mesh refinement near high-gradient regions (nose, forehead, ears) and informed boundary condition definitions using validated head surface temperatures. Extending the head study methodology to the full standing posture enabled quantification of integrated convective and radiative exchanges under stagnant and moving air conditions. Air velocities ranged from 0.05 m/s to 0.35 m/s, with surface h_c values mapped across the body.

Key outcomes include:

- **Natural vs. Forced Convection:** For stagnant or low-velocity air, the whole-body natural convection coefficient was 3.76 W/m²·K, consistent with mid-range literature values. Forced convection coefficients increased with velocity, closely following the ASHRAE correlation h_c = 14.8 $V_{air}^{0.69}$ (ASHRAE, 2017).
- **Agreement with Literature:** Predicted h_c values matched experimental findings by Fanger (1970), Murakami et al. (1997), and Brohus for standing posture conditions.
- **Radiative Exchange:** Whole-body radiative coefficients ($h_r = 4.93 W/m^2 \cdot K$) were in close agreement with ASHRAE's 4.7 W/m²·K and Ichihara et al.'s 4.3 W/m²·K.

These results confirmed that localized head convection values are typically higher than whole-body averages due to increased curvature and exposure but must be evaluated in the context of total body heat exchange.

The two-dimensional model analyzed heat transfer through skin–clothing air gaps and across clothing layers, enabling control of parameters such as air gap thickness, fabric conductivity, and emissivity.

Key outcomes include:

- **Air Gap Effects:** Thin air gaps reduced natural convection, increasing conductive heat transfer. Larger gaps enhanced buoyancy-driven flow but introduced temperature variability.
- **Material Properties:** Low-conductivity insulation reduced both conduction and convection; high-emissivity fabrics increased radiative heat loss to the environment.
- **Link to Nude Body Studies:** Demonstrated that clothing layers attenuate airflow patterns seen in nude manikin simulations, significantly altering local h_c and h_r. This model also served as a computationally efficient test platform for mesh sensitivity and turbulence model selection before application in the complex full-body geometry.

Together, the three models provide a multi-scale framework for predicting human heat transfer:

1. **Local detail (Head Model):** Critical for targeted heating/cooling applications such as helmets, headgear, and localized ventilation.
2. **Whole-body integration (Full Manikin):** Supports thermal comfort standards, HVAC system optimization, and environmental ergonomics.
3. **Clothing microclimate (2D Arm):** Bridges the gap between idealized nude-body heat transfer and real-world dressed conditions.

The iterative modeling workflow where experimental measurements informed CFD boundary conditions, and outputs from one model refined the next—ensures consistency and reliability across scales. The validated correlations developed herein have immediate application in building design, and human thermal comfort assessment.

8.2 Conclusions

This thesis presented an integrated experimental and computational investigation of mixed convection heat transfer from the human head, full body, and clothing microclimate, with particular emphasis on developing predictive Nusselt number correlations applicable to complex geometries and realistic thermal conditions. High-fidelity CFD models, validated against controlled experimental measurements, successfully captured the combined effects of forced and natural convection, surface radiation, and flow–thermal interactions. The results demonstrated strong agreement between CFD predictions and measured data, with relative percentage differences typically within ±2%. Flow visualization revealed the transition from buoyancy-dominated plumes at low air velocities to inertial-force-driven wake structures at higher velocities, confirming the interplay between Reynolds and Grashof number effects. The final semi-empirical correlations derived using the power-law approach provided accurate, dimensionless representations of heat transfer behavior across a broad range of flow regimes, offering both practical applicability and theoretical consistency.

Beyond confirming the validity of the developed models, this work also advanced the understanding of human thermophysiology in environmental contexts by linking localized heat flux patterns with full-body convective performance. The findings showed that geometric complexity, posture, and microclimate layer thickness significantly influence convective and radiative heat transfer mechanisms. Importantly, the proposed correlations extend beyond the human thermal comfort field, offering potential applications in sports science, protective clothing design, and thermal safety engineering. By bridging experimental rigor with numerical precision, this research provides a robust framework for predicting heat transfer from irregularly shaped, thermally active bodies in mixed convection environments—laying the groundwork for future refinement through transient simulations, physiological coupling, and variable clothing permeability modeling.

8.3 Recommendations for further research

Recommendations for future studies are provided, emphasizing the need for dynamic models and further validation in real-world scenarios. While this thesis has established an essential CFD-based framework for analyzing heat transfer from the human body under mixed convection conditions, several research directions remain open to expand the applicability and precision of these findings. First, future studies should explore a wider range of postures, activity levels, and ambient flow orientations. The current simulations focused primarily on standing postures with perpendicular crossflow to gravity, but real-world scenarios often involve dynamic or asymmetrical exposure, such as walking in varying wind directions or performing occupational tasks in non-uniform thermal environments. Including transient CFD simulations that capture time-dependent changes in skin temperature, sweat evaporation, and transient plume formation could yield deeper insight into thermal comfort prediction. Moreover, expanding the parameter space to include extreme Reynolds and Grashof numbers beyond the present study's range would test the robustness of the proposed mixed-convection correlations and extend their validity to more diverse environmental conditions, such as high-speed airflow in sports or low-gravity environments in aerospace applications.

A second key area for further research is the incorporation of physiological responses and thermoregulation mechanisms into the CFD models. The current approach assumes steady-state surface temperatures and does not account for the dynamic regulation of blood flow, sweat production, and metabolic heat generation, which can significantly alter local and whole-body heat transfer rates. Coupling the CFD models with bioheat transfer equations such as the Pennes bioheat model or integrating multi-node thermophysiological models like Fiala or Stolwijk (Stolwijk, 1970; Fiala et al., 2001), would provide a more complete representation of human-environment interactions. This would allow simulations to predict not only external heat transfer coefficients but also internal thermal states, making the results directly applicable to thermal stress assessment, occupational safety, and medical applications. Such integration would also enable studying the effects of age, body composition, and health status on heat exchange, bridging the gap between engineering-based CFD studies and human physiology research.

Finally, further work should be dedicated to extending the modeling framework to realistic clothing systems and complex surface materials. While the two-dimensional clothing microclimate model in this study demonstrated the effect of air gap thickness, fabric conductivity, and emissivity on heat transfer, future models should account for three-dimensional garment geometry, fabric porosity, and moisture transport through textile layers. This would enable simulations that capture coupled heat and mass transfer, including the impact of evaporative cooling under both dry and humid conditions. Additionally, validating such models against controlled wind tunnel experiments with instrumented thermal manikins wearing various clothing ensembles would improve predictive accuracy. Incorporating computational textile modeling to represent weaves structure and fiber-level thermal properties could also enhance the realism of predictions. These developments would make the CFD framework directly relevant to apparel design, sports engineering, protective clothing evaluation, and climate-specific clothing optimization.

References

Acharya, J., Bhanja, D., & Misra, R. D. (2024). A modified model to assess the thermal protective performance of fire-retardant clothing exposed to both flame and radiant source. Applied Thermal Engineering, 242, 122422.

Ansys Inc. (2024). Ansys SpaceClaim User Guide. Ansys Documentation.

Asawo, T., Torvi, D., & Sumner, D. (2023). Measuring convection heat transfer coefficients and thermal resistance for protective fabrics using a heated cylinder in a wind tunnel. The Journal of The Textile Institute, 114(12), 1909–1917.

ASHRAE. (2005). Thermal comfort. In ASHRAE handbook of fundamentals.

Autodesk Inc. (n.d.). Meshmixer. Retrieved from https://www.meshmixer.com

Cengel, Y. A., & Ghajar, A. J. (2015). Heat and mass transfer: Fundamentals and applications (5th ed.). McGraw-Hill Education.

Cernei, A., Lacassagne, T., Fagniez, T., Danca, P., Georgescu, M. R., Thevenet, F., ... & Nastase, I. (2025). Exploring the impact of clothing insulation on thermal comfort evaluation using thermal manikins. E3S Web of Conferences, 608, 02005.

Chen, Y. S., Fan, J., Qian, X., & Zhang, W. (2004). Effect of garment fit on thermal insulation and evaporative resistance. Textile Research Journal, 74, 742–748.

Choudhary, B., Wang, F., Ke, Y., & Yang, J. (2020). Development and experimental validation of a 3D numerical model based on CFD of the human torso wearing air ventilation clothing. International Journal of Heat and Mass Transfer, 147, 118973.

Churchill, S. W., & Bernstein, M. (1977). A correlating equation for forced convection from gases and liquids to a circular cylinder in crossflow.

Etris, S. F., Sisca, V. K., Lieb, K. C., et al. (1973). Heat transfer in fibrous materials. Journal of Testing and Evaluation, 1, 231–245.

Fiala, D., Lomas, K. J., & Stohrer, M. (2001). A computer model of human thermoregulation for a wide range of environmental conditions. *Journal of Applied Physiology*, **87**, 1957–1972.

Fukazawa, T., & Tochihara, Y. (2015). The thermal manikin: A useful and effective device for evaluating human thermal environments. Journal of the Human-Environment System, 18(1), 021–028.

Gao, C., & McCullough, E. A. (2000). Modeling of airflow and heat transfer around a clothed cylinder. Textile Research Journal, 70(1), 42–49.

Gao, S., Ooka, R., & Oh, W. (2019). Formulation of human body heat transfer coefficient under various ambient temperature, air speed and direction based on experiments and CFD. Building and Environment, 160, 106168.

Gibson, P. (2009). Modeling heat and mass transfer from fabric-covered cylinders. Journal of Engineered Fibers and Fabrics, 4(1), 155892500900400102.

Gibson, P. W. (1997). Transient heat and mass transfer in porous textiles. International Journal of Heat and Mass Transfer, 40(15), 4023–4030.

Gibson, P. W. (2002). Coupled heat and moisture transport in porous polymer materials. Polymer Testing, 21(2), 211–221.

Hager, N. E., Jr., & Steere, R. C. (1967). Radiant heat transfer in fibrous thermal insulation. Journal of Applied Physics, 38(12), 4663–4668.

Havenith, G., et al. (2006). 3D simulation of heat and mass transfer in clothed human models. Ergonomics, 49(14), 1456–1468.

Holmér, I. (1999). Thermal manikins in research and standards. In Proceedings of the Third International Meeting on Thermal Manikin Testing, Sweden, October 12–13.

Holmér, I., & Nilsson, H. (1995). Heated manikins as a tool for evaluating clothing. Annals of Occupational Hygiene, 39(6), 809–818.

Huang, J. (2006). Sweating guarded hot plate test method. Polymer testing, 25(5), 709-716.

Human Solutions GmbH. (n.d.). Human Solutions 3D Body Scanner. Retrieved from https://www.human-solutions.com

Islam, M. R., Golovin, K., & Dolez, P. I. (2023). Clothing thermophysiological comfort: A textile science perspective. Textiles, 3, 353–409.

Joshi, A., Psikuta, A., Bueno, M. A., Annaheim, S., & Rossi, R. M. (2021). Effect of movement on convection and ventilation in a skin-clothing-environment system. International Journal of Thermal Sciences, 166, 106965.

Li, J., Zhang, Z., & Wang, Y. (n.d.). The relationship between air gap sizes and clothing heat transfer performance.

McGuffin, R., Burke, R., Huizenga, C., Hui, Z., Vlahinos, A., & Fu, G. (2002). Human thermal comfort model and manikin (pp. 01–1955).

Modest, M. F., & Mazumder, S. (2022). Radiative heat transfer. Academic Press, Elsevier.

Nielsen, R., Olesen, B. W., & Fanger, P. O. (1985). Effect of physical activity and air velocity on the thermal insulation of clothing. Ergonomics, 28(12), 1617–1631.

Oh, W., & Kato, S. (2018). The effect of airspeed and wind direction on human's thermal conditions and air distribution around the body. Building and Environment, 141, 103–116.

Pan, N. (2007). Material science of clothing: A misunderstood field. Textile Research Journal, 77(1), 1–11.

Pennes, H. H. (1948). Analysis of tissue and arterial blood temperatures in the resting human forearm. *Journal of Applied Physiology*, **1**, 93–122.

Psikuta, A., Allegrini, J., Koelblen, B., Bogdan, A., Annaheim, S., Martínez, N., ... & Rossi, R. M. (2017). Thermal manikins controlled by human thermoregulation models for energy efficiency and thermal comfort research – A review. Renewable and Sustainable Energy Reviews, 78, 1315–1330.

Rogale, D., Firšt Rogale, S., Knezić, Ž., Jukl, N., & Majstorović, G. (2023). Measurement methods of the thermal resistance of materials used in clothing. Materials, 16, 3842.

Rowley, F. B., Jordan, R. C., Lund, C. E., & Lander, R. M. (1951). Gas is an important factor in the thermal conductivity of most insulating materials, Part I. ASHVE Journal Section Heating, Piping, Air Conditioning, 103–109.

Sobera, M. P., et al. (2002). Effect of porous layers on convective heat and mass transfer. International Journal of Heat and Fluid Flow, 23(4), 509–515.

Somerton, C. W., & Wood, P. (1988). Effect of walls in modeling flow through porous media. Journal of Hydraulic Engineering, 114(12), 1431–1448.

Stolwijk, J. A. J. (1970). Mathematical model of thermoregulation. In *Physiological and Behavioral Temperature Regulation* (pp. 703–721).

Strong, H. M., Bundy, F. P., & Bovenkerk, H. P. (1960). Flat panel vacuum thermal insulation. Journal of Applied Physics, 31(1), 39–50.

Su, Y., Tian, M., Li, J., Zhang, X., & Zhao, P. (2022). Numerical study of heat and moisture transfer in thermal protective clothing against a coupled thermal hazardous environment. International Journal of Heat and Mass Transfer, 194, 122989.

Take-uchi, M. (1983). Analysis of wind effect on the thermal resistance of clothing with the aids of Darcy's law and heat transfer equation. Sen'i Gakkaishi, 39(3), T95–T104.

Talukdar, P., Das, A., & Alagirusamy, R. (2016). Estimation of radiative properties of thermal protective clothing. Applied Thermal Engineering, 100, 788–797.

Torvi, D. A. (1997). Heat transfer in thin fibrous materials under high heat flux conditions.

Torvi, D. A., & Dale, J. D. (1999). Heat transfer in thin fibrous materials under high heat flux. Fire Technology, 35, 210–231.

Vallabh, R., Banks-Lee, P., & Seyam, A. F. (2010). New approach for determining tortuosity in fibrous porous media. Journal of Engineered Fibers and Fabrics, 5(3), 155892501000500302.

Verschoor, J. D., & Greebler, P. (1952). Heat transfer by gas conduction and radiation in fibrous insulations. Transactions of the American Society of Mechanical Engineers, 74(6), 961–967.

Wyon, D. P. (1989). Use of thermal manikins in environmental ergonomics. Scandinavian Journal of Work, Environment & Health, 15(1), 84–94.

Xu, J., Psikuta, A., Li, J., Annaheim, S., & Rossi, R. M. (2019). Influence of human body geometry, posture and the surrounding environment on body heat loss based on a validated numerical model. Building and Environment, 166, 106340.

Yang, J., & Zhang, S. (2023). Three-dimensional simulation of the convective heat transfer coefficient of the human body under various air velocities and human body angles. International Journal of Thermal Sciences, 187, 108171.

Yuge, T. (1960). Experiments on heat transfer from spheres including combined natural and forced convection. Journal of Heat Transfer (US), 82, 214–220.

Zhang, X., Chao, X., Lou, L., Fan, J., Chen, Q., Li, B., Ye, L., & Shou, D. (2021). Personal thermal management by thermally conductive composites: A review. Composites Communications, 23, 100595.

Zhu, F., Zhang, W., & Song, G. (2008). Heat transfer in a cylinder sheathed by flame-resistant fabrics exposed to convective and radiant heat flux. Fire Safety Journal, 43(6), 401–409.